2D Mott Hopping of Vortices in an Amorphous Indium Oxide Film

A DISSERTATION
SUBMITTED TO THE FACULTY OF THE GRADUATE SCHOOL
OF THE UNIVERSITY OF MINNESOTA
BY

Ilana Michele Percher

IN PARTIAL FULFILLMENT OF THE REQUIREMENTS
FOR THE DEGREE OF
DOCTOR OF PHILOSOPHY

Allen Goldman

July, 2018

Acknowledgements

I have been extremely fortunate to have the opportunity to pursue this degree. I credit my parents' commitment to my education for making it possible for me to have envisioned this path in the first place. I am grateful to them, my sister and best friend, Joanna, and the entire extended family for supporting me through this process with forbearance and hearty enthusiasm. I want to thank my wonderful partner, Jason, for his dedication to lightening my load and celebrating my successes these past several years. Thanks to all of my friends for spurring me on and being such good company.

I want to thank my advisor, Allen Goldman, for his outstanding mentorship and long-term support. It was a privilege to work under and alongside someone with such deep knowledge, excellent intuition, and superhuman memory of the literature. I admire and am grateful for his remarkable patience as a person and a scientist, his dedication, and the good-humored curiosity he brings to this work.

Thanks go to those Goldman group colleagues who passed along their knowledge of practical laboratory matters as well as functional equipment: Steve Snyder, JJ Nelson, Yen-Hsiang Lin, Javi Garcia-Barriocanal, and Yeonbae Lee. I would like to give a special shout-out to Joe Kinney for repairing the Kelvinox 25 so that I was able to use it. It has been a pleasure to work alongside contemporaries Boyi Yang, Nicholas Lewellyn, Terry Bretz-Sullivan, and Danqing Deng–thank you for all of your help and good ideas. I could not have done this work without the facilities of the Minnesota Nano Center and the support of its great staff. I have been grateful for access to the Minnesota Characterization Facility and its staff, and the support of the machinists in the Physics and then CSE machine shops. Bill Voje played a vital role in this research by liquifying the many liters of helium it required. I am also grateful for his work maintaining the student machine shop–the facility I will probably miss the most.

Thanks to collaborators Aviad Frydman and Irina Volotsenko, who grew the interesting indium oxide films discussed in this thesis.

I want to thank my Ph.D. committee. Boris Shklovskii's course was my favorite in all of graduate school. His interest in these results and theoretical contributions toward understanding them gave this project traction. I appreciate the careful attention Chris Leighton and Paul Crowell gave to this document. Paul has provided advice, feedback, and hands-on support on all manner of topics, and I particularly appreciate his particular style of nurturing. My thanks go to the entire condensed matter group at Minnesota for their support and community, as well as to the School of Physics & Astronomy for investing in me. I am grateful to many past and present students (and post-docs and faculty) within the School of Physics & Astronomy for their camaraderie, friendship, and collaboration. Friends from my first year, and those I know through WiPA, have a special place in my heart.

Finally, I want to thank the funding agencies that made this work possible. This work was supported by the Condensed Matter Physics Program of the National Science Foundation under Grant No. DMR-12663316. Part of this work was carried out at the University of Minnesota Characterization Facility, a member of the NSF-funded Materials Research Facilities Network via the MRSEC program (Grant No. DMR-140013), and the Nanofabrication Center, which receives partial support from the NSF through the NNIN program.

Dedication

To Pam Vo, who should have had the same support that I did.

Abstract

The electron transport behavior of a thin film of amorphous indium oxide was studied as it was driven across the superconductor-insulator transition by a perpendicular magnetic field. For the range of field values between zero and the critical field of the transition, a positive slope in temperature dependence of the resistance was observed in the data. These data are best described by the form of two dimensional Mott variable range hopping as applied to vortices. The quality of this fit is demonstrated over several orders of magnitude in resistance and over a broad range of fields using several methods of analysis. The observation of variable range hopping of vortices is the main result of this work. Data from a second sample were also found to be consistent with vortex variable range hopping, as were data extracted from a paper within the literature. These examples suggest that this behavior has probably been overlooked in the past. The field-dependence of the characteristic hopping temperature T_0 at very low fields was predicted using a granular model for the thin film. This is consistent with the picture of effective granularity induced in a highly disordered superconductor, which also explains various properties of the film, including the magnetoresistance peak observed at high fields. What was not observed, however, was a crossover from Mott to some other hopping behavior at high fields, where corrections to the hopping exponent due to vortex-vortex interactions were expected. The reason for this is an open question.

Contents

List of Figures

Chapter 1

Introduction

When Heike Kamerlingh Onnes first observed superconductivity in mercury in 1911, it was quite a surprise. The behavior of metals in the limit of zero temperature was being measured for the first time, but certainly nobody had predicted that the finite electrical resistance of the metal would drop abruptly to zero at temperatures below 4.18 K [1]. At this point, quantum mechanics, which describes the physics of cold, interacting systems, was still in the early stages of development. The tools to understand the phenomenon of superconductivity did not yet exist. Two years later, when his efforts were rewarded with a Nobel prize, he recognized that the puzzling phenomenon of superconductivity could be very useful [2].

It would be another 13 years before Satyendra Nath Bose would formulate the quantum statistics that could explain the low temperature behavior of bosons, sub-atomic particles with integer spin. A full 50 years would pass before Bardeen, Cooper and Schreiffer would figure out how electrons, which are half-integer-spin fermions that obey wholly different quantum statistics, could develop an attractive interaction within a crystal, in order to form bosonic pairs and collapse into a superconducting condensate–a many-body quantum state spanning the entirety of the superconducting sample.

In 1986, superconductivity was discovered to occur in doped copper-oxide ceramics at temperatures far above what could be explained by the existing theory, opening up new horizons for potential applications. Magnetically ordered iron-based materials were doped into a superconducting state in 2006. The superconductivity in these high-T_c materials is still not fully understood. For over a century, the study of superconductivity

has offered a succession of surprises and new physical puzzles, as well as a continued promise of technological opportunity.

The results presented in this dissertation were obtained from an experiment designed to explore details of the superconductor-insulator transition (SIT) in an amorphous thin film. This is a transition between quantum ground states in the limit of zero temperature, which we tuned using an applied magnetic field. It so happened that the most interesting result was found unexpectedly in form of the finite-temperature data.

Specifically, the temperature dependence of the film resistance took a form that indicates quantum motion of vortices across the film between localized sites. (Vortices are holes in the condensate through which single quantized lines of magnetic flux pass.) This temperature dependence was developed to describe resistance due to the quantum hopping of non-interacting charges in insulators by Sir Neville Francis Mott. As we will explain, it can also be used in a straightforward fashion to describe the *conductance* due to the motion of vortices, though this has seldom been observed. This dissertation presents an argument that Mott hopping provides the best description for a significant portion of our data for a single main sample, and also for other samples.

This dissertation is comprised of five chapters. The four chapters that follow this introduction progress as follows:

Chapter 2 briefly presents the physics relevant to this work. This covers basic theories of the superconducting state, vortices, and the superconductor-insulator transition. Theories of charge hopping in disordered insulators are also discussed.

Chapter 3 contains a description of the experimental methods, as well as some background about amorphous indium oxide as a material.

Chapter 4 presents the results from this experiment. These results come primarily from data gathered from a single sample. The data are presented in sections related to the sample behavior, defined by the sign of the slope of the resistance versus temperature curves. Details about the sample structure, disorder, and dimensionality are also explored here.

Final discussion of these data is provided in Chapter 5, offering conclusions, open questions, and directions for future work.

All physical relationships presented here are in the Gaussian CGS unit system.

Chapter 2

Review of relevant physics

This chapter covers the physical concepts that are important for understanding the results presented in this dissertation, which come from disordered superconducting films. This review will cover the two main theories of superconductivity with a focus on phase behavior and vortices in type II superconductors, films, and Josephson junction arrays. These concepts will be applied to the problem of the superconductor-insulator transition, where there is approximate duality symmetry. A final section covers mechanisms for charge hopping in disordered insulators.

2.1 The Superconducting State

Two main behaviors characterize the superconducting state: the perfect conductivity from which it gets its name, and the expulsion of magnetic fields from the interior of the superconductor, known as the Meissner effect.

A superconductor is a perfect conductor in the sense that it can carry an electrical current I with zero voltage drop, which by Ohm's law

$$V = IR \tag{2.1}$$

means electrical resistance $R = 0$. Since power $P = IV$, electrical conduction in these systems occurs without power dissipation. This is an extremely useful property made possible by the fact that the superconducting condensate is a macroscopic quantum

ground state of the electrons in the system. The charges carrying the electrical current have no spare energy to thermalize, so they move frictionlessly and coherently through the system below a critical temperature T_c and current I_c.

The nearly perfect diamagnetism exhibited in the Meissner state results from a thin skin of supercurrent at the surface of the superconductor, which screens the field. Expulsion of an external field from a superconductor can be understood from the classical Maxwell equations, and follows from the perfect conductivity. However, if a field exists within superconducting material above T_c, it will be expelled when the sample is cooled through the transition. This cannot be explained classically.

Bardeen, Cooper, and Schreiffer (BCS) developed a microscopic theory to explain the Meissner effect and the very existence of superconductivity as a function of this many-body quantum state [3]. They determined that interactions between electrons within a Fermi sea and the lattice background become attractive at sufficiently low temperatures. This attractive interaction leads to the formation of bound pairs of electrons known as Cooper pairs. Unpaired electrons obey the Pauli exclusion principle and fermionic statistics, but when paired they effectively obey bosonic statistics and fall into a collective quantum ground state similar to a Bose-Einstein condensate.

The superconducting condensate is separated from single-particle (in this context, quasiparticle) states by an energy gap Δ. The energy gap, also called the pairing potential, indicates the strength of the superconductor. It relates to the superfluid density $n_s = \Delta^2$. The BCS theory also predicts the Meissner effect, in that there is a higher energy cost to admit a field into the many-body state and break time-reversal symmetry than to screen the field out entirely. This is true up to a critical field strength B_c. The picture provided by the BCS theory, and its predictions about thermodynamics, have been enormously important for the understanding of superconducting phenomena. The drawback for the predictive capacity of the BCS theory is that it describes superconductors of infinite extent with spatially uniform Δ, which is not a realistic description of experimental systems, especially reduced dimensional disordered systems like the one under study here.

For this reason, the purely phenomenological theory developed by Ginzburg and Landau has proven very predictive [4]. This theory was developed several years before the BCS theory and thus does not depend on the microscopic picture, though Gor'kov

later showed that the Ginzburg-Landau (G-L) theory is a special case of the BCS theory [5].

Most of the theory relevant to this thesis comes from the G-L treatment, which extended Landau's theory of second-order phase transitions to the case of superconductivity. This uses an expansion in the free energy around the transition that can account for spatial variation of the order parameter. The result is a pair of equations [6] that have solutions in the form of a complex order parameter

$$\Psi = |\Psi| e^{i\varphi} \tag{2.2}$$

with amplitude $|\Psi|$ and phase φ degrees of freedom. The order parameter functions much like a macroscopic wavefunction which describes the superconducting condensate of BCS theory over real space. Like a wavefunction, the modulus squared returns a probability density, with $|\Psi(\vec{x})|^2 = n_s(\vec{x})$, a quantity that is nonzero for $T \leq T_c$, increasing with decreasing temperature. The physical importance of the phase φ is in its evolution in space, and over time, as we shall see later in the chapter. The second of the two G-L equations

$$\vec{j}_s = \frac{2en_s}{m}\left(-\hbar\nabla\varphi - \frac{2e}{c}\vec{A}\right) \tag{2.3}$$

relates the supercurrent response $\vec{j}_s$ to changes in φ as well as the presence of magnetic vector potential $\vec{B} = \nabla \times \vec{A}$.

The G-L theory describes systems where $T \approx T_c$ and Ψ is small, and where sample disorder restricts correlations to occur over short lengthscales. For systems outside this narrow region, the G-L theory offers an approximate picture of sample behavior.

The penetration depth λ describes the screening distance necessary to expel a magnetic field, and is one of two important lengthscales for superconductivity. Screening of the applied field occurs over a certain thickness

$$\lambda^2 = \frac{mc^2}{4\pi n_s e^2} \tag{2.4}$$

into the superconductor, were, m is the electron mass and e is the fundamental charge. The relation presents $\lambda^2 n_s$ as an invariant quantity, related to the total current necessary to screen superconductivity. This relationship was first determined as part of a set of

phenomenological equations the London brothers developed in 1935, extended from Maxwell's equations, to describe the electrodynamics of superconductors [7]. London's penetration depth, λ_L, is a temperature-independent quantity.

Both the BCS and G-L theories have more detailed approaches to the penetration depth. In the G-L theory $n_s = |\Psi|^2$ depends on temperature, and thus so does $\lambda(T)$, which diverges near T_c. The BCS theory offers additional corrections for the case of superconductors with a high level of disorder. In the "dirty limit", which is defined below, a correction to the London penetration depth gives an effective length

$$\lambda_{eff} = \lambda(T) \left(\frac{\xi_0}{\ell} \right)^{1/2} [J_{BCS}(T)]^{-1/2} \tag{2.5}$$

where ℓ is the electron mean free path, ξ_0 is the BCS coherence length, and $J_{BCS}(T)$ is a response function of order unity. The normal state ℓ parameterizes the degree of localizing disorder present in the system, effectively suppressing its superconducting response.

The coherence length ξ describes the extent of a single Cooper pair and the minimum lengthscale for changes in the order parameter. The BCS coherence length ξ_0 is not phenomenological, but rather a value intrinsic to the pure material. The definition $\xi_0 \equiv \hbar v_F/(\pi\Delta(0))$ relates it to Fermi velocity v_F and zero-temperature pairing potential $\Delta(0)$. The dirty limiting case applies to systems where $\ell \ll \xi_0$. On the other hand, the coherence length in G-L theory is phenomenological, given by

$$\xi(T) = \frac{\Phi_0}{2\sqrt{2}\pi B_c(T)\lambda(T)}, \tag{2.6}$$

where B_c is the thermodynamic critical field mentioned above, and Φ_0 is the magnetic flux quantum, which will be explained further in the next section. In the dirty limit, these quantities are related by [6]

$$\xi(T) = 0.855 \, \frac{(\xi_0 \ell)^{1/2}}{(1 - T/T_c)^{1/2}}. \tag{2.7}$$

This shows how $\xi(T)$ also diverges near T_c.

The ratio of these two lengths is known as the G-L parameter

$$\kappa = \frac{\lambda}{\xi}, \tag{2.8}$$

which provides important information about the superconductor's behavior in the presence of a magnetic field. Abrikosov showed a fundamental difference between the response of superconductors with $0 < \kappa < 1/\sqrt{2}$, known as type I superconductors, and those with $\kappa > 1/\sqrt{2}$, which are type II [8]. The distinction between these two types manifests in the response to magnetic field. Type I superconductors expel a magnetic field up to the critical field B_c, at which the energy cost of expelling the field becomes equal to the energy gain of the superconducting state. At fields above H_c type I superconductivity is destroyed. In contrast, a type II superconductor does not enter the "normal" (non-superconducting) state all at once, but rather in stages by introducing vortices–small normal domains–within the superconductor. Reduction in the spatial extent of the superconducting condensate lowers the energy needed to screen it, allowing superconductivity in the condensate to persist above B_c to an upper critical field

$$B_{c2} = \sqrt{2}\kappa B_c. \tag{2.9}$$

Vortices first nucleate at the lower critical field B_{c1}, where

$$B_{c1} = \frac{\ln \kappa}{\sqrt{2}\kappa} B_c \tag{2.10}$$

above which it becomes energetically favorable to form vortices in a type II superconductor.

Most elemental metal superconductors have high carrier concentrations n in the normal state, such that n_s is large and λ is short. These low-κ materials are Type I, and were the first superconductors to be discovered and studied. Type II materials were discovered later, and include compounds used to study superconductivity in disordered systems. These materials, such as TiN, MoGe, and In-O, have low n compared to metals. Type II materials NbTi and Nb_3Sn are able to withstand magnetic fields up to $\approx 15 - 20\,\mathrm{T}$ and are thus standard materials used in superconducting magnets.

The high-T_c superconductors are also type II, and are capable of maintaining phase-coherent superconductivity to very high fields, though engineering magnets from these materials has proven difficult and the technology is currently very expensive [1]. In 2017 a hybrid superconducting magnet, which used high-T_c complex oxide ceramic $YBa_2Cu_3O_{7-\delta}$ (YBCO) coils within coils of more customary materials, achieved a record-breaking persistent 32 T magnetic field [9].

2.1.1 Vortices in superconductors

The magnetic properties of type II superconductors are made possible by the formation of vortices. These allow a small quantity of magnetic flux, known as a fluxoid, to penetrate through the material. The magnitude of the order parameter is suppressed along the length of the fluxoid, dropping to zero at its center and healing almost fully at radius ξ, the minimum lengthscale for such changes.

Because the healing length of the order parameter is shorter than the penetration depth in type II materials, the field will penetrate some distance into the superconducting condensate, prompting a supercurrent response as predicted by Equation 2.3. The swirling supercurrents around the fluxoid center give the vortex its name.

The flux carried within a single vortex is quantized. This can be understood by rewriting Equation 2.3 as

$$\frac{mc}{(2e)^2 n_s}\vec{j_s} + \vec{A} = \frac{\hbar c}{2e}\nabla\varphi \tag{2.11}$$

and considering what happens when a path is traversed through superconducting material described in such a way. Let us first consider a path far away ($\gg \lambda$) from any vortices, so both $\vec{j_s}$ and $\vec{A}$ will be small. Let us take $\vec{j_s} \cdot d\vec{s} \to 0$ for simplicity. By Faraday's law

$$\oint \vec{A} \cdot d\vec{s} = \int \vec{B} \cdot d\vec{S} = \frac{\hbar c}{2e} \oint \nabla\varphi \cdot d\vec{s} \tag{2.12}$$

where $\vec{S}$ is the surface bounded by the path, and $\int \vec{B} \cdot d\vec{S} = \Phi$ is the total flux through that surface. The closed path integral over $\nabla\varphi$ is constrainied by the fact that the order parameter is a single-valued function in space, so changes in φ around the loop can only

occur in integer multiples of 2π. The result of this is quantization of the fluxoid value

$$\frac{\hbar c}{2e} \oint \nabla\varphi \cdot d\vec{s} = n\Phi_0 \tag{2.13}$$

where the flux quantum

$$\Phi_0 = \frac{hc}{2e} = 2.07 \times 10^{-7}\,\mathrm{G}\cdot\mathrm{cm}^2. \tag{2.14}$$

Equation 2.13 holds for all paths through a superconductor.

The energy of a single vortex can be calculated as the sum of the field energy of the fluxoid and the kinetic energy of the supercurrent [6,10] to give the following expression per unit length of vortex:

$$\epsilon_v = \left(\frac{\Phi_0}{4\pi\lambda}\right)^2 \ln\frac{\lambda}{\xi}. \tag{2.15}$$

It is particularly useful and intuitive to relate this quantity to the energy cost of removing the vortex core from the superconducting condensate, ϵ_{core}. The free energy gain Δf due to the superconducting condensate in zero field is equal to the energy density of the thermodynamic critical field B_c, such that $\Delta f = B_c^2/8\pi$. A tube of radius ξ thus costs $\epsilon_{core} = (B_c^2/8\pi)\pi\xi^2$ per unit length when it becomes normal. Combined with the relation for B_c in Equation 2.6, this shows $\epsilon_v = \epsilon_{core}\, 4\ln\kappa$.

With this picture, it is clear how the energy of a vortex is reduced when it sits upon a defect or impurity. Such sites are unavoidable in physical samples, and cause a dip in the local $|\Psi|$ that functions as a potential well to trap the vortex. We shall see presently that defect pinning of vortices is very important in determining the behavior of type II superconductors.

In the presence of a current density $\vec{J}$, a single vortex experiences a version of the Lorentz force,

$$\vec{f}_L = \vec{J} \times \frac{\Phi_0 \hat{n}}{c}, \tag{2.16}$$

where $\hat{n}$ indicates the direction of field in the fluxoid. If the vortex line moves under this force in the absence of pinning, viscous damping from the condensate will oppose the force. The vortex will move at a constant $\vec{v}$ perpendicular to $\vec{J}$, producing an electric

field

$$\vec{E} = -\Phi_0 \hat{n} \times \frac{\vec{v}}{c}. \tag{2.17}$$

The electric field is anti-parallel to $\vec{J}$, so that mobile vortices effectively create resistance, even in a superconductor below its transition temperature. The success of the superconducting magnets mentioned at the end of Section 2.1, which all require dissipationless conduction of type II superconductors in order to run a persistent supercurrent and stable magnetic field, then rests in the pinning strength of the material's defects. The force from a sufficiently large current will "de-pin" weakly bound vortices. Vortices moving through the condensate experience a viscous drag that leads to dissipation of electrical energy into heat.

This has very real consequences in superconducting magnets. Vortex motion across the current-carrying coils of a solenoid magnet results in relaxation of its stored magnetic field. If the loop traversed in Equation 2.13 traced along the outer edge of a current-carrying cylinder, an escaping fluxoid would cause a discontinuous jump in winding number n as it intersected the path. This corresponds to a "phase slip" of 2π. Thus, there has been considerable interest in understanding as well as minimizing vortex dynamics and phase slips.

Because a current exerts a force on a vortex, and circulating supercurrents are part of the vortex object, nearby vortices interact. The direction of these currents means vortices carrying parallel fluxoids repel one another, and those with anti-parallel flux attract. The vortex-vortex (as opposed to vortex-antivortex) interaction energy $\epsilon_{v\text{-}v}$ can be calculated from the Maxwell-London equations [6], and takes the form

$$\epsilon_{v\text{-}v}(r) = \frac{\Phi_0^2}{8\pi^2\lambda^2} K_0\left(\frac{\lambda}{r}\right) \tag{2.18}$$

where r is the separation between the two vortices and K_0 is a modified Bessel function. Tinkham gives the limiting forms of this function as [6]

$$\epsilon_{v\text{-}v}(r) \approx \frac{\Phi_0^2}{8\pi^2\lambda^2} \begin{cases} \ln\dfrac{\lambda}{r} + 0.12 & \text{for } \xi < r \ll \lambda_\perp \\ \left(\dfrac{\pi}{2}\dfrac{\lambda}{r}\right)^{1/2} e^{-r/\lambda} & \text{for } r \to \infty \end{cases} \tag{2.19}$$

The logarithmic approximation in Equation 2.19 indicates that vortices are strongly interacting over distances $r < \lambda$ in bulk superconductors, but less so further away.

2.1.2 Superconductivity in thin films

Let us now consider a thin superconducting film with thickness $d \ll \lambda$, with magnetic field applied perpendicular to the surface, such as the samples considered here. Screening current I_{scr} is provided by current density $\vec{J}_s = n_s \vec{v}_s$, where $\vec{v}_s$ is the superfluid velocity. Per Equation 2.4 we can imagine that this passes through an area λ^2 in the bulk regime. In the thin film regime, I_{scr} is carried by the same $\vec{J}_s$ through an area of $d\lambda_\perp = \lambda^2$, where $\lambda_\perp$ is the effective penetration length in thin films. In 1964, Pearl used the Maxwell-London equations to more rigorously establish [11]

$$\lambda_\perp = \frac{\lambda^2}{d} \gg \lambda. \tag{2.20}$$

This inflated effective penetration depth means that below some thickness, even films of type I materials function as type II superconductors. The G-L parameter κ grows as d becomes smaller, and the lower critical field B_{c1} described in Equation 2.10 can also become negligibly small. For very thin and/or small films, $\lambda_\perp$ can become larger than the physical extent of the sample, so that the field is not screened anywhere.

Thus vortices are ubiquitous in ultra-thin superconducting films. This is both due to external fields and excitations. For the former, consider as an example Earth's magnetic field which in Minnesota has a strength of 0.6 Gauss [12]. A sample oriented perpendicular to this field will contain a vortex density $n_v = B_{earth}/\Phi_0 = 3 \times 10^6\,\mathrm{cm}^{-2}$ which corresponds to an average distance $1/\sqrt{n_v} = 6\,\mu$m between vortices. This field passes through any cryostat not specifically equipped with magnetic shielding.

Even in shielded cryostats, vortices form as topological excitations of the superconducting condensate, usually in the form of vortex-antivortex pairs (i.e. vortices carrying fluxoids of opposite direction.)

The total energy of a vortex in a thin film follows from the energy of a vortex in bulk material Equation 2.15 [13],

$$\epsilon_{v\perp} = \left[\frac{\Phi_0}{4\pi}\right]^2 \frac{1}{\lambda_\perp} \ln \frac{\lambda_\perp}{\xi}. \tag{2.21}$$

The expression for the energy for vortices interacting in a thin film departs a bit more from the bulk form. The total interaction energy of vortices in a thin film [10]

$$\epsilon_{v\text{-}v\perp}(r) \approx \frac{\Phi_0^2}{8\pi^2\lambda_\perp} \begin{cases} \ln\left(\dfrac{\lambda_\perp}{r}\right) & \text{for } \xi < r \ll \lambda_\perp \\ \dfrac{\lambda_\perp}{r} & \text{for } r \gg \lambda_\perp. \end{cases} \tag{2.22}$$

This shows that in addition to being larger and more ubiquitous in thin films than in bulk systems, long-range interactions are stronger in thin film superconductors. The energies shown here are for vortices carrying parallel flux, but the sign is reversed for vortex-antivortex interactions, such that there is an attractive potential. In quasi-2D films, this potential is enough to keep pairs bound in pairs at low temperatures. Above a temperature T_{BKT}, predicted by Berezinskii as well as Kosterlitz and Thouless (BKT), the vortices fluctuate and unbind, leading to a regime of dissipation below the bulk transition temperature T_{c0}. This topological transition occurs instead of a classical phase transition because superconductivity with long-range order is forbidden in two dimensions at finite temperatures [6]. However, such a transition is possible at $T = 0$ [14].

2.1.3 Josephson junction arrays and granular films

Films with granular morphology or a high level of disorder have significant spatial variation in $|\Psi|$. Such systems are better described as a a set of discrete superconducting regions than the flat slab superconductor described above. In such systems, grains that are strongly superconducting may be separated by an insulating or normal metal oxide layer or gap, or may have a very small point of contact, forming a weak link. A break in a superconductor that is long enough to cause a substantial suppression of the order parameter, but shorter than ξ so it does not drop to zero, is known as a Josephson junction. The macroscopic superconducting behavior of a granular film depends on what happens at these junctions. The range of possible behaviors is considerable, it turns out, and highly nonlinear.

Josephson was the first to calculate pair tunneling across such a barrier [15], and

found that the rate depended on the phase difference ϕ between the two bulk superconducting electrodes, $\phi \equiv \varphi_1 - \varphi_2$. As in Equation 2.3, spatial changes in phase will give rise to a supercurrent. For nonzero ϕ the Josephson current relation gives

$$I = I_c \sin \phi, \tag{2.23}$$

where I_c is the junction- or system-specific critical current [6]. This relation may describe a junction carrying a sourced current as a supercurrent, in which case the electrodes are said to be Josephson or phase coupled. In the absence of an applied current, the supercurrent will flow for $\phi \neq 0$.

If a potential V is held across a junction the phase evolves. This follows from the fact that the total number of charges on a grain N_e and the order parameter phase φ are quantum conjugate variables. Their quantum mechanical operators do not commute, and a version of Heisenberg's uncertainty theorem can be written

$$\sigma_{N_e} \sigma_\varphi \geq \frac{\hbar}{2}, \tag{2.24}$$

where σ_{N_e} and σ_φ are uncertainty values. Due to the conservation of charge, pair tunneling across the junction leads to evolution of phase ϕ by Josephson's voltage relation

$$\frac{d\phi}{dt} = \frac{2e}{\hbar} V = \frac{2\pi}{\Phi_0} cV. \tag{2.25}$$

Thus, an induced DC voltage across a junction causes an alternating current of frequency $2\pi/\Phi_0$ to flow through the junction and the phase to increase by a quantity 2π with each cycle. This is the same change in phase that occurs when a vortex escapes from a loop as described in Equation 2.14. One oscillation cycle of the AC Josephson effect described here can be thought of as a vortex passing across the width of a junction, perpendicular to the direction of current.

The energy U_J in a single junction can be found from power IV dissipated over time. Integrating this obtains [6]

$$U_J(\phi) = \int \Big(I_c \sin \phi \Big) \Big(\frac{\Phi_0}{2\pi c} \frac{d\phi}{dt} \Big) dt = -E_J \cos \phi \tag{2.26}$$

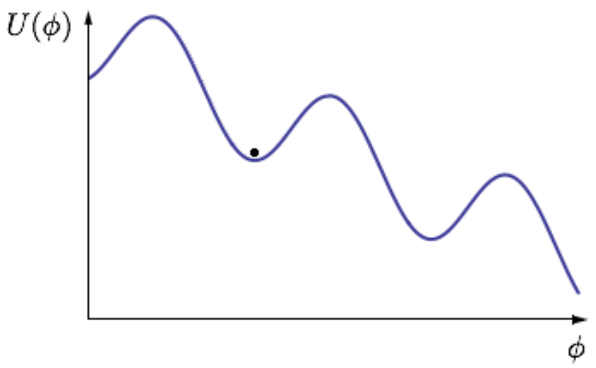

Figure 2.1: The "tilted washboard potential" for the resistively and capacitively shunted junction model, described in Equation 2.28.

where the energy scale is set by the Josephson coupling energy $E_J = I_c\Phi_0/2\pi c$.

If the applied current I and tunneling supercurrent $I_c \sin\phi$ are unequal, charge q accumulates across the junction at a rate $dq/dt = I_c \sin\phi - I$, as it would across a shunting capacitance C. The stored charge would add energy $q^2/2C = CV^2/2$ to the system. In this scenario, a Hamiltonian can be written in terms of ϕ to obtain [16]

$$\mathcal{H} = U(\phi) + \frac{C}{2}\left(\frac{\Phi_0}{2\pi c}\right)^2 \dot{\phi}^2, \tag{2.27}$$

which describes a classical particle of effective mass $M_\phi = (\Phi_0/2\pi c)^2 C$ at coordinate ϕ in the "tilted washboard potential"

$$U(\phi) = -E_J\left(\cos\phi + (I/I_c)\phi\right). \tag{2.28}$$

This potential energy is shown in Figure 2.1 and was determined in the same manner used in Equation 2.26. For $I < I_c$ the phase has stable states in the energy minima, and will stay put unless it has sufficient kinetic energy to escape, or is delocalized by a fluctuation.

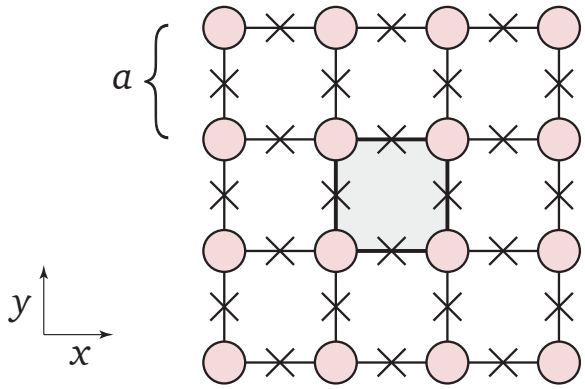

Figure 2.2: Schematic diagram of a 2D Josephson junction array. Circles are superconducting grains or islands, and junctions are marked with an $\times$. The central plaquette is highlighted.

The dynamical response of the phase depends on the junction's damping characteristics. This enters into the problem by way of quasiparticle tunneling across the junction with a resistance R. A viscous drag force $\eta\dot{\phi}$ acts on the phase, where $\eta = (\Phi_0/2\pi c)^2 R^{-1}$. This gives the following equation of motion for the phase in a Josephson junction:

$$\eta\dot{\phi} + M_\phi\ddot{\phi} = E_J\left(\sin\phi - I/I_c\right). \tag{2.29}$$

This treatment of a junction as a compound circuit element is known as the resistively and capacitively shunted junction (RCSJ) model.

The results obtained from studying these single zero-dimensional junctions are useful for higher dimensional systems. Josephson junction arrays (JJAs) can be fabricated to specification, and are highly controllable model systems for exploring the physics of disordered 1D or 2D superconductors. The physics of JJAs crosses over to apply to granular and even continuous nanowires and films [6].

A cartoon of a square JJA is shown in Figure 2.2, which shows circular superconducting islands, each connected to four neighbors by junctions. Each set of four islands connected by junctions surrounding an empty square forms a "plaquette".

Some unique properties arise from the perfect periodicity of the array. Each plaquette has area a^2, so that in a perpendicular magnetic field, the flux through all the

plaquettes would be the same. However, in the coupled, phase coherent state, phase φ will be single-valued in space. A loop traversed along the junctions will need to enclose a quantized amount of flux, just as in Equation 2.14 for a bulk superconductor. As a result, full coherence will be possible when $B = n\Phi_0/a^2$, where each plaquette contains n flux quanta. When this condition is not met, the JJA is said to be frustrated, and will show some electrical resistance. This effect underlies the sensitive magnetometry of superconducting quantum interference device (SQUID) magnetometers comprised of only two junctions in parallel, as well as the very dramatic effects observed in large arrays [17].

The resistance that appears in the JJA in a field can be thought of as a quantum interference effect, but it can also be thought of as the result of mobile vortices. Vortices in a JJA sit in plaquettes while screening currents run through the junctions. When $B \neq n\Phi_0/a^2$, so that not all plaquettes contain the same number of flux quanta, vortices are more likely to move to neighboring plaquettes. When they do move, it is often under the influence of an applied current, just as in the thin film case. In fact, it has been shown that the dynamics of a single vortex in an JJA are essentially the same as those presented in Equation 2.29 for the phase of a single junction. The only necessary changes are the replacement of ϕ with spatial coordinate $x' = x/a$ perpendicular to applied current, and the reduction of the sine term by 90% [18, 19].

The penetration depth in a Josephson junction array, where the screening currents are carried through the junctions is

$$\lambda_{JJ} = \frac{c\Phi_0}{8\pi^2 I_c}. \tag{2.30}$$

This value assumes small screening from individual islands, which is true for $\lambda_{JJ} \gg L$, if L is the total dimension of the array.

The energy of a single vortex in a JJA is

$$\varepsilon_v = \pi E_J \ln \frac{\lambda_{JJ}}{a}. \tag{2.31}$$

This is found using the expression for vortex energy in thin film Equation 2.21 with penetration length λ_{JJ}. Coherence length ξ is replaced by a as the minimum lengthscale for changes within the system, a cross-over between the continuum and discrete systems.

Since it is likely that $L < \lambda_{JJ}$, Equation 2.31 is frequently written with L as the numerator in the logarithmic term.

The interaction energy cuts off much sooner, at the distance between the vortices r. This energy is given by

$$\varepsilon_{v\text{-}v}(r) = 2\pi E_J \ln \frac{a}{r}. \tag{2.32}$$

In arrays with very tiny junctions and islands, the energy to transfer a charge across the junction can become large enough to compete with E_J. This charging energy $E_C = e^2/2C$, so that in the limit of zero bias, the Hamiltonian in Equation 2.27 becomes

$$\mathcal{H} = -E_J \cos\phi + E_C \left(\frac{q}{e}\right)^2. \tag{2.33}$$

Small capacitance can arise not only from the small size of the junction but from the small size of the electrodes or superconducting islands themselves, and their limited capacity to accommodate additional charges this energy. For $E_J < E_C$, the supercurrent will be inhibited by the so-called Coulomb blockade. This is another manifestation of the charge-phase Heisenberg relation in Equation 2.24, which becomes relevant for quantum-sized junctions. The Hamiltonian will have eigenstates in the charge or phase basis, but not both, and competition will determine the dynamics at the junction.

2.2 Superconductor-insulator transition

In the last sections we have discussed some different behaviors available from superconducting systems, not all of which deliver the hallmark properties of superconductors below T_c: resistanceless conductivity and the Meissner effect. These behaviors were explained by BCS as the result of a Bose condensate, which is a many-body quantum ground state. When the system exhibits other behaviors, it provides evidence that the system has entered different ground state. The ground state is the lowest energy eigenstate of a system's quantum Hamiltonian. It is possible to modify a parameter of the Hamiltonian to the point that a transition occurs to a competing ground state. This is a quantum phase transition (QPT), and it occurs at zero temperature.

In the context of electrical systems, three classes of quantum ground state are available: superconductors, metals, and insulators. These are defined by the voltage response

to a current, expressed as the resistance R as defined in Ohm's law, Equation 2.1. In a superconductor, $R = 0$ at $T = 0$. In a metal, $0 < R < \infty$. In an insulator, $R = \infty$[1]. Transitions between these electronic ground states have been studied as examples of QPTs. While it is experimentally impossible to probe these transitions at $T = 0$ where they occur, important details can be obtained by measuring at finite temperatures, both far from and in the vicinity of the transition. Such details include the specific behaviors of the superconducting and insulating states, as well as information about the fluctuations of the system at finite temperatures above the QPT.

Transitions between superconductivity and metallic or insulating states have been tuned by varying magnetic field, carrier concentration, disorder, and stress. Particular attention has been paid to QPTs in thin films in the quasi-2D limit. In 1979 Anderson showed that for 1D or 2D samples, any level of disorder in a sample would preclude a metallic ground state, at least for non-interacting fermions [20]. Thus, in quasi-2D superconducting systems, the expected QPT would be between superconducting and insulating ground states.

Work to understand the superconductor-insulator transition (SIT) has been ongoing for more than thirty years, and a coherent picture, or set of pictures, of the transition has yet to emerge [21]. Furthermore, improvements in fabrication techniques have enabled very clean, purely 2D systems, which continue to provide experimental evidence of metallic behavior [22]. This all suggests that a non-interacting model does not describe the full range of possible behaviors. The nature of the 2D metal, especially in relation to superconductivity, has been a matter of ongoing investigation and debate for more than two decades with regard to experimental methods alone [23–30]. Unsurprisingly, a theoretical picture to describe the set of observed behaviors has yet to cohere [31].

Here it will be sufficient to consider the observed transition in terms of the SIT. Several theoretical scenarios have been proposed for the SIT, but here we will discuss only a bosonic picture for the transition, based on phase fluctuations and the competition between charge and phase, as expressed in Equation 2.24.

[1]There are multiple varieties of insulators, but the focus here will be on materials that are insulating due to the presence of Anderson's localizing disorder.

2.2.1 Dirty boson theory and charge-vortex duality

The original tuning parameter for the SIT was disorder, because there was interest in the interplay between the long-range coherence of the superconducting state and the localizing influence of disorder. The first examples of the SIT were observed in extremely thin films, deposited in minute increments within the cryostat [32–34]. The thinnest films only covered a portion of the substrate, with grains or clusters of material scattered across the substrate surface. The addition of more material filled these gaps, reducing the disorder and increasing the 2D carrier density, eventually bringing about a transition to superconductivity. These pioneering studies from the 1980's found that the SIT usually occurred when sheet resistance[2] in the normal state was at or near $6.45\,\mathrm{k}\Omega = h/(2e)^2$. Figure 2.3 shows the now-classic plot of the SIT induced in an ultra-thin Bi film.

Predictions for a universal critical resistance value could be derived using "dirty boson theory", initially developed around JJAs and superfluid ^{4}He films with quenched disorder. The crux of this theory is the quantum conjugate relationship between N_s and φ described in Equation 2.24. In the context of the Josephson relations, it was shown that flow of supercurrent occurs with a stable (known) φ, while phase instability and incoherence stops charges. The bosonic degrees of freedom considered here are Cooper pairs, which are associated with N_s, and vortices, which are associated with φ. The first key feature of this theory is that if one of these populations is delocalized in a superfluid state, the other must be localized in a glassy solid state. In a superconductor, the Cooper pairs are condensed while vortices are pinned. The other side of this coin is an insulating state characterized by paired charges localized by a superfluid of vortices in a manner akin to a JJA without Josephson coupling between islands. This is known as a Bose or Cooper pair insulator.

Matthew Fisher's 1990 paper laid out dirty boson theory as specifically applied to the SIT in thin films [35]. Shown in Figure 2.4 is a (slightly updated and annotated) version of his schematic phase diagram for a 2D superconductor. Two axes show the effects of tuning by quenched disorder Δ and perpendicular field B, while a third extends the diagram to finite temperatures. Here, the Δ-B plane maps out the landscape at zero

[2] A definition for sheet resistance is given in Equation 3.3.

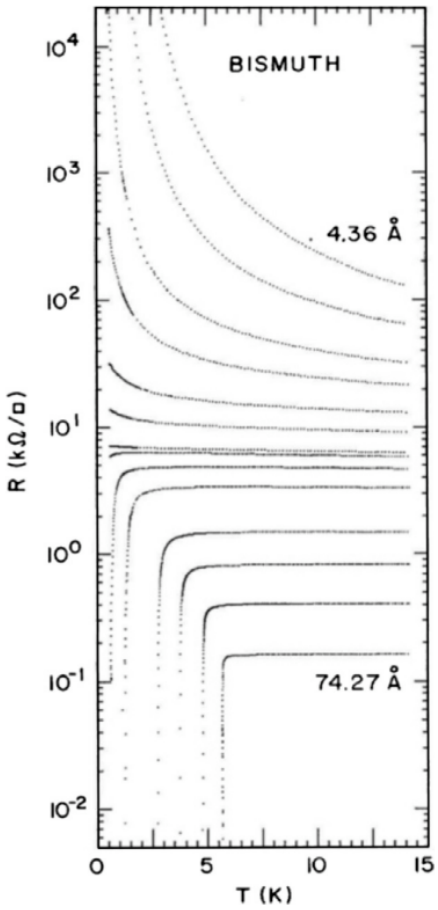

Figure 2.3: The thickness/disorder-tuned superconductor-insulator transition in ultra-thin quench-deposited bismuth, from Reference [34].

temperature, demarcating the region of low Δ and B where vortices are in the glass phase, permitting superconducting behavior in the ground state. Beyond this region on the other side of the B_c phase boundary is the Bose insulator [36]. Further out is a region labeled as an electron glass, though the true nature of this region is disputed [37, 38]. This diagram showed the applicability of the dirty boson theory not only to the SIT tuned by disorder, but also tuned by magnetic field, which at the time of publication was a new idea [35, 39].

The SIT that occurs across this quantum phase boundary is an exchange of roles

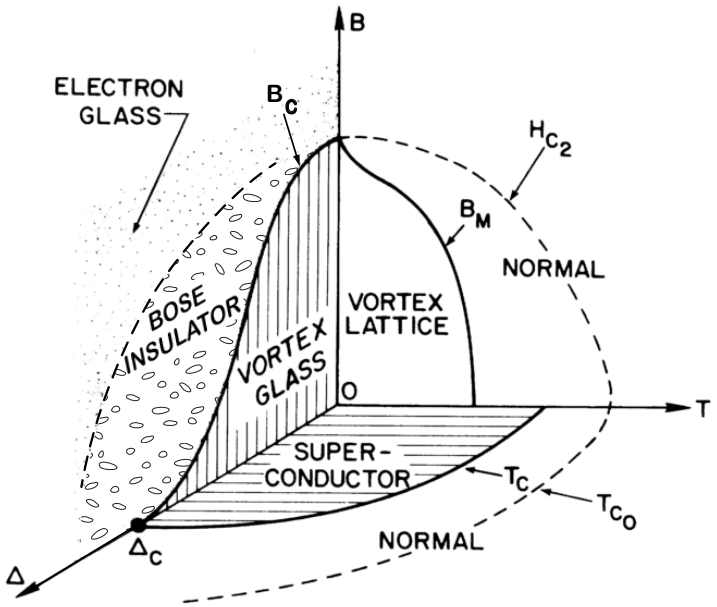

Figure 2.4: Schematic phase diagram of superconductivity in a thin film as a function of magnetic field B, disorder Δ, and temperature T. Adapted from Reference [35].

between Cooper pairs and vortices that is mathematically described by a duality transformation. Duality transformations are generically used to map the physical properties of one system onto another one that is analagous to the first. The systems are not always physically similar, but in some cases duality highlight a symmetry between systems, or within a system. The best-known duality symmetry in physics is between particles and waves in real and momentum space. Duality symmetry between charges and vortices bears some similarity to this.

Disordered superconductors in the dirty boson theory are said to be self-dual because the duality transformation maps between degrees of freedom of the same system [40]. However, the term "self-dual" is also used to describe the system at its QPT, where the mapping between vortices and Cooper pairs is precisely 1:1. This means the critical point occurs where the number of vortices $N_v = N_s$, the number of electron pairs. The phase boundary in Figure 2.4 reflects this equality. N_v is linear in B, so the curve of $B_c(\Delta)$ reflects the suppression of the superfluid density with increasing disorder until it

is entirely suppressed at Δ_c .

In the self-dual state at the QPT, both pairs and vortices move diffusively. Moving Cooper pairs give rise to the current $I = 2e\dot{N}_s$, while moving vortices produce the voltage $V = \frac{h}{2e}\dot{N}_v$, where N_v is the vortex population (and $\dot{N}_v$ denotes its time derivative). Right at the QPT, both boson populations are mobile and diffusive, moving by identical transport such that $\dot{N}_s = \dot{N}_v$, and in competition. These current and voltage contributions give rise to a finite resistance at the transition

$$R_c = V/I = \frac{h}{(2e)^2} \equiv R_Q \tag{2.34}$$

where the universal result R_Q is known as the quantum resistance for pairs. This predicts the universal critical resistance that was observed in early observations of the SIT, and many subsequent experiments.

The success of the prediction of a universal resistance has been surprising, because the symmetry between Cooper pairs and vortices is not exact [16, 35, 41]. The most glaring issue comes from the form of interactions: vortices interact logarithmically at fields high enough to induce the SIT, while charges interact with the Coulomb potential. Even so, reports have been made of symmetric behavior across the QPT, not only in its immediate vicinity but much further out in phase space. A "superinsulating" state mirroring superconductivity was recently reported to exhibit a topological BKT-type transition of charges in NbTiN [37, 42].

Furthermore, the past decades of study have provided examples of systems undergoing SIT revealed systems with $R_c \lesssim R_Q$. Steiner et al. presented a survey of experimental data from a range of films, where $R_c < R_Q$ occurs in low disorder films, and $R_c \simeq R_Q$ in systems with higher disorder [36]. They attribute this to the presence of shunting dissipative pathways in lower-disorder films that are ignored in the dirty boson picture.

Fisher's paper also predicted a form for finite-size scaling around the quantum critical point, allowing for analysis of low-temperature resistance data that reveals the interplay between dynamics and thermodynamics at the transition [35]. These data obey a power-law with specific exponential dependence connecting them with a particular universal model (or "universality class") for the transition that does not depend on microscopic

details of the system [14]. Published alongside Fisher's paper was a second paper by Hebard and Palaanen demonstrating the field-tuned SIT and the applicability of finite-size scaling analysis to these data [39]. Such analysis has been employed successfully many times since, providing evidence that the SIT is indeed a QPT. It has been shown that the field- and disorder-tuned SITs are actually fundamentally different transitions, belonging to different universality classes. However, little clarity has been established as to the nature of these transitions, as multiple universality classes have been found to describe the SIT in systems expected to be similar [43], and due to their universal nature these exponents shed little light on the microscopic origins of these differences.

2.3 Hopping Transport

Transport in systems with localizing disorder hinges on the ability of particles to "hop" between sites. Charge transport has been the primary interest, and hopping by thermal activation or quantum tunneling has been studied in systems where surface effects are important, such as doped semiconductors, amorphous material, and reduced-dimensional samples.

The trapping potential at each site, ϵ_i, is sufficiently strong so that we can consider localized charges to occupy bound states, without regard to neighboring sites or particles within. The wavefunctions of the bound states decay exponentially away from the sites with a characteristic lengthscale a. The rate Γ at which a charge hops from site i to j, via thermal excitation or quantum tunneling, is expressed as the product of these two respective probabilities, giving

$$\Gamma \propto \exp\left(-\frac{r_{ij}}{a}\right) \exp\left(-\frac{\epsilon_{ij}}{k_B T}\right) \tag{2.35}$$

where r_{ij} is the distance between the sites in space and ϵ_{ij} is the difference in energy, k_B is the Boltzmann constant and T is temperature. The first term here describes the tunneling rate between the sites, which depends on the overlap between the exponential tails of the wavefunctions of the sites, and not on temperature. The second describes the rate of activation over the barrier, based on the available thermal energy $k_B T$ and the relative depths of the potential wells. The microscopic conductance will be proportional

to this rate, while the resistance R_{ij} will be the inverse

$$R_{ij} \propto \exp\left(\frac{r_{ij}}{a} + \frac{\epsilon_{ij}}{k_B T}\right). \tag{2.36}$$

This general expression for inter-site hopping shows the competition between thermal activation, which will drive charge transport above a temperature threshold, and quantum tunneling which dominates at the lowest temperatures.

Macroscopic hopping transport occurs as a series of microscopic hops spanning the entirety of a sample. A sample, then, can be treated as a Miller-Abraham network of resistors, each behaving as described above. The potential minima can be expected to have random distributions in space as well as energy, so there will be a great deal of variation in R_{ij}. Percolation theory was developed to predict the behavior of such a network, with the expectation that charges will take the path of least resistance across a sample.

A percolative path is computed using a process where only resistors with R_{ij} below a test value R_{test} are activated. When R_{test} is low, the resistors will not form a complete path across the sample. The number of resistors forming connected clusters of possible paths grows as R_{test} increases. At $R_{test} = R_c$, the percolation threshold, the path extends across the sample, permitting macroscopic transport. All pathways where $R_{ij} > R_c$ can be ignored, as they will be shunted by lower resistance paths. The resistance behavior of the film depends primarily on the behavior of the highest resistance links, for which $R_{ij} \approx R_c$, with the temperature dependence described by Equation 2.36.

At all but the very lowest temperatures, thermal activation dominates and resistance takes the Arrhenius form

$$R(T) = R_0 \exp\left(\frac{U_0}{k_B T}\right), \tag{2.37}$$

where U_0 is the limiting barrier height of the system. In this regime, the charges take the shortest path possible, to the nearest-neighbor pinning site. Lower temperatures create circumstances under which a charge must hop greater distances, which is referred to as variable range hopping (VRH).

Mott's version of VRH, set out in 1968 [44], deals with the case of 2.36 at very low temperatures, where only hops with very small ϵ_{ij} are at all likely to occur. All transport occurs via charges and sites around the Fermi level μ, within a slim energy band of width

$2\epsilon_0$. This band contains only a fraction of the total number of pinning sites, so that in a temperature regime with sufficiently small $k_BT \approx \epsilon_0$ an infinite cluster of nearest-neighbor hopping sites simply does not exist. However, hopping can occur if charges tunnel further. The density of states $g(\epsilon)$ is assumed to be approximately constant within this narrow band, so that the density of carriers can be written $N = 2\epsilon_0 g(\mu)$. This reasoning permits the following approximations for a system of dimensionality d:

$$r_{ij} \to N^{-1/d} = (2\epsilon_0 g(\mu))^{-1/d} \quad \text{and} \quad \epsilon_{ij} \to \epsilon_0,$$

such that 2.36 becomes

$$R_{ij} \propto \exp\left(\frac{1}{(2\epsilon_0 g(\mu) a^D)^{1/d}} + \frac{\epsilon_0}{k_B T}\right) \tag{2.38}$$

The argument of the exponent is now written entirely as a function of energy width ϵ_0, and can be minimized with respect to this quantity to obtain [45]

$$\epsilon_0(T) = \frac{(k_B T)^{d/(d+1)}}{(2\epsilon_0 g(\mu) a^d)^{1/(d+1)}}. \tag{2.39}$$

This gives rise to the general result for d-dimensional Mott VRH

$$R(T) = R_0 \exp\left(\frac{T_0}{T}\right)^{1/d+1}, \tag{2.40}$$

where the characteristic temperature T_0, is given by the relation

$$T_0 = \frac{\beta}{k_B g(\mu) a^d}. \tag{2.41}$$

The coefficient β is not derived directly from Eq. 2.38 , but rather is a dimensionally-dependent coefficient calculated using the numerical techniques of percolation theory, which was offered later as a refinement to the result of [45,46]. The case that is relevant here is 2D, and for this we have the relationship

$$R(T) = R_0 \exp\left(\frac{T_0}{T}\right)^{1/3} \tag{2.42}$$

where T_0 is given by Eq. 2.41 with $\beta \approx 14$ [45].

Mott's model for VRH assumes that hopping charges and accessible sites are far apart and thus non-interacting. Efros and Shklovskii developed a treatment for hopping of interacting charges in 1975, which predicts a soft gap in the DOS at the Fermi level within the narrow band of accessible site energies $\mu \pm \epsilon_0$.

In the case of Efros-Shklovskii VRH, one imagines a system that is more or less in its ground state, with pinning sites below the Fermi level filled with charges, and those above the Fermi level vacant. If a charge is to hop from site i to site j, it follows logically that $\epsilon_i < \mu$ and $\epsilon_j > \mu$. Thus, the hop will necessarily increase the energy of the system by some amount Δ. This sets up the inequality

$$0 < \Delta_{ij} = \epsilon_j - \epsilon_i - {}^{e^2}/_{K r_{ij}}, \tag{2.43}$$

where K is the dielectric constant of the material. The energy of the hop includes the difference between the sites themselves, and a final term for the attractive interaction between the electron that has just hopped to site j, and the hole it left behind at site i. This leads to the inequality $\frac{e^2}{r_{ij}} < \epsilon_j - \epsilon_i$, which prohibits hops between sites that are both nearby in real and energy space. The result is the suppression of the density of states at the Fermi level known as the Coulomb gap [45].

With this form for the density of states $g(\mu)$ the optimization of Equation 2.38 gives rise to a different exponential temperature dependence,

$$R(T) = R_{ES} \exp\left(\frac{T_{ES}}{T}\right)^q \tag{2.44}$$

with $q = {}^1/_3$ and model-specific pre-exponential factor R_{ES} and characteristic temperature T_{ES} [45].

For systems in which charges interact with a form other than the coulomb potential, there can be corrections to the hopping exponent such that ${}^1/_3 < q < 1$. Such systems include hopping of charges in thin films with high dielectric constants [47], and those with very highly correlated electrons [48].

Chapter 3

Experimental Methods

3.1 Samples

The objective of these experiments was to explore aspects of the SIT within the phase space available to a Kelvinox 25 (K25) dilution refrigerator system, which will be discussed in Section 3.2.2. This equipment has temperature stability between $\sim 100\,\mathrm{mK}$ and $1.7\,\mathrm{K}$, as well as a $12\,\mathrm{T}$ magnet. Amorphous indium oxide, a highly tunable superconductor, was chosen as a sample material.

3.1.1 Amorphous Indium Oxide

Indium oxide can be grown in crystalline or amorphous phases. Pure crystalline In_2O_3 is an insulator with a band-gap around $3\,\mathrm{eV}$. In this form, each indium atom is coordinated with six oxygen atoms, while each oxygen has four-fold coordination with indium. Oxygen vacancy defects occur readily in this material, with each missing oxygen resulting in two free electrons. Thus In_2O_{3-x} functions as an n-type semiconductor with carrier concentrations $n \sim 5 - 11 \times 10^{18}\,\mathrm{cm}^{-3}$ [49].

Amorphous indium oxide, which we will refer to as InO_x throughout this thesis, is highly tunable, and shows incredible flexibility in its physical properties. It is optically transparent and has mechanical properties that make conductive (usually Sn-doped) InO_x films useful as electrodes on flat-panel liquid crystal displays. Even without impurity-doping, the material can be tuned to behave as a strong or weak insulator, metal, and/or superconductor based on oxygen content alone.

As in the crystalline system, the density of oxygen vacancies in the amorphous material determines the carrier concentration n. However, without the constraints of crystalline order, carrier concentrations can range from $\sim 2\times10^{18}\,\mathrm{cm}^{-3}$ to $\sim 10^{22}\,\mathrm{cm}^{-3}$ [50]. Rutherford backscattering measurements on low-n InO_x measure an oxygen fraction x=1.45, while for the the highest-n films x=1.1 [51]. The result is a highly disordered system, where charged defects are a source of disorder on top of the underlying structure of the material, which is disordered on an atomic scale [52].

Superconductivity has been observed in InO_x at carrier concentrations $n \gtrsim 10^{20}\,\mathrm{cm}^{-3}$ [53]. Compared with metallic superconductors, with carrier concentrations $\gtrsim 10^{22}\,\mathrm{cm}^{-3}$ [54], InO_x is a low-n superconductor. This strong electron pairing in the presence of strong disorder have made it a very popular material for the study of the disorder-tuned SIT and MIT [38, 55–66].

Film stochiometry, and thus carrier density, can be determined during growth. Films grown by electron beam-evaporation of an In_2O_3 target in a chamber under vacuum have been found to be significantly oxygen deficient. Oxygen content can be increased by mantaining a background pressure of pure O_2 during deposition. Film stochiometry can be adjusted via the ratio of deposition rate to O_2 pressure, which is typical kept on the order of 10^{-5} or 10^{-4} mbar during growth [50].

During the development of this fabrication technique by Zvi Ovadyahu and his group, it was also observed that film disorder could be altered after growth by annealing at low temperatures ($\lesssim 60\,^{\circ}\mathrm{C}$) [50, 51]. Sample resistivity could be reduced by 3-5 orders of magnitude by annealing, as well as producing a transition to superconductivity. This effect was irreversible, and did not depend on sample atmosphere during annealing. Changes to the carrier concentration, determined by Hall effect measurements, were found to be small and not sufficient to explain the large changes in resistivity. The change is then understood to result from increased electronic mobility, or a decrease in the scattering disorder. The stability of the carrier concentration during annealing indicates there is little changed to the disorder due to point defects, since the two quantities are linked. Annealing must then reduce the disorder in interatomic spacing. To explain the increase in mobility, it has been suggested that there might be microvoids in the material that relax during annealing, resulting in more uniformity in local density across the sample [56].

Evidence that annealing does reduce the *average* interatomic spacing supports this picture. Thickness measurements have shown the volume of the film decreases up to 3% during annealing, providing evidence for a structural relaxation within the material [56]. An overall increase in local density would also enhance correlation effects within and across the material, improving superconductivity [52].

InO_x is considered to be a "homogeneously disordered" due to it's structural disorder on an atomic scale [67]. It was found that if substrate temperatures stayed below $\approx 60\,^{\circ}\mathrm{C}$ during deposition and through subsequent processing, films were found to be amorphous, i.e. disordered on an atomic scale. Electron diffraction through such samples has given rise to diffuse peaks consistent with amorphous form [50, 51, 55–57], and similar results have been obtained with X-ray diffraction [59]. Standard electron microscopy and transmission electron microscopy have shown a lack of features that has been interpreted as evidence of homogeneity [58, 59, 61, 62, 66]. This all stands in contrast with the earlier studies on films grown by reactive ion-beam sputtering, which were shown to contain crystallite inclusions [68]. It should be noted that the diffraction and microscopy techniques cited have limited resolution, and crystallites $\lesssim 10\,\text{Å}$ may be present within the film. In 2012, Givan and Ovadyahu used scanning TEM with sufficient resolution to show deviations in transmission behavior of amorphous InO_x films over mesoscopic lengthscales, which was attributed to spatial variation in chemical composition [51], though the exact role of this type of disorder is still not well understood [52].

3.1.2 Sample Design

The desired information about electrical behavior of thin film samples is contained in the electrical resistance R. DC resistance is measured by using Ohm's law

$$V = IR \tag{3.1}$$

where I is sourced current and V is the measured voltage drop in the same direction across the sample.

Measured resistance values depend on intrinsic properties of the material like bulk resistivity ρ, in combination with the specific geometry of the sample under study. We can consider the example of a sample in the form of a rectangular prism, as shown in

Fig. 3.1 with dimensions a, b, c, were I runs in the direction parallel to the side of length

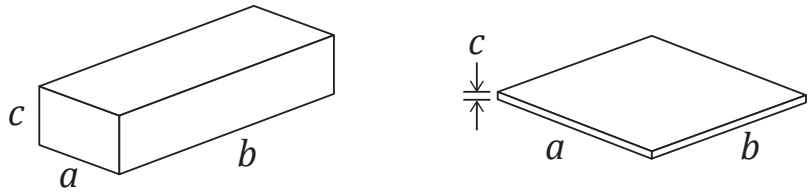

(a) Bulk sample. (b) Thin film sample.

Figure 3.1: Example sample geometries for resistance and resistivity calculations.

b. It takes more energy to move the same current across a longer sample, so $R \propto b$. Charges will flow more easily through a larger cross-section of material, so R will be inversely proportional to $a \times c$. Thus, in a bulk sample,

$$R = \frac{b}{ac}\,\rho. \tag{3.2}$$

For thin film samples where the thickness dimension c is microscopic, surface effects become important and behavior departs from the bulk description. For a hypothetical film such as the one shown in Figure 3.1(b), let us assume $a = b$, so the film in a square. Experimentally it has been shown that the prediction $R = \rho/c$ from Equation 3.2 does not hold for a thin film, as it would for a bulk sample. Thus it is more useful to use sheet resistance R_{sheet}, or $R_{\square}$, to describe the intrinsic electronic behavior of the film, where

$$R = \frac{b}{a} R_{\square}. \tag{3.3}$$

$R_{\square}$ characterizes the electrical behavior of a square piece of film, regardless of size. All resistances values presented in this dissertation are sheet resistances.

The best practice for measuring $R_{\square}$ employs four points of contact with the sample. One pair of contact electrodes delivers current across a sample, while the second set measures the resultant voltage drop. The advantage of the four-probe method is that the only resistances measured will come from the sample, since current does not flow through any other portion of the contacts to the voltmeter. There are two standard sample geometries used for such measurements, and both were fabricated for this experiment.

These are shown in Fig. 3.2. The blue regions in the figure indicate the InO_x film and the gold-colored regions indicate the metal contact electrodes and bond pads.

In the "Hall bar" geometry shown in Figure 3.2 (b), contacts at either end of a strip of film, locations 1 and 2, provide a source and drain for the current. The strip is much longer than it is wide, so that current distributes evenly across the film over the central portion of the strip. Contacts 4 and 3 probe the voltage drop across this uniform portion. Sheet resistance can be calculated from resistances measured in this way by determining a geometric factor, like the one in Equation 3.3. The geometric factor for the sample geometry shown in Figure 3.2 (b) is 23.4 ± 0.6, calculated from the sample design. Uncertainty here is due to the finite width of the voltage probes.

This geometry is named due to the ease with which it permits measurement of the Hall effect, wherein a voltage V_y develops transverse to an applied current I_x in the presence of a perpendicular ($\hat{z}$-directed) magnetic field B. In the free electron model [54], the Hall coefficient $R_H = V_y/(I_x B)$ can be used to determine the carrier concentration n using the relation

$$R_H = -\frac{1}{nec} \tag{3.4}$$

where e and c are fundamental constants for the elementary charge and speed of light, respectively.

A square geometry with corner contacts, as shown in Figure 3.2 (a), is standard for the van der Pauw method of measuring sheet resistance. As before, contacts at 1 and 2 are used to supply a current while contacts at 4 and 3 measure voltage. In this context let us refer to these as I_{12} and V_{43}, respectively. These connections are then rotated 90° so that the current source connects to contacts 2 and 3, and the voltmeter to 1 and 4 to obtain I_{23} and V_{14}. The contact configurations rotate clockwise twice more to acquire a complete set of measurements for all four rotations on the square.

In such a geometry, the current will clearly not be uniform through the sample, as in the Hall bar. However, it was shown in a mathematical proof by van der Pauw that this configuration is perfectly sufficient to determine $R_\square$ [69, 70]. It can be found using the formula

$$\exp\left(-\pi R_\leftrightarrow / R_\square\right) + \exp\left(-\pi R_\updownarrow / R_\square\right) = 1 \tag{3.5}$$

where $R_\updownarrow$ refers to the average of resistances measured in the vertical direction of the

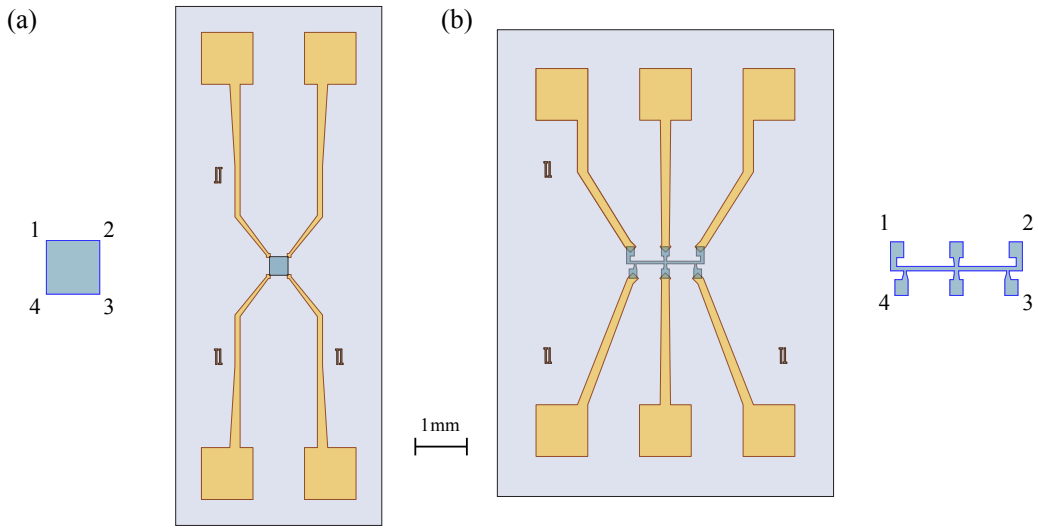

Figure 3.2: (a) Van der Pauw and (b) Hall bar geometries of thin films used to generate the data presented in this dissertation.

sample shown in Fig. 3.2(b), (e.g. $R_{23,14} = V_{23}/I_{14}$, etc..) and $R_{\leftrightarrow}$ refers to the average of resistances measured in the horizontal direction for this sample. It happens that Equation 3.5 does not depend on the square geometry at all, and actually holds for any arbitrarily-shaped thin film. The requirements here are that contacts are point-like and lie in number order in either direction along the outer edges of a film that is free of holes. The only advantage of a square shape in this case is the expectation of uniformity of the measurements.

The patterns shown in Fig. 3.2 were used to determine the InO_x films that will be discussed in Chapter 4. Sample A is a van der Pauw square measuring $360\,\mu m \times 360\,\mu m$, which overlapped the contact electrodes with $15\,\mu m \times 15\,\mu m$ squares at each corner. Sample B is a Hall bar measuring $1500\,\mu m$ from end to end, and $50\,\mu m$ in width.

3.1.3 Fabrication

To fabricate these samples, patterns were defined using a photolithography process, wherein a substrate is coated with a thin layer of photo-sensitive polymer, or "photo-resist", everywhere except where the film is meant to adhere to the substrate. When resist is applied to the substrate it is in a fluid form, thinned with solvent, and spread evenly by spinning the substrate at several thousand RPM. Subsequent heating further improves uniformity of thickness, and removes solvent so the resist becomes solid. The sample patterns had previously been written onto a glass shadow mask using a opaque chrome film, and this is positioned close to the substrate before it is exposed to UV light. The exposure softens the resist, which is dissolved and removed during development to leave the substrate bare in the exposed regions. Leftover resist residue on the substrate is removed in an oxygen plasma at the end of the patterning process. A graphical summary of this process, specifically the double-layer photo-process used to define the contact electrodes, is illustrated in Figure 3.3 (a)-(c).

Samples were fabricated on resistive Si(100) wafers with 300 nm SiO_2 termination layer. Because the photo-process involves a series of bakes above 100 °C and InO_x begins to form crystallites at temperatures above 60 °C, it was necessary to do all patterning before deposition of the film. Thus, titanium-gold contacts were deposited first. This combination of metals is used frequently for thin film contacts. Au has excellent electrical conductivity and is non-reactive. Because of this, it remains very conductive on its surface, providing a good interface for electrical contact to both the sample and bond wires. However, Au does not adhere well to silicon (or SiO_2) substrates. Ti adheres to both Au and Si, and provided a wetting layer to improve adhesion.

Because contacts were deposited before the thin InO_x film, the edge profile of the Ti-Au contacts was important. A smooth and gradual edge profile was necessary for the thin film to sit atop the electrodes and maintain continuity with the rest of the film. This was achieved by limiting the thickness of the contact layer, and by using a double-layer of resist as depicted in Figure 3.3. Shipley 1813 resist was used for the top layer, and LOR 3A was used underneath. Using a process adapted from JJ Nelson, it was possible to achieve an undercut like that shown in the figure. A contact stack comprised of 120 Å Au atop 15 Å titanium was deposited via electron-beam evaporation, and liftoff was performed in bath of Microposit Remover 1165 heated to 80 °C. (All resists and

removers mentioned here are Dow Microchem products.) Through this process, contacts with reliably clean, smoothly tapered and continuous edges were obtained.

InO_x film patterns were defined by a single-layer resist process, using only a single layer of Shipley 1813 resist. Unlike the LOR, this resist is soluble in room-temperature acetone, so that elevated temperatures would not be necessary during liftoff. The single-layer process is identical to that shown in Fig. 3.3, with the lower (green) layer omitted. Patterned substrates, with several devices on a single chip, were then packed up and mailed to collaborators in Israel.

InO_x films with a thickness of 550 Å were grown on these substrates via e-beam evaporation by Irina Volotsenko in the laboratory of Prof. Aviad Frydman in a manner consistent with that described in Section 3.1.1. Material was evaporated from an In_2O_3 target in the presence of an O_2 background. The chamber was pumped continuously while pure O_2 was supplied to the chamber through a needle valve. Sample A was deposited with a nominal O_2 partial pressure of 6.7×10^{-5} mbar. The rate of evaporation for all films was 1.0 ± 0.1 Å/s .

Once the chips were returned, liftoff was performed in a room-temperature acetone bath. Excellent results were achieved when a chip soaked for 2-3 minutes sonication at 50% power for 3-30 seconds. This gave the solvent time to diffuse into and dissolve the resist layer under the excess InO_x material. Parts of loose film still clinging to the edges of the pattern were then shaken free. Individual devices were then cut apart with a wafer saw, and stored in a vacuum until measurement.

(a) *Resist coat.* A substrate (purple) is spin-coated with a first photo-resist, (green), and then a second resist (orange).

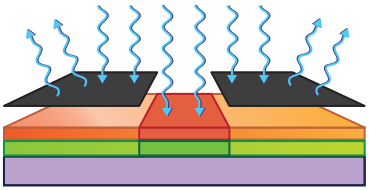

(b) *Exposure.* A shadow mask that blocks all but the sample pattern is placed over the substrate, which is then exposed to UV light.

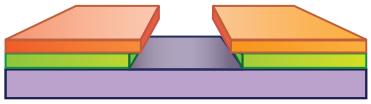

(c) *Development.* The sample is placed in developer, which dissolves the exposed portion of the resist. The process is tuned so that the resist underlayer is eaten further than the upper resist layer, producing an undercut.

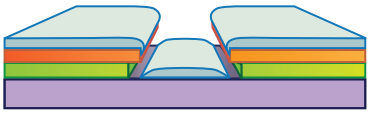

(d) *Deposition.* A thin film is deposited onto the patterned substrate, sticking to the substrate and the top layer of photoresist. The undercut ensures discontinuity between these two film layers.

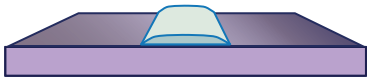

(e) *Liftoff.* Sample is placed in a solvent or chemical stripper, which dissolves the remaining resist. The unwanted film material to float away, leaving only the substrate and the thin film pattern.

Figure 3.3: Double-layer photolithography and liftoff process.

3.2 Measurement

3.2.1 Characterization in the PPMS

Initial characterization of the films were performed in a Quantum Design Physical Properties Measurement System (PPMS) using the ^{3}He option. This cleverly-designed system is capable of reaching temperatures below 0.5 K, and has the advantage of being very fast. It is possible to cool a sample from 300 K to 0.5 K in just over 100 minutes using this tool, and to induce persistent magnetic fields up to 9 T.

The main PPMS refrigerator cools using the evaporation of ^{4}He. Figure 3.4 (a) presents a schematic for the cooling apparatus that sits within, but thermally isolated from, a liquid ^{4}He bath which in turn is surrounded by a liquid nitrogen jacket within the measurement Dewar. This bath cools the superconducting magnet, and provides a source of cryogen for the fridge. The sample sits at center of the magnet bore, at the bottom of a cylindrical space which connects to the access point at the top of the Dewar (not shown). Thin, low-thermal-conductivity stainless steel chamber walls maintain the thermal gradient between the cryogenic sample holder, block, and thermally-anchored measurement contacts at the bottom of the chamber, and room temperature above. Cooling of the sample and space occurs from the bottom up via a cooling annulus chamber surrounding the sample space. ^{4}He gas, which enters the cooling annulus from the main bath through variable impedance, flows upwards through the annulus to a pump. Rapid cooling from high temperatures is possible through contact with gas that boils off from the bath at 4.2 K. When the bath temperature is reached, the liquid pools in the bottom of the cooling annulus and uses heat energy to excite its particles into the vapor phase as those are pumped away by a rotary pump. The vapor pressure drops away with the temperature, so base temperature for continuous cooling is 2 K (1.8 K for shorter periods.)

Still lower temperatures are achieved by using a ^{3}He fridge within this apparatus. The light isotope of helium, ^{3}He, is very rare, and at atmospheric pressure has a boiling point of 3.2 K, the lowest of any known material [71]. It also a significantly higher vapor pressure than ^{4}He making it a particularly good evaporative coolant. Use of the ^{3}He insert with the PPMS allows more than a four-fold reduction of base temperature, to 400 mK.

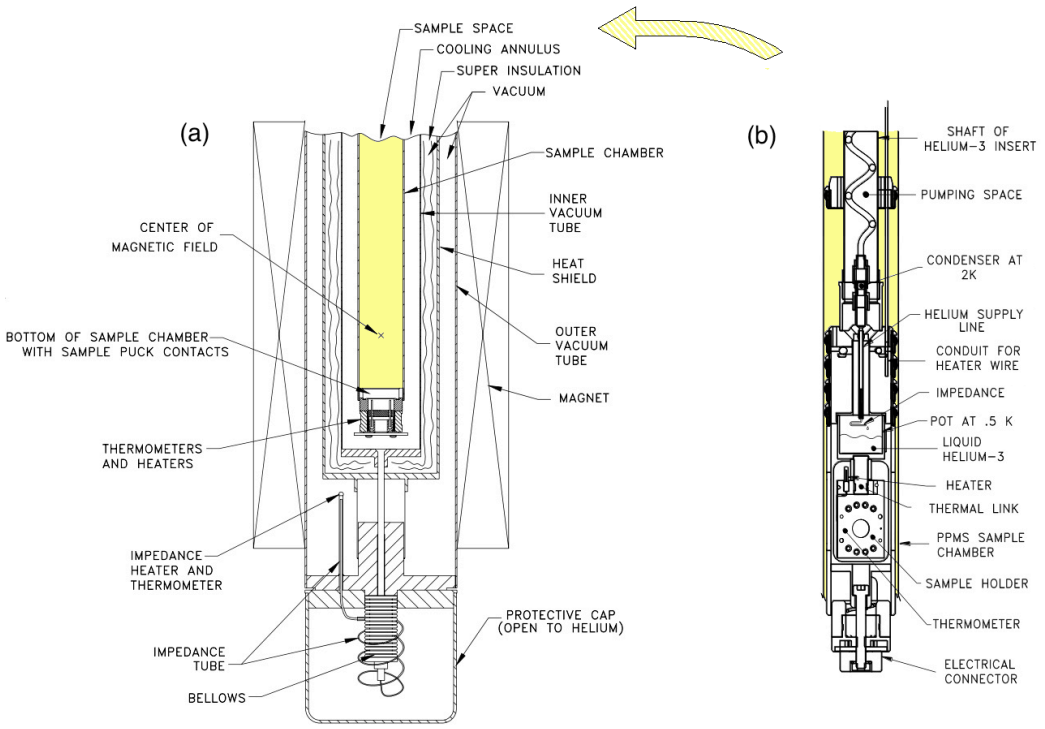

Figure 3.4: Cutaway view of (a) PPMS ^{4}He refrigerator and (b) ^{3}He insert. The insert loads into the PPMS samples space, which is highlighted in yellow. (Adapted from Reference [72])

The ^{3}He fridge is diagrammed in Figure 3.4(b). This insert also takes the form of a long stainless steel tube, which is inserted into the PPMS sample space. Rows of springy metallic fingers heat-sink the insert to the walls of sample space, so it will be cooled by the ^{4}He fridge as described above. When the PPMS reaches base temperature, ^{3}He gas within the insert condenses into a pot just above the sample holder. This chamber is open to a hermetic turbo pump which pulls ^{3}He vapor, cooling the system by the same mechanisms described above for the ^{4}He fridge. For continuous cooling, the helium gas that has been pumped from the chamber returns to the pot through a series of heat exchangers, as well as a condenser cooled by the PPMS, before returning to the pot. The sample mounted to this pot is mechanically isolated from the rest of the system, and the sample space is cryopumped to reduce heat leak due to convection.

Sample temperature is controlled by feedback loops within the software. Thermometers at the sample holder, sample block, and partway up the sample space provide input used to determine power to heaters at these same locations, as well as control of cooling power by regulation of pumping speeds. The resultant fast temperature response and stabilization make this an excellent system for rapid sample characterization prior to cooling in the K25, or samples with features of interest above the operating temperature of dilution refrigerator.

3.2.2 Dilution Refrigerator

The majority of data presented here were measured in the Oxford Instruments Kelvinox 25 (K25) dilution refrigerator. This type of fridge also makes use of helium isotopes ^{4}He and ^{3}He, but here the cooling mechanism comes from what happens when they are mixed together. ^{4}He is a boson which condenses into a superfluid state below 2.2 K, whereas ^{3}He obeys Fermi statistics at the lowest temperatures. At temperatures below 0.86 K, the two very different isotopes cease to mix, and a fluid containing both isotopes separates into two layers, with lighter ^{3}He floating on top of the ^{4}He. While the ^{3}He fluid is relatively pure, the superfluid ^{4}He supports a concentration of 6.6% dissolved ^{3}He, regardless of temperature. This fundamental behavior is what allows dilution refrigerators to provide cooling to temperatures significantly below 1 K.

Figure 3.5 offers a schematic to illustrate this process as it occurs in the K25 during operation. In this figure, which is not to scale, the fridge insert is shown loaded into its dewar, which contains a bath of liquid ^{4}He and a 12 T superconducting magnet. The dewar is insulated by a vacuum chamber filled with layers of superinsulation, called the outer vacuum can (OVC). The apparatus of the dilution unit is contained within the inner vacuum can (IVC).

Sample loading and unloading occurs when the full apparatus is warm and the insert is pulled from the dewar. The indium-sealed IVC is opened and the sample is affixed at the very bottom of the insert, below a series of cooling stages and at the end of what is called “the cold finger”.

Operation of the dilution unit depends on circulation of through the three chambers marked in Figure 3.5: the 1K pot, the still, and the mixing chamber.

The uppermost of these is the 1K pot–a ^{4}He fridge that draws liquid from the main

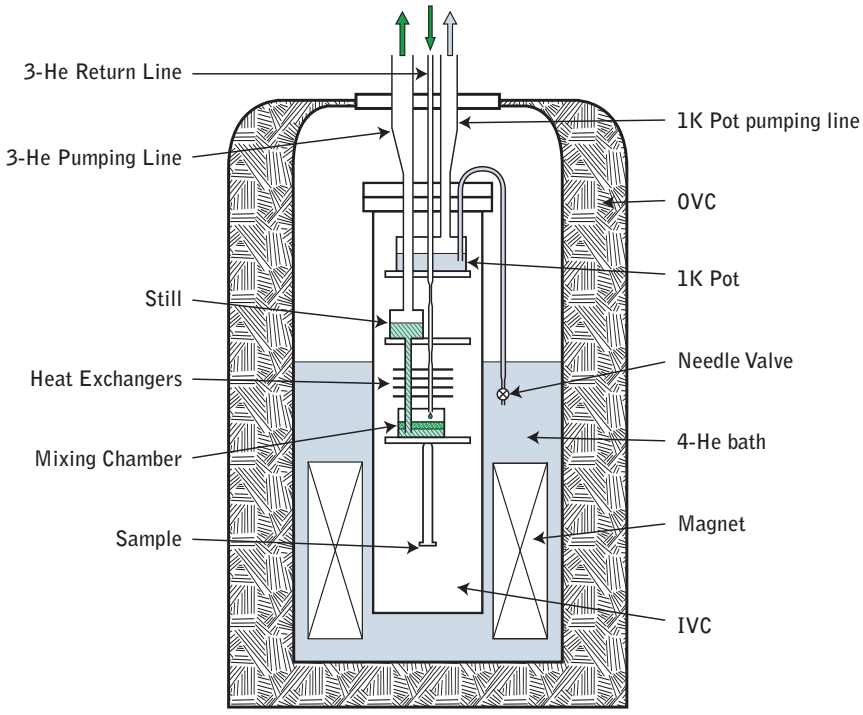

Figure 3.5: Schematic diagram of the Kelvinox 25 Dilution Refrigerator.

bath through a needle valve. This chamber is pumped continuously by a rotary vane pump, and despite its name, maintains a temperature around 1.2 K. This chamber cools and condenses the ^{3}He -^{4}He mixture (which will henceforth just be called "the mixture") during cooldown, and condenses ^{3}He during continuous operation.

During operation, the mixture is condensed into the still and mixing chamber. A pump runs continuously on the still, reducing the pressure with respect to the mixing chamber so the liquid level rises to sit within the still chamber. Pumping on the still also causes evaporation at the liquid surface. Because the vapor pressure of ^{3}He is so much higher than that of ^{4}He, it will be removed preferentially.

The K25 mixture is 16% ^{3}He by volume, so that phase separation occurs below $\approx$ 0.4 K [71]. ^{3}He floats above the phase that is 93% ^{4}He and 7% ^{3}He. (These are commonly referred-to as the ^{3}He-rich and ^{3}He-poor phases, respectively.) The boundary between these phases occurs in the mixing chamber, at a level above the connection to

the still. During continuous operation, the pump on the still causes ^{3}He to leave the ^{3}He-poor phase. To replenish this, ^{3}He will pass across the boundary and dissolve into the poor phase, a process that absorbs thermal energy. Removal of ^{3}He at the still directly leads to a cooling process to occur at the mixing chamber. In stark contrast with the evaporation methods discussed previously, the "dilution" process does not reach a finite equilibrium temperature, but instead can cool continuously, or at least until the cooling power of the fridge is equal to the energy entering the system by way of heat leaks, which are kept to a minimum.

The biggest heat leak comes from the ^{3}He itself, which must be returned to the fridge after it is pumped out in order for cooling to remain continuous. ^{3}He returns to the fridge through a narrow condenser line, through a set of heat exchangers and impedances that slow it down so it cools before returning to the mixing chamber.

The mixing chamber stage is the center of temperature measurement and control. A ruthenium oxide (RuO_2) resistance thermometer and heater resister on the stage are connected to a low-noise resistance bridge and power supply, (Picowatt OY AVS-47A and TS-530) which provide temperature control via feedback loop. The sample itself is located about a foot away in the bore of the 12 T magnet, at the end of the cold finger. RuO_2 has low sensitivity to magnetic fields compared to other resistance thermometers, but it will not function as intended in high fields. Instead, it is kept above the magnet and a compensation coil that reduces stray fields to ~ 1 mT. The cold finger is engineered for maximum thermal coupling between the sample and mixing chamber. Copper is among the best thermal conductors at cryogenic temperatures, and this is used for the mass of the cold finger, as well as the electrical connections from the level of the mixing chamber down to the sample. The sample wiring and cold finger are all heat sunk to the mixing chamber, and the assumption is that all of these parts are in thermal equilibrium.

However, this is not a safe assumption. Sending measurement current across a resistive sample will lead to the dissipation of heat. Even if the sample is superconducting, the resistive contacts will lead to Joule heating. Measurement of the sample inevitably induces some heating at the sample. However, it is possible to keep the resultant thermal gradient between the sample and the thermometer very small if thermal contact with the sample is good and the power of the measurement current is kept very low. Joule

heating can also come from electrical background noise, which can be more difficult to control. At temperatures below 100 mK, there can be additional complications, such as a thermal decoupling between electrons and the lattice [73].

The magnet is comprised of concentric solenoids of niobium titanium and niobium tin. It is thanks to such material technology that a magnetic field of such magnitude can be delivered in such a compact space, with unparalleled field stability! Control of the field is made possible by the activation and opening of a superconducting "switch"–a portion of the coil heated into the normal state. The switch now has high electrical resistance, so the current in the electromagnet redirects through normal metal leads to a power supply, which can ramp the current (and field) as needed.

The Kelvinox 25 is designed to be a relatively nimble dilution refrigerator with a low thermal mass. This allows for rapid cooldown. The process of loading a sample at room temperature to achieving base temperature can be performed in three days at a leisurely pace. The fridge is named for the 25 mW of cooling power it was designed to provide at 100 mK. When it was purchased in 1990, it was able to achieve a base temperature of 30 mK. In the intervening years of service, performance declined. In 2010, Joe Kinney found several leaks and rebuilt several portions of the K25. The sintered silver heat exchanger was found to be damaged, and could not be repaired or replaced. As a result, the base temperature increased to $\gtrsim 80$ mK, and the already modest cooling power of the K25 was considerably reduced. These factors make the K25 extremely sensitive to the sources of Joule heating mentioned above.

While care was taken to reduce the risk of heating, several factors suggest it may have been a problem during the measurements that produced the data shown here.

In 2013, we moved the K25 into a new space in the freshly-constructed Physics and Nanotechnology building, and into a new electrical environment. The lab space and equipment were set up with attention to eliminating noise sources such as ground loops, and iterative improvements were made to electrical shielding and isolation. However, in the months following the measurement run on Sample A, a short was found between a grounded cable shield and a wall-mounted cable tray. This created an alternate ground path to the low-noise instrument ground chosen for the measurement, and would have functioned as a giant antenna. Low-pass pi filters were part of the sample connections, and would have helped attenuate the RF noise, but would not entirely eliminate such a

strong source. Noise was evident in the measurement signal, and likely dissipated excess power to the sample.

An additional trouble was the thermal anchoring of Sample A. The sample was mounted to a Delrin (plastic) sample holder on the end of the K25 cold finger during measurement. This material was chosen for its ease of machining, and was designed for a separate experiment. While it was expected that cooling of the sample would occur primarily through the electrical contacts, the presence of several pin connectors and solder joints might have worked to thermally isolate the sample.

3.2.3 Resistance Measurement

The resistance measurements performed in the PPMS used low noise Keithley 6221 precision current source, and a Keithley 2182 nanovoltmeter. Measurements were made using a delta method, in which a positive current bias is applied across the sample to measure V_+ followed by a negative bias to obtain V_-. Sample resistance is determined using $R = (V_+ - V_-)/2I$, which will average out any time-independent offset voltage. Thermoelectric offset voltages are common where there are large temperature gradients within a measurement circuit. A Kiethley 7001 switchbox was used to rotate contacts around a van der Pauw configuration, when needed.

The resistance measurements made in the K25 were also delta measurements, and a switchbox was also used. Here, the Keithley 6221 precision current source was coupled with a Keithley 2182A nanovoltmeter, a model with the added capability to receive commands from the current source. These were coupled with a high speed cable to give the current source control of the voltmeter, allowing for delta measurements in a "pulse mode", with very tight time tolerances.

Pulse mode permits DC measurements by way of very short ($(\sim 1\,\text{ms}$) current pulses separated by zero-current rest periods. These reduce the average power delivered to the sample by the measurement current, and the communication between the current source and voltmeter allow use of the current pulses with maximal efficiency. Pulses can be adjusted up to a length of 12 ms, with a variable wait time for the system to reach equilibrium before measuring the voltage.

The delta mode used in this configuration is different than the one used in the PPMS. Fig. 3.6 shows a schematic of this measurement, showing the additional step

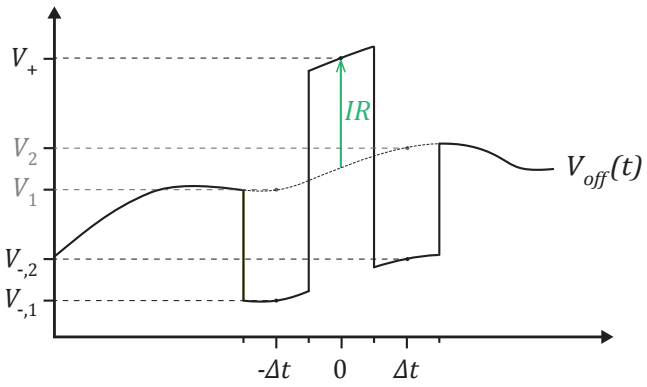

Figure 3.6: Delta and pulse mode resistance measurements using the Kiethley 6221 current source and 2182A nanovoltmeter. V_{off} is the thermo-electric offset voltage, Δt is the duration of the current pulse, and IR is the desired quantity.

that is used to remove a time-dependent offset, $V_{off}(t)$. Here, V_- is measured at some interval Δt both before and after V_+, so we have

$$V_{-,1} = V_{off}(-\Delta t) - IR,$$

$$V_{-,2} = V_{off}(\Delta t) - IR$$

as well as

$$V_+ = V_{off}(0) + IR.$$

In this case,

$$R = \left(2V_+ - V_{-,1} - V_{-,2}\right)/4I$$

provides a better value for R, based on the assumption that $(V_{off}(-\Delta t)+V_{off}(\Delta t))/2 \approx V_{off}(0)$. This approximation improves as Δt becomes small, and in pulse mode this is the case. For measurements of Sample A, $\Delta t = 12\,\text{ms}$, due to a several ms time constant on the response to an applied current.

During the optimization of measurement parameters it was found that the negative-current measurements $V_{-,1}$ and $V_{-,2}$ could be replaced with zero-current measurements

V_1 and V_2, such that

$$R = (2V_+ - V_1 - V_2)/2I.$$

These measurements meant a threefold reduction in average power delivered to the sample during a single resistance measurement, at the cost of a reduced signal-to-noise ratio. Signal quality was recovered by using statistics from repeated measurements.

Each pulse was separated in time by a set period, T, during which time the sample was able to cool. This amounts to a reduction of average Joule power by $\Delta t/T$ as compared to a standard DC measurement with a current of the same magnitude. At low temperatures and high sample resistances, where a thermal gradient between the sample and thermometer is most likely, pulsed measurements departed from more straightforward DC measurements, which had started to flatten out at the lowest temperatures–a sign of sample heating. $\Delta t/T$ of 0.7% or lower made for very slow measurements, but reduced the signatures of heating significantly. At low fields and higher temperatures, where measurements using both DC and pulse mode were consistent, $\Delta t/T$ was set to around 5%.

Chapter 4

Results

The data presented here come from a set of resistance measurements made on amorphous InO_x thin film samples, which were grown on insulating silicon substrates in the manner described in Section 3.1.3.

Data from a single sample, "A", are the primary focus of this dissertation. Some data from a second sample, "B", are also presented. The temperature- and field-dependence of the sheet resistances were measured initially in the Quantum Design PPMS using the helium-3 insert. Both of these films exhibited superconductivity in the absence of a magnetic field as grown–that is, without an annealing–below some critical temperature T_c. For Sample A, the superconducting transition occurred at a low enough temperature such that the bulk of the features of the transition were within the range of the Kelvinox 25. Among these observable features was the destruction of the sample's superconductivity by a magnetic field.

All subsequent measurements of Sample A were made in the Kelvinox 25 dilution refrigerator. In fact, several sets of measurements were performed over the course of a year, each time with refinements made to the measurement technique and attention paid to different aspects of the film's behavior. The sample was stored in vacuum at ambient temperature between measurements. From one measurement to the next, T_c shifted to higher values and B_c shifted lower, indicating a strengthening of superconductivity with time. Usually these changes are observed with annealing at elevated temperatures, but in this case it appeared that the sample annealed at room temperature. Despite these shifts, the features of the sample data presented here appeared consistently across

all data. The $R(T, B)$ data presented here for Sample A all come from a single, self-consistent measuring run using the pulse-delta DC measurement method described in Section 3.2.2.

Hall effect measurements were performed in the PPMS at 10 K to determine normal state carrier concentration $n = 3 \times 10^{20}\,\mathrm{cm}^{-3}$. This is near the lower bound of carriers at which superconductivity has been observed in InO_x [49]. These measurements were made over a year after the $R(T, B)$ data presented here were measured. Though the sheet resistance decreased between the measurements, the carrier density should still be roughly the same [49]. (Hall effect measurements were not made on Sample B.)

As mentioned above, the focus of this dissertation is on Sample A, and the manner in which its resistance changes as a function of temperature in the presence of a magnetic field from 0 to 12 T, applied perpendicular to the plane. Figure 4.1 provides an overview of the data, showing the range of behavior over the full range of fields, from superconductivity at zero field to clearly not-superconducting, insulator-like behavior at high fields.

These same data have been reconfigured to make Fig. 4.2, showing isotherms as a function of field. Here, the transition from superconducting to insulating behavior appears as a crossing of the isotherms near 2.8 T. Here also we see the strong magnetoresistance (MR) peak, a typical feature in InO_x and other highly disordered superconducting films.

From these figures, it is clear that the application of a perpendicular field to Sample A gives rise to a shift in the behavior of $R(T)$ at the lowest accessible temperatures.[1]. Historically, this transition would be categorized as a Superconductor-Insulator Transition (SIT), a quantum phase transition between ground states where $R \to 0$ or $R \to \infty$ in the limit of $T \to 0$. In the picture of Anderson localization, a 2D metallic phase is forbidden [20]. In this approach, the sign of slope dR/dT is enough to distinguish between the two accesible limiting behaviors.

In this picture, Figure 4.3, which maps out dR/dT along a color scale as a function of temperature and field, provides a phase diagram for Sample A. Here, blue and violet

[1]For reasons explained in Section 3.2.2, samples in the Kelvinox 25 are very susceptible to the influence of Joule heating due to background electrical noise. In sample A data, R vs. T curves flatten out at temperatures near 100 mK at all fields. While it is possible this flattening is intrinsic to the sample, heating is a much more likely explanation. Thus, data measured below 120 mK are omitted.

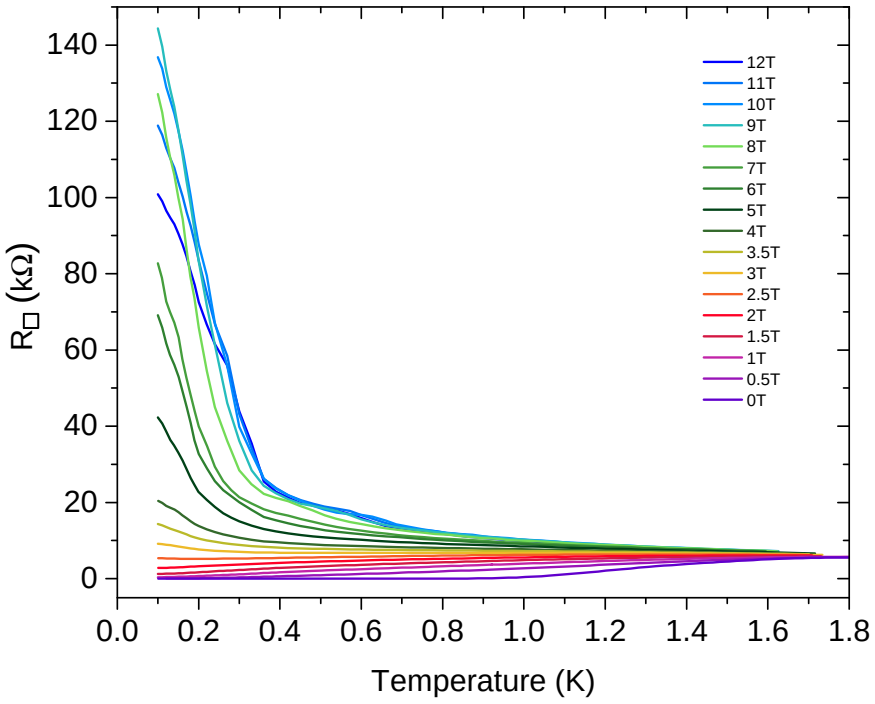

Figure 4.1: Sheet resistance versus temperature at magnetic fields from 0 to 12 T.

signify $dR/dT > 0$, the putative superconducting state found at lower fields, while green, yellow and red indicate $dR/dT < 0$ at higher fields. Regions where $dR/dT \approx 0$ are rendered with stripes. These occur in the lowest left-hand corner of the plot, below about 0.5 K and 0.5 T, where the film is a zero resistance superconductor. They appear again along a curved vertical band around 2-3 T, a transition region between the two behaviors.

Over the last 20 years, experimental evidence has been mounting in support of a finite-resistance (i.e. metallic) quantum ground state in quasi 2-D systems [23–28, 66, 74–77], and there have been subsequent theoretical efforts to address this [78–83]. In this context, the sign of dR/dT does not provide sufficient basis for determining the quantum ground state(s) of the system under study. More definitive characterization requires extrapolation of data to the zero temperature limit.

Despite these limitations, the sign of dR/dT provides a useful parameter by which we can organize the data from Sample A. the different behaviors observed in Sample A,

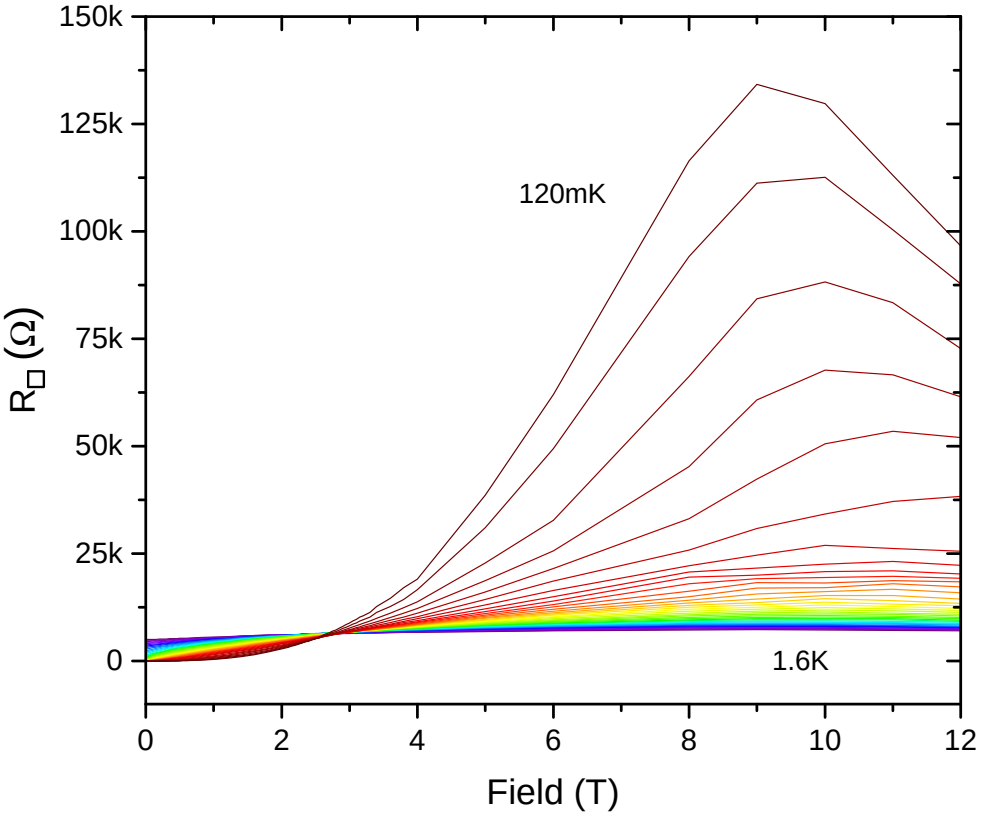

Figure 4.2: Sheet resistance vs. magnetic field. Isotherms range from 120 mK to 1.6 K with a spacing of 40 mK for Sample A.

organized in a manner based on the sign of dR/dT.

The $dR/dT > 0$ section covers behavior from zero field up to near the critical field. It is in this section that the major new finding of this work is presented – the observation of 2D Mott VRH of vortices. Sample B data also show this behavior, and are presented in this section as well. The possible existence of an intermediate quantum metal regime is explored. Features of the transition observed at $B \approx 2.8$ T are explored in the $dR/dT = 0$ section. The high field, $dR/dT < 0$ section covers the putatively insulating regime, which contains the MR peak. A final section covers measurements of Sample A's morphology and other clues to the nature of its microstrucure and disorder.

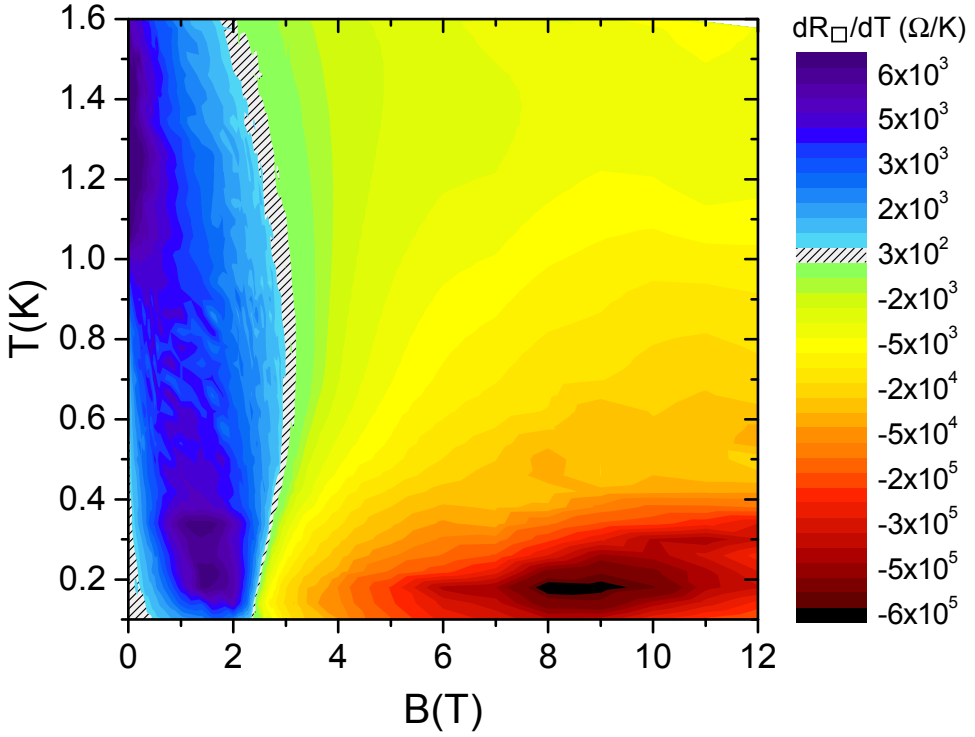

Figure 4.3: False-color plot showing dR/dT as a function of temperature and magnetic field for Sample A.

4.1 $dR/dT > 0$: The Superconducting and Metallic phases

The region of $B - T$ space where $dR/dT > 0$ encompasses a variety of behaviors. The $R(T)$ curves in this regime and the transition region are shown in Figure 4.4. These data show the zero-field transition to superconductivity, as well as the evolution of the sheet resistance with increasing perpendicular magnetic field. The critical temperature T_c is defined in this thesis as the temperature at which $R_\square$ falls to 50% of the normal-state resistance measured just above the transition. T_c for Sample A is 1.27 K.

The zero-field transition occurs over an extended region in temperature, a feature typical for a highly disordered superconductor. The broadening is due in part to fluctuations above the Berezinskii-Kosterless-Thouless temperature for the vortex unbinding transition in 2D [6] but likely owe more to spatial inhomogeneity of the superconducting order parameter $|\Psi|$ across the sample [84]. Variation of the pairing amplitude across the

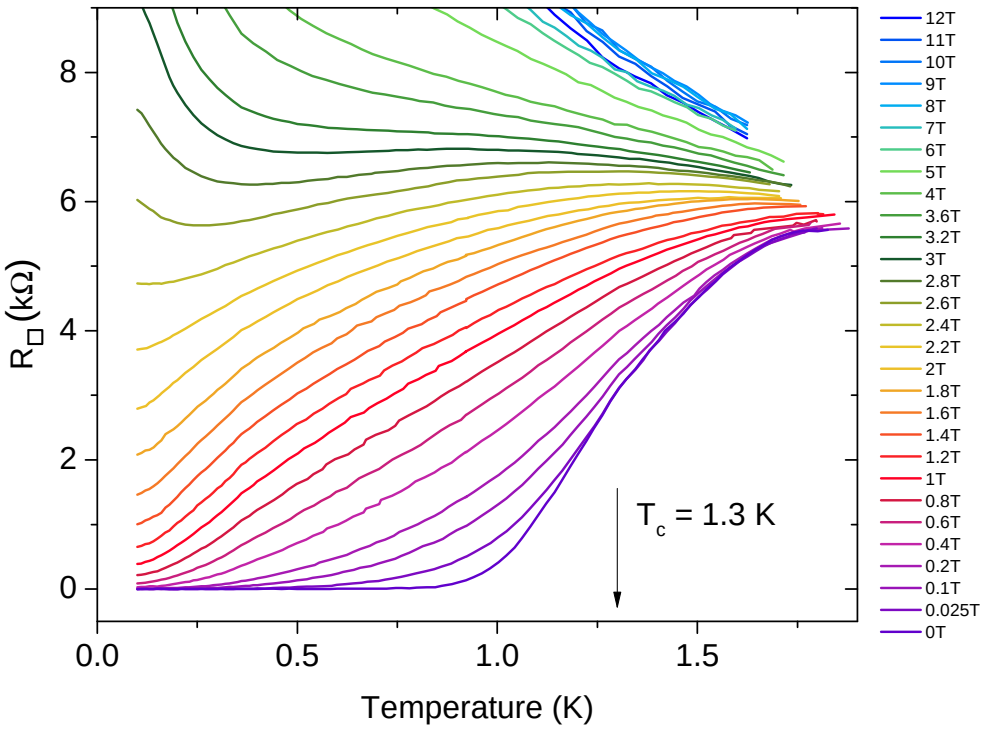

Figure 4.4: Resistance versus temperature at various magnetic fields in the low-resistance region for Sample A.

sample leads to local variation of critical temperature T_c, and smearing of the mean-field transition.

The application of a perpendicular field causes the transition to broaden even further, with the width of the transition becoming larger with increasing fields. This broadening can be explained by the introduction of potentially mobile vortices into the film. As explained in Section 2.1.2, the motion of a single vortex generates a voltage in a superconducting system. As the vortex density n_v increases linearly with applied field, so too does the signal due to vortex motion.

The particulars of the vortex dynamics, which can be understood through the temperature dependence of R, is of considerable interest here and will be discussed in the next sub-section. Also of interest is the extrapolation of these data to zero temperature. For a range of fields within this regime, $R(T)$ extrapolates to a finite value in the limit $T \to 0$, indicating a metallic ground state. This will be examined in Section 4.1.2

4.1.1 Vortex hopping resistance form at finite temperatures

In a disordered system such as the one studied here, vortices are pinned in energy minima as discussed in Section 2.1.1. If a large current is applied, the Lorentz force pulls vortices out of their pinning sites. Below this depinning current, however, movement will be due to fluctuations. Anderson and Kim predicted that due to the strongly interacting nature of vortices, they would necessarily move in "bundles". Their collective motion would take on the Arrhenius form [85]

$$R = \omega_0 \exp\left(-\frac{U_0}{kT}\right) \tag{4.1}$$

where ω_0 is the attempt rate of one of the vortex lines to escape its pinning site, U_0 is the energy barrier to escape, and kT is the available thermal energy. The discovery of high-T_c superconductors prompted the development of a more detailed theory of flux motion, called collective pinning theory. Here, motion occurs as shifts between quasi-stable vortex configurations. The vortex configuration lacks long range order due to the pinning potential, but this motion is similar to that of a defect (or pair of nucleated defects) in a true Abrikosov vortex lattice [10, 86, 87].

The inverted relationship between Equation 4.1, which describes the hopping of vortices, and Equation 2.37, which describes nearest-neighbor hopping of charges, is no accident. The measured resistances presented here are defined with regard to charge transport, as in Ohm's law $R = V/I$. By the Josephson relations, the vortex transport analog $R^v \propto I/V$, such that $R \propto 1/R^v$. This inverse mapping of charge and phase transport is another manifestation of the quantum conjugate relationship between charge number and phase.

Most of the theoretical understanding of vortex behavior has been built around thermally-activated, nearest-neighbor hopping because it is a classical process, and vortices are large enough to be considered classical objects [10,85]. It has proven predictive in a variety of systems. However, the possibility of vortex motion by quantum tunneling has been explored theoretically for Josephson junction arrays [88, 89] as well as for films [86, 90, 91], with ample experimental evidence [23, 24, 92–94]. Vortex motion by hopping has, in fact, been predicted [47, 95, 96] and reported previously, although only a few times [97–99]. These are discussed in detail in Section 5.1 of the next chapter.

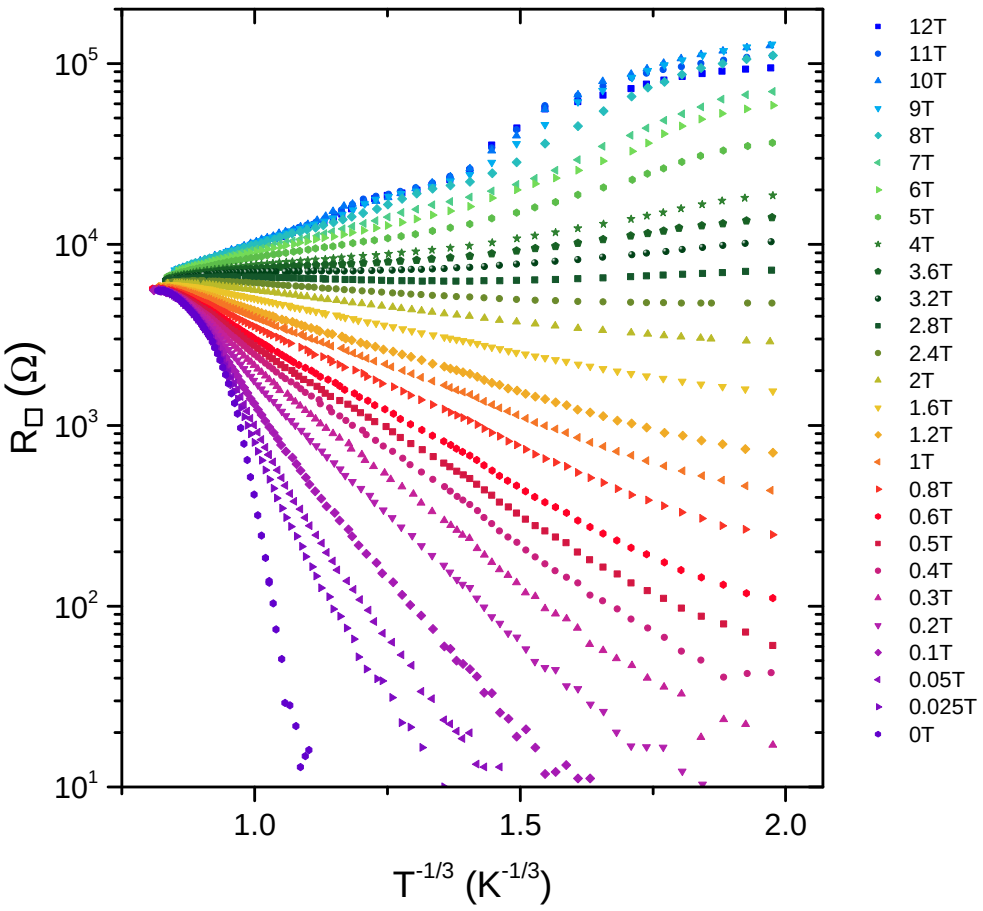

Figure 4.5: Sheet resistance vs. $T^{-1/3}$ at magnetic fields spanning 0 to 12 T.

Thus, Sample A's $R(T)$ data were evaluated against a range of hopping models, such as those described in Section 2.3. For vortex hopping, the generic stretched exponential form for charge hopping is inverted, such that the observed temperature dependence would have the form

$$R(T) = R_0 \exp[-(T_0/T)^{-p}], \tag{4.2}$$

where R_0 is a prefactor, T_0 is the characteristic hopping energy (expressed as a temperature), and the value of p will depend on the hopping model. The exponent $p = 1/3$ was found to best describe the data, and this corresponds to vortices moving by Mott VRH in two dimensions [96].

Several methods were used to arrive at this unexpected result. The first of these was plotting the data as $\log(R)$ against T^{-p} at different values of p predicted for different hopping mechanisms. Data obeying Equation 4.2 fall into a straight line for the best value of p. Figure 4.6 shows $R(T)$ data taken at three representative low fields, plotted for the visual comparison of different p. Here, the upper left panel clearly shows the poor fit for $p = 1$, the exponent for thermally-activated vortex motion. The data appear most linear for $p = 1/3$, based on visual assessment alone. Figure 4.5 allows for a visual assessment over the full field range.

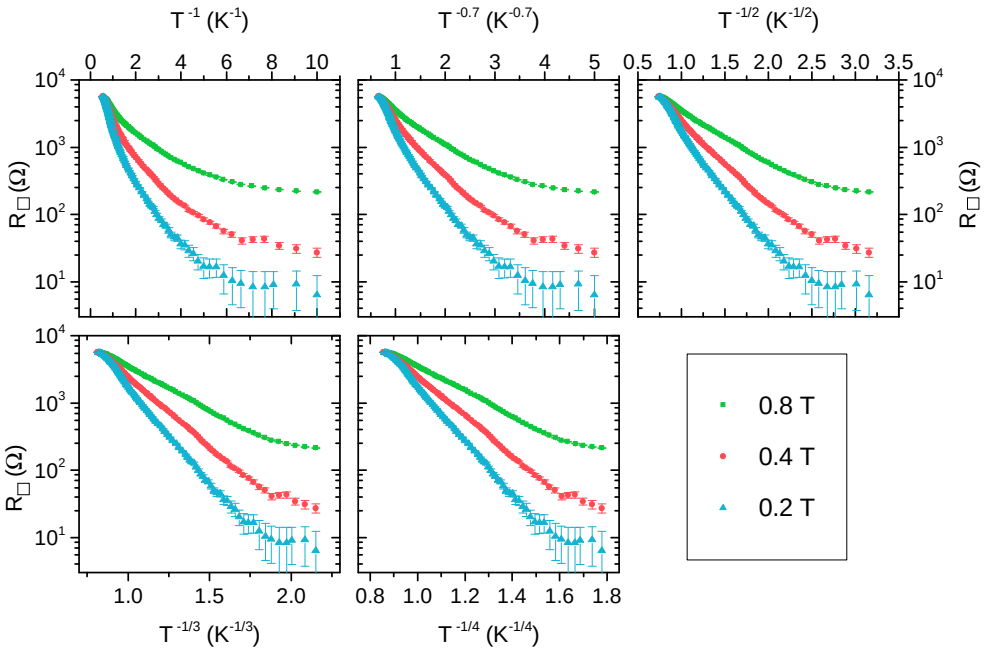

Figure 4.6: The logarithm of R vs. T^p for three representative fields, with $p = 1$, 0.7, $1/2$, $1/3$ and $1/4$.

A more quantitative approach involves linear fitting of the Figure 4.6, and the comparison of $\widetilde{\chi}^2$ (a.k.a. reduced χ^2) calculated for those fits [100]. The quantity $\widetilde{\chi}^2$ evaluates the fit of function $f(x)$ for n data points (x_i, y_i) and is defined as [101]

$$\widetilde{\chi}^2 = \frac{1}{\nu} \sum_{i=1}^{n} \frac{(y_i - f(x_i))^2}{\sigma_i^2} \tag{4.3}$$

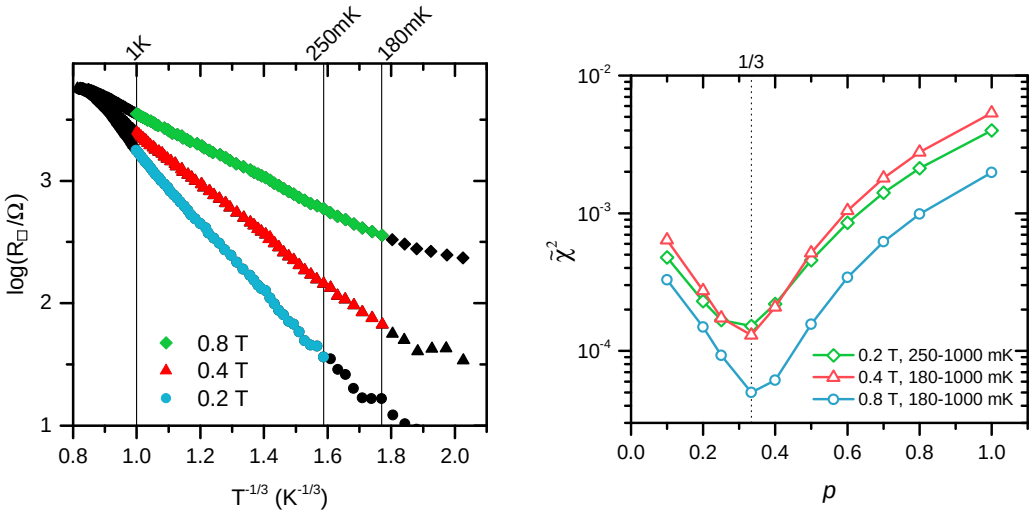

(a) $\log R$ vs. $T^{-1/3}$ plots indicating the temperature range used for the fit evaluation.

(b) $\widetilde{\chi}^2$ as a function of exponent p for fits over the specified temperature intervals, all showing a minimum at $p = 1/3$.

Figure 4.7: Quantitative comparison of fit quality over the ranges of Sample A temperature data and fields shown in (a). (b) shows $\widetilde{\chi}^2$ computed for fits of those data for a set of possible p.

where σ_i is the variance of measurement i, and the quantity is normalized by the degrees of freedom, ν. $\nu = n - m$, where m is the number of fitting parameters in f. A lower value of $\widetilde{\chi}^2$ indicates a better fit, and "best fit" has been found when $\widetilde{\chi}^2$ is at minimum. Figure 4.7 shows that for the data shown in Figure 4.6, $\widetilde{\chi}^2$ reaches a minimum at $p = 1/3$ for fits over a significant portion of the low-temperature data[2].

A third graphical approach employed to verify $p = 1/3$ is a modified version of a Zabrodskii-Zinov'eva plot [102]. This type of analysis was developed to provide a way of manipulating and plotting insulating data of the form $R \propto \exp[(T_0/T)^p]$ such that the data appear as a line with slope $-p$.

[2]The resistance measrurement standard error δR, visible in Figure 4.6, becomes distorted when propagating through to $\delta \log(R)$. As a result, $\widetilde{\chi}^2$ reached a minimum far from $p = 1/3$ when weights were used. This was most true of the 0.2 T data, where a minimum for $\widetilde{\chi}^2$ was found for very small $p \lesssim 0.1$, a result that does not match visual assessments of the data. The best fits for 0.4 T and 0.8 T data also showed some distortion. When weighting was abandoned, with $\sigma_i \to 1$, $\widetilde{\chi}^2$ results agreed with visual assessments, as shown in Figure 4.7.

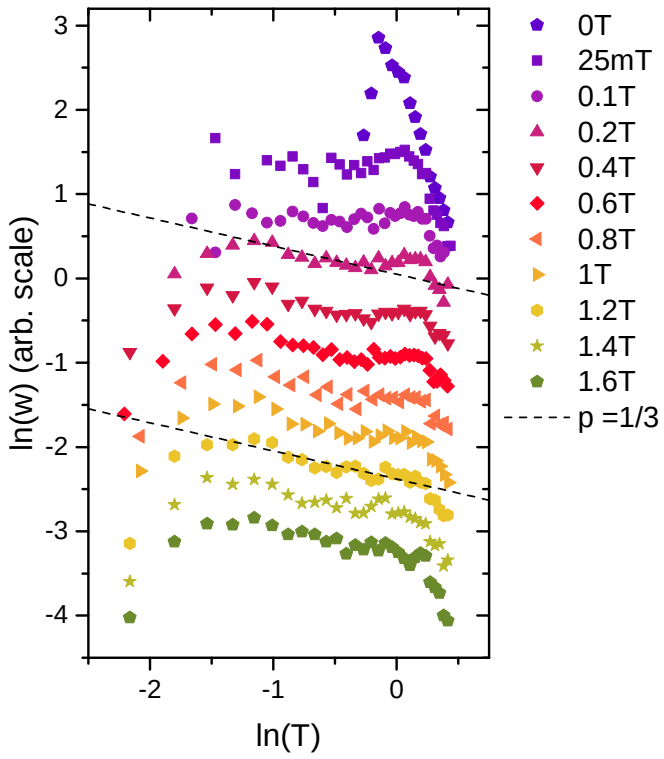

Figure 4.8: Modified Zabrodskii-Zinov'eva plot showing low field conductance data for Sample A. Dashed lines provide a reference for a slope of $-1/3$, corresponding to 2D Mott VRH of vortices.

Data of the form Equation 4.2 are incompatible with the standard Zabrodskii-Zinov'eva approach due to the negative value of the argument in the exponent. However, if resistance data are inverted we expect a conductance of the form

$$G(T) = G_0 \exp\left(\frac{T_0}{T}\right)^p, \tag{4.4}$$

which has the desired sign in the exponential term. Here we assume that prefactor $G_0 = 1/R_0$ is temperature independent, as we do throughout. Stated in terms of $\ln G$ and $\ln T$ this is

$$\ln G = \ln G_0 + \left(\frac{T_0}{e^{\ln T}}\right)^p \tag{4.5}$$

which permits the straightforward evaluation of

$$w \equiv -\frac{\partial \ln G}{\partial \ln T} = p\,(T_0/T)^p\,. \tag{4.6}$$

This quantity proves useful through a second use of logarithms, such that

$$\ln w = C - p \ln T \tag{4.7}$$

is a linear relationship, with intercept $C = \ln(pT_0^p)$ and slope equal to $-p$.

The results of such an analysis for Sample A data is shown in Figure 4.8. The partial derivative used to find w amplifies measurement noise, and despite the use of linear interpolation in an attempt to smooth the data, the noise level here makes linear fitting impractical. Instead, dashed lines with slope $-1/3$ has been provided as a guide for the eye. For fields $B \geq 0.4\,\mathrm{T}$, a portion of the points at the center of the temperature range do appear to line up in agreement with $p = 1/3$. For this set of curves, there is a sharp-sloped high-temperature region, which gives way $\approx$1.3 K to behavior characterized by a gentler slope. This central region of the plots is fairly straight and consistent at the highest fields shown. This central region terminates at a low-temperature cutoff around 200 mK, where the points begin to droop down so that the slope becomes positive. Possible causes for this drooping are discussed in Section 4.1.2.

In figure Figure 4.8, data in the central temperature region observed for $B \geq 0.4\,\mathrm{T}$ visually agree with the lines that show a slope of $-1/3$. At the limiting case $B \geq 0.4\,\mathrm{T}$, a feature at the high temperature end of this region limits the fit agreement to a region corresponding to $\approx 0.2 - 0.9\,\mathrm{K}$. It is possible this feature relates to the onset of the transition region at zero field, which also occurs near 0.9 K. As the field increases, the high-temperature feature in the central region becomes smaller and disappears, so that apparent agreement extends the full width, from $\approx 0.2 - 1.3\,\mathrm{K}$.

At the lowest non-zero fields $0 < B < 0.4\,\mathrm{T}$, the high temperature bump has consumed the central region, depressing the slope from $-1/3$. This flattening can be interpreted as a sign that the prefactor G_0 is not constant, but instead has power-law temperature dependence. It is also possible that in this low-resistance regime, the signal-to-noise ratio was too low for these data to be useful in this type of analysis.

Whatever the case, the $B = 0$ data stick up in a manner inconsistent with any form

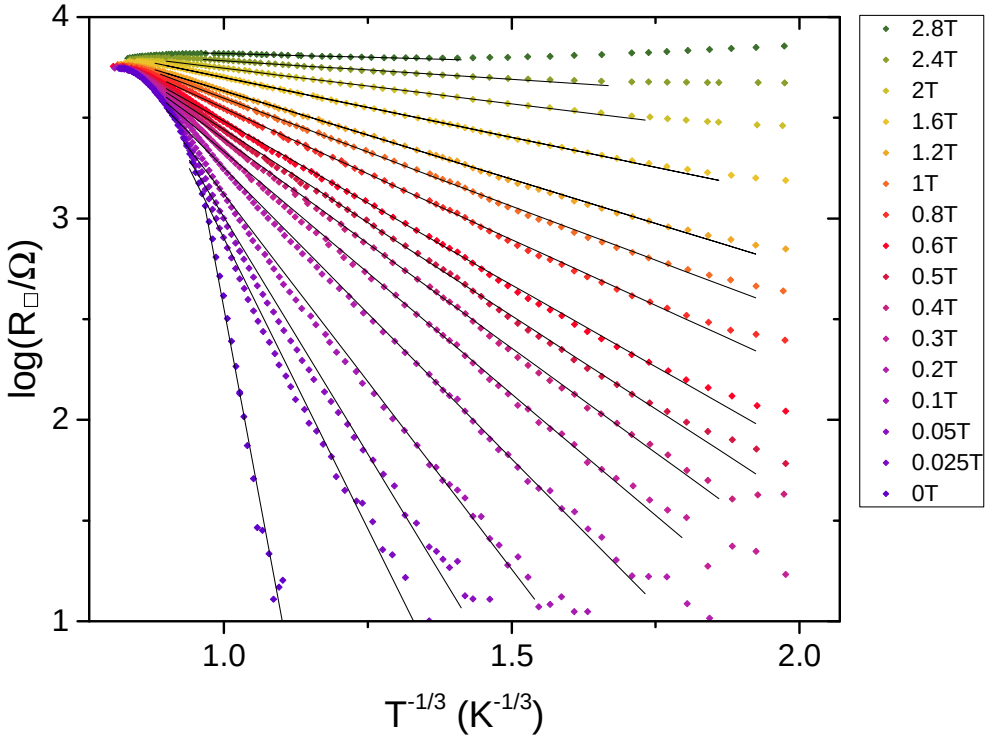

Figure 4.9: The logarithm of sheet resistance vs. Temperature$^{-1/3}$ at various fields within the positive dR/dT regime. The straight lines show fits to the functional form for 2D Mott VRH of vortices.

of vortex hopping. This is very reasonable, given that the free vortex density will be very small in the absence of an applied field.

Figure 4.9 shows a range of data within the $dR/dT > 0$ region, plotted to linearize data with the 2D Mott hopping form

$$R(T) = R_0 \exp\left[-\left(\frac{T_0}{T}\right)^{1/3}\right]. \tag{4.8}$$

Fits to these linearized data are shown as well. For some curves at relatively low field values, the fits describe the data very well over more than two decades in sheet resistance. Values of characteristic temperature T_0 and prefactor R_0 extracted from these fits are shown in Figure 4.10 as function of field. We return to these parameters in the next chapter.

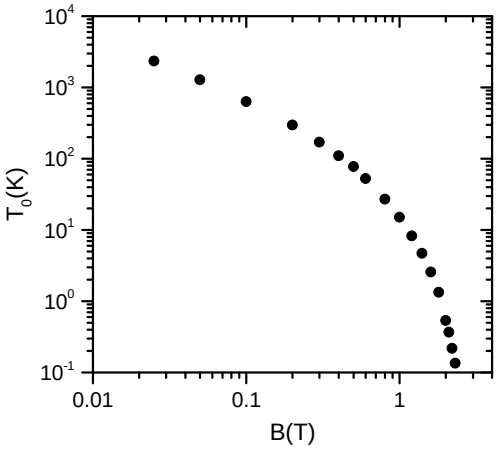

(a) Characteristic hopping temperature T_0 as a function of magnetic field.

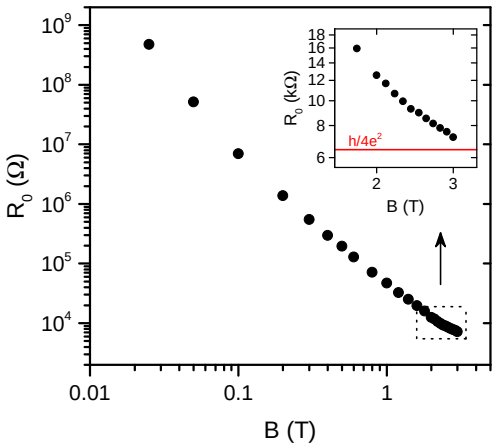

(b) Exponential prefactor R_0 as a function of magnetic field.

Figure 4.10: Values of R_0 and T_0 extracted from fits like those shown in Figure 4.9 to the 2D Mott hopping form Equation 4.8.

Evidence of 2D Mott hopping of vortices was observed in Sample B as well. Samples A and B were grown in similar conditions and have the same nominal thickness. However, R vs T data for Sample B shown in Figure 4.11, indicate it has much stronger superconductivity than in Sample A. Superconductivity persists to higher temperatures, with $T_c = 2.13\,\mathrm{K}$, and the critical field $B_c > 9\,\mathrm{T}$, exceeding the full strength of the PPMS magnet. Thus, this measurement did not allow for observation of the full field-tuned transition, or the behavior of the film on the other side of the transition.

Figure 4.12(a) shows how these data linearize on a log R versus $T^{-1/3}$ plot. The linear region here occurs over a much smaller region than was seen in Sample A, covering only a fraction of a decade in R. Panels (b) and (c) of Figure 4.12 show the evolution of characteristic hopping temperature T_0 and resistance prefactor R_0 as a function of field. These are qualitatively very similar to the equivalent data for Sample A, shown in Figure 4.10.

Sample B data were used to generate the same type of modified Zabrodskii plot described above. This is shown in Figure 4.13. Since cooling is not a concern in PPMS, DC resistance measurements were performed with an integration time $\sim 1\,\mathrm{s}$[3].

[3] The improvement to noise provided by this longer integration time, compared to the pulsed DC measurements ($\sim 10\,\mathrm{ms}$), is extremely clear here.

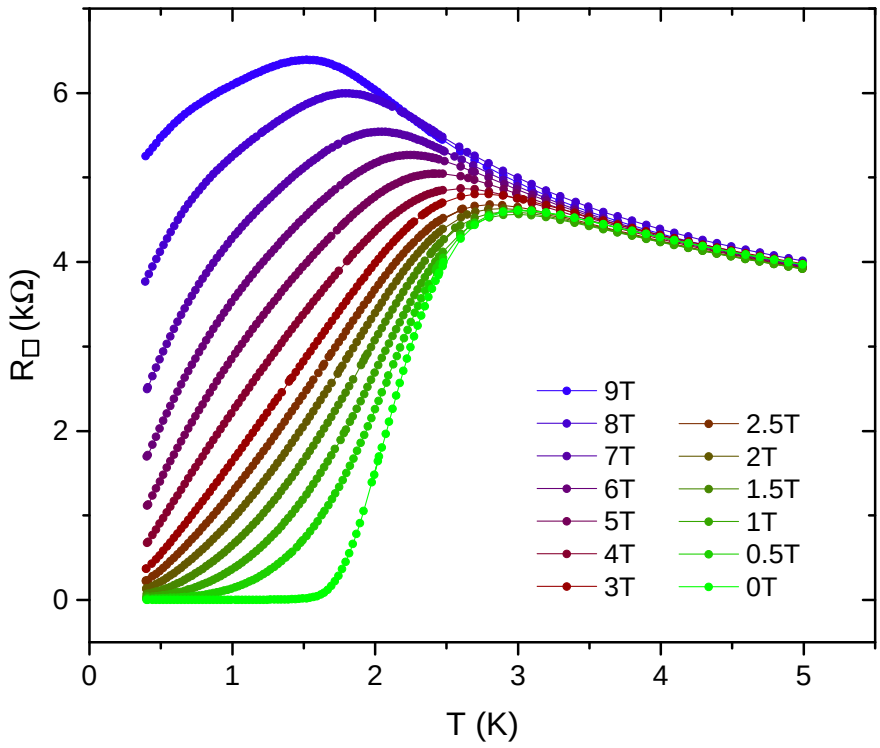

Figure 4.11: Sheet Resistance of Sample B vs. Temperature for $0 \leq B \leq 9\,\mathrm{T}$.

Data for $B \geq 2T$ show linear behavior over a stretch of temperatures, providing strong evidence for vortex hopping in this sample. On each curve, a linear hopping region is bounded by the dropping-off of data at both the high and low end of the data. Linear fits are shown in Figure 4.13. The slopes of these lines, which provide information about the hopping exponent p in Equation 4.2, are plotted in the inset.

These fits indicate an evolution of hopping exponent p with increasing field that in some ways mirrors what is seen for Sample A. The zero-field behavior, for example, follows the same sharp trajectory. With the application of a small magnetic field the trajectory changes radically and becomes flat. Even where there appears to be linearity, the slopes for the data for $B \lesssim 2T$ are too low to correspond to any predicted hopping exponent.

As the field increases p does as well. The exponent passes through $1/3$ around $3\,\mathrm{T}$ and saturates[4] near $p = 1/2$ around $7\,\mathrm{T}$.

[4]It is unclear if the slight drop in slope above $7\,\mathrm{T}$ is real, or if it is an artifact of the data showing

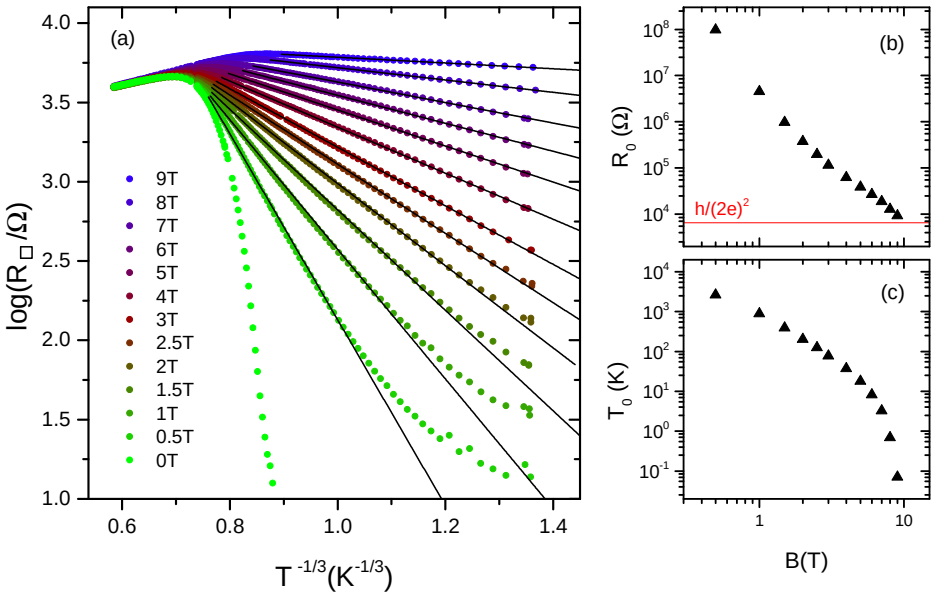

Figure 4.12: (a) $\log R$ versus $T^{-1/3}$ for Sample B along with fit lines to the 2D Mott hopping form Equation 4.8. Parameters (b) R_0 and (c) T_0 as a function of B, extracted from the fits shown in (a).

As discussed in Section 2.3, this is the hopping exponent predicted by Efros-Shklovskii VRH for systems interacting via the coulomb potential. Mott VRH occurs in the absence of interactions. It makes sense that as B increases, thereby increasing vortex density n_v, the interactions between vortices will eventually effect the hopping behavior. The lack of such a crossover in Sample A's data is surprising. However, a crossover to an Efros-Shklovskii hopping form is not expected for vortices, which interact logarithmically, rather than via the coulomb potential.

4.1.2 Possible quantum metallic ground state

Resistance data measured at the lowest accessible temperatures provides the best clue for the quantum ground state of the system. In the last section we showed there is good agreement with 2D Mott hopping of vortices in the low-temperature regime of Sample A. Where this behavior is observed down to the low temperature experimental limit, it is reasonable to assume that this behavior persists down to the zero temperature limit.

$dR/dT > 0$ over only a small number of points in temperature the highest fields.

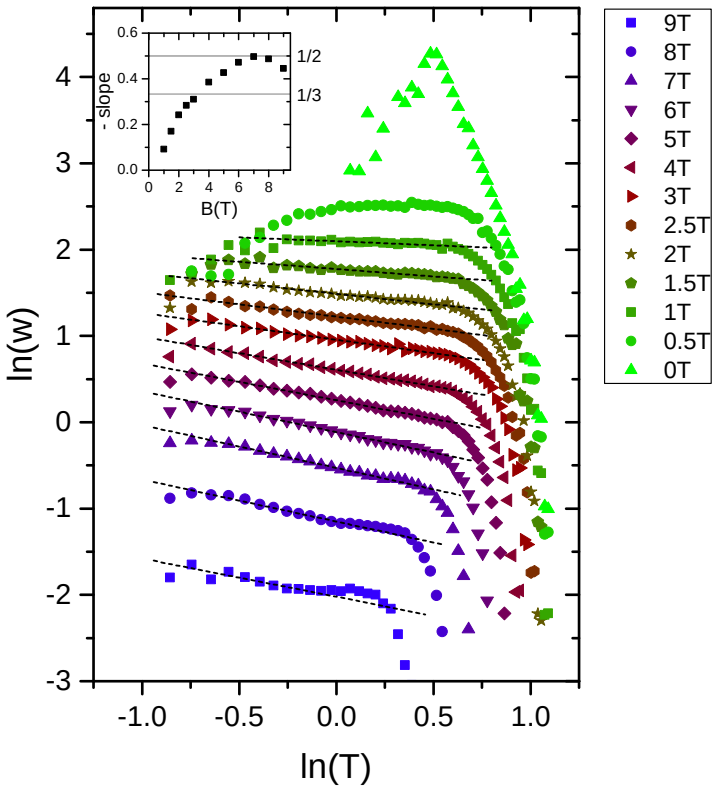

Figure 4.13: Modified Zabrodskii-Zinov'eva plot based on conductance data for Sample B. Data for $B \geq 1\,\mathrm{T}$ were fit to lines. The inset displays the fitted slope as a function of field.

The limiting case of Equation 4.8 is $R(T \to 0) = 0$, such that vortices are frozen into a glassy solid, and the ground state is a superconductor. However, Figures 4.9 and 4.12(a) show that for both Samples A and B, at some or all applied fields, the data depart from hopping behavior at the lowest temperatures.

Determining the quantum ground state from data measured at low temperatures is difficult. On the one hand there are always energy scales below those probed by a given low-temperature experiment, and it is not impossible that some completely different behavior emerges below accessible temperatures. Thus, the lowest-temperature data may provide a vital clue. On the other hand, the basic reality of low-temperature measurement is that the cooling power of fridges, as well as thermal coupling in and between materials, all decrease with temperature. As a result, the risk of systematic

errors in temperature control and thermometry due to sample self-heating is greatest at the lowest temperatures. Thus, interpretation of the lowest temperature data must be done with great care.

The flattening observed here can be a signature of a temperature difference ΔT between the sample and the thermometer. The risk factors for this occurrence in the K25 are discussed in depth in Section 3.2.2. A finite value of ΔT is to be expected in any fridge, though ideally it will be negligibly small even at base temperature. A resistance value at thermometer temperature T will be assigned $R(T)$, though the true value is $R(T + \Delta T)$. For very small ΔT, $R(T) \approx R(T + \Delta T)$. Where ΔT becomes significant, usually below some threshold temperature T_Δ, plotted data stretch out in the temperature direction, artificially flattening out with increasing ΔT. In this case T_Δ should have very weak field dependence.

Flattening was evident in the Sample A data, at temperatures below $\approx 120\,\mathrm{mK}$, regardless of field. Given the issues with cooling experienced with the K25, this was assumed to result from sample heating, and these data are excluded from this study.

Still, this flattening can be seen in Figure 4.4. Figure 4.14 shows a few of these same curves, with $T_\Delta(B)$ marked. These are the points where the data and fitlines differ by greater than 1.5 %. (This is a less stringent criteria than the one used to create Figure 4.7, and verify a minimum for $\widetilde{\chi}^2$ at $p = 1/3$, but the results track.) Here we can see that $T_\Delta(B)$ is strongly field dependent. At low fields $T_\Delta(B)$ is high, but also seems to occur where the curve meets the (high) noise floor. At higher fields, $T_\Delta(B)$ increases again, here as point of separation between $dR/dT > 0$ and $dR/dT < 0$ behaviors, i.e. the SIT. A quantum metal is expected at the quantum critical point [35].

A second possible explanation for the flattening is the onset of a quantum metal ground state, which occurs over a broader range of fields than just the quantum critical point. Twenty years ago, reports began to emerge of vortex hopping giving way to temperature independent behavior at low temperatures. This was initially reported by Ephron et al. in the 1990's, who observed this in amorphous MoGe thin films [23]. In this work, the authors also examined the likelihood that the temperature independence could be caused by sample heating, looking to T_Δ for clues. In this case, T_Δ was found to depend strongly on perpendicular magnetic field, and decreased with increasing field. Unlike the Sample A data presented here, the noise floor of the MoGe

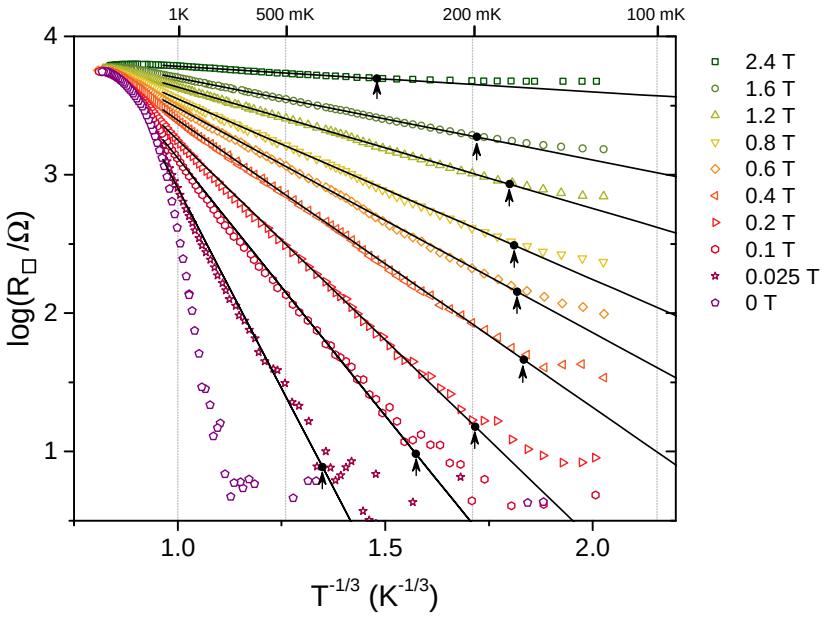

Figure 4.14: $\log R$ vs. $T^{-1/3}$ at various fields within the positive dR/dT regime. The straight lines show fits to the data showing agreement with Equation 4.8. Dark dots indicate $T_\Delta(B)$, the set of temperatures where the data deviate from this functional form.

resistance measurement was well below the saturation value of the resistance at low fields, unambiguously indicating that the phenomenon could not be explained by local heating effects. Instead, it was interpreted to be the onset of a metallic ground state.

This field-induced metallic behavior has subsequently been observed in additional MoGe samples [24] as well as in numerous other amorphous materials, such as MoSi [26], Ta [27], and InO [66], all showing T_Δ to decrease with applied field. The same pattern of behavior has been observed in ultra-thin crystalline materials such as $NbSe_2$ [28] and ionic-liquid gated ZrNCl [77]. Since this low-temperature metallic state cannot be explained by Fermi liquid theory, an alternative description has been sought. There has been little consensus as to the best approach, with descriptions of the system as a Bose metal [78–81], as a vortex metal [82, 83], and as a failed superconductor [31]. There is no consensus over the proper approach.

A very recent preprint [30] throws this entire body of work into doubt. Two thin superconducting films, one of highly disordered InO_x and the other of exfoliated single

crystal 2H-$NbSe_2$, provide evidence of the intermediate metallic state in one measurement environment. In a second measurement environment with improved shielding and filtering of external radiation and noise, neither sample exhibits a metallic regime. 2D superconductors, they argue, are extremely sensitive to noise and prone to Joule heating. In light of this, it seems reasonable to conclude that the departures from the hopping form for Sample A at low temperatures are artifacts of measurement.

Sample B is a different case. Compared to the K25, the disadvantage of the PPMS for determining the quantum ground state of the system is its continuous-mode base temperature of 400 mK. The lowest energy scales probed by these measurements are 3-4 times higher than those accessible to the K25. However, the thermometer is very near to the sample stage, which affords much higher degree of confidence in the lowest-temperature data.

In Figure 4.12(a) the data agree with fitlines indicating 2D Mott vortex VRH temperature dependence down to base temperature for $B \geq 2.5\,\mathrm{T}$. However, for $B \leq 2\,\mathrm{T}$ there is departure from the hopping form at low temperatures. At lower fields, the curves trend upwards and away from the fitline, such that T_Δ nearly reaches 1 K when $B = 0.5\,\mathrm{T}$. While this does have the hallmarks of a resistance saturation such as that reported in Ephron et al. [23], a better answer can be found by considering Figure 4.13. At the lowest fields, this shows that the effective hopping exponent is much lower than $1/3$. While we are unable to physically explain the temperature dependence at this field, it is clear that it is neither consistent with 2D Mott hopping of vortices, nor total temperature independence.

4.2 $dR/dT \approx 0$: The transition region

In the SIT paradigm, a temperature-independent, zero slope separatrix on an R vs. T plot occurs at the critical value of the tuning parameter, and points like an arrow to a resistance value at the quantum critical point. On a plot showing resistance as a function of the tuning parameter, isotherms will cross at the single-valued critical field.

Finite-size scaling analysis methods are customarily applied to finite-temperature data around the quantum critical point, because these data contain the signature of quantum critical fluctuations. In the vicinity of a continuous quantum critical point,

resistance has the temperature dependence [43]

$$R = R_c f\left(\delta/T^{\nu z}\right) \tag{4.9}$$

where R_c is the critical resistance, f is an arbitrary function, and δ indicates the distance from the critical value of the tuning parameter. For the field-tuned transition $\delta = |B - B_c|$. The quantities ν and z are the correlation length and dynamical critical exponents, respectively. These values place the transition into one of a limited number of universality classes which encompass the vast breadth of continuous phase transitions in nature. These exponents are considered "universal" because they relate to the underlying ordering symmetry and mechanism of the transition, rather than microscopic details of a sample.

Practically speaking, the value of exponent product νz can be extracted by plotting the isotherms as a function of $\delta/T^{\nu z}$ and varying νz until the data collapse into a single curve [43].

Data presented here differs from the paradigmatic field-tuned SIT in a few ways. While Fig. 4.2 gives the appearance of a critical field around 2.8 T, closer inspection reveals a range of critical values. Such a view is provided in Fig. 4.15, where the isotherm crossings trace a path through R vs. B space. On the R vs. T plot in Fig. 4.4, the smearing of the transition manifests as the lack of a clear separatrix. Instead, flat portions are distributed across the range of fields from 2 to 3.2 T. (Zero slope points on the R vs. T plot correspond directly to the crossing points on the R vs. B plot.)

The smearing of the transition over a range of critical values doesn't automatically preclude finite-size scaling analysis, despite the intrinsic difficulty in determining a single value of B_c. (At best B_c can be defined only within the resolution of the measurement.) A notable example of this is the historic work from Hebard and Paalanen [39] where scaling was first applied to a field-tuned transition.

However, the data presented here were not found to collapse convincingly for any single value of exponent product νz. Some recent papers [103, 104] assert that the breakdown of finite-size scaling at smeared transitions can be understood as evidence of a different sort of critical point, the infinite randomness critical point, where activated scaling is expected instead of power law scaling [105]. Full exploration of this possibility

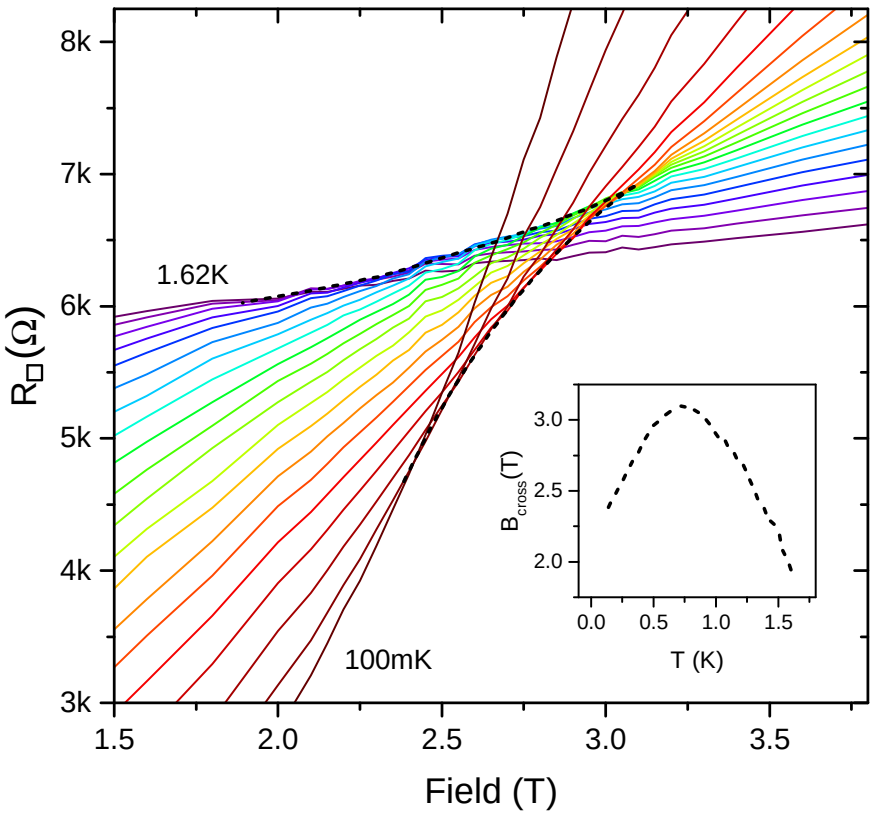

Figure 4.15: Resistance vs. magnetic field showing the crossover region. The line of crossings between isotherms is highlighted by a dark dashed line. These crossing fields are plotted as a function of temperature in the inset.

goes beyond the scope of this dissertation.

It is worth noting that the crossings seen in Hebard and Paalanen's data smear in a manner consistent with the thermodynamic evolution of the critical field. H_c is expected to increase as the temperature decreases and superconductivity becomes more robust. They took their quantum critical value B_c to be the lowest crossing temperature of the bunch. In the data presented here, crossings above $\approx$0.8 K evolve in this way, but at the lowest temperatures, crossing field $B_{cross}(T)$ increases with temperature. There is no clear explanation for this behavior.

Though the data do not collapse to a single value at any νz, they do support the concept of duality symmetry that was laid out by Matthew Fisher in his prediction

for scaling at the field-tuned SIT [35]. Fisher's model relies on the quantum dual relationship between Cooper pairs and vortices, and their competition at the critical field. Below a critical field, a condensate of Cooper pairs support a superconducting state, where vortices are localized at pinning sites. Above the critical field, the vortex density is great enough that they Bose-condense, localizing Cooper pairs. Right at the critical field, neither boson is able to condense as the system fluctuates between the two competing ground states. Here, the system can be described as "self-dual" and is effectively a metal. Despite the differences between Cooper pairs and vortices (primarily in the form of their interactions,) Fisher predicted there to be a common mechanism behind transport in the two quantum states. His dual Hamiltonian gave rise to the relationship between particle resistivity and conductivity tensors ρ and σ and vortex resistivity and conductivity tensors ρ^v and σ^v. Specifically, $\tilde{\rho} = \tilde{\sigma}^v$ $\tilde{\sigma} = \tilde{\rho}^v$ where the tilde indicates that quantities are normalized by the quantum resistance for pairs.

Here, the measured sheet resistances stand in for the diagonal terms of the tensor, and the much smaller off-diagonal terms will be ignored. Written in notation applicable to the data presented here, Fisher's duality relationship becomes

$$\tilde{R} = (\tilde{R}^v)^{-1} = \tilde{G}^v \tag{4.10}$$

where, as before, the tilde refers to normalization by the quantum resistance, so that normalized sheet resistance $\tilde{R} = \frac{4e^2}{h} R_\square$, normalized sheet conductance $\tilde{G} = \frac{h}{4e^2} G_\square$, and so on. At the transition point, self-duality requires $\tilde{R} = \tilde{G}^v = \tilde{G} = \tilde{R}^v \approx 1$.

If the transport mechanism is truly shared between Cooper pairs and vortices, then duality symmetry is predicted in the vicinity of the critical point. Specifically, if the resistance at a field $B_{sc} < B_c$ is $\tilde{R}_{sc} = \tilde{R}(T, B_{sc})$, there should be a partner field $B_{ins} > B_c$ and $\tilde{R}_{ins} = \tilde{R}(T, B_{ins})$, a at which the charge/vortex roles have swapped, such that $\tilde{R}_{sc} = \tilde{R}^v_{ins}$ or

$$\tilde{R}_{sc} = \tilde{R}^{-1}_{ins}. \tag{4.11}$$

This kind of symmetry was first found by Sambandamurthy et al. in indium oxide films. These show power-law temperature dependence of magnetoresistance described

by the phenomenological form [60, 64, 106]

$$\frac{R(B,T)}{R_c} = \left(\frac{B}{B_c}\right)^{P(T)}. \tag{4.12}$$

Here, B_c is the critical field, the critical resistance R_c, and P is the temperature-dependent power determining $R(B)$. They found their $R_c \simeq h/4e^2$, so that the left hand side of Equation 4.12 becomes $\tilde{R}$.

Power-law temperature dependence was observed across the transition in Sample A as well, as is shown in Figure 4.16 where several representative isotherms demonstrate linearity on double logarithmic axes. As in the works mentioned above, Equation 4.12 describes the data not just in the critical region but over multiple decades in resistance, at least a decade in field, and almost a decade in temperature. The bulk of this phase space occurs at fields below the transition, but the fits continue to describe the data into the insulating regime. At the highest and lowest isotherms shown, the data are within 2% of the power law fit all the way up to the MR peak, where the magnetoresistance changes sign entirely. Isotherms at intermediate temperatures were found to "droop" away from the low-field power-law fits, departing at fields down to 6 T. Ovadia et al. suggest that power-law dependence is robust over the domain where the insulator can be characterized as a vortex condensate [64]. They reason that departure from power-law magnetoresistance indicates a crossover from a Bose to a fermionic insulator, where local pairing potential has been destroyed.

The inset in Figure 4.16 shows the values of $P(T)$ as extracted from fits like those shown in the main panel. The temperature dependence of P takes the form found by Tamir et al. [106]:

$$P(T) = \frac{T_{PL}}{T+\theta} \tag{4.13}$$

where T_{PL} and θ are described as sample specific parameters. The values measured here, T_{PL} =0.67 K and θ =0.09 K are consistent with the values presented in that work for films with B_c similar to the set of $B_{cross}(T)$ for Sample A.

The power-law magnetoresistance observed in these samples is very friendly toward

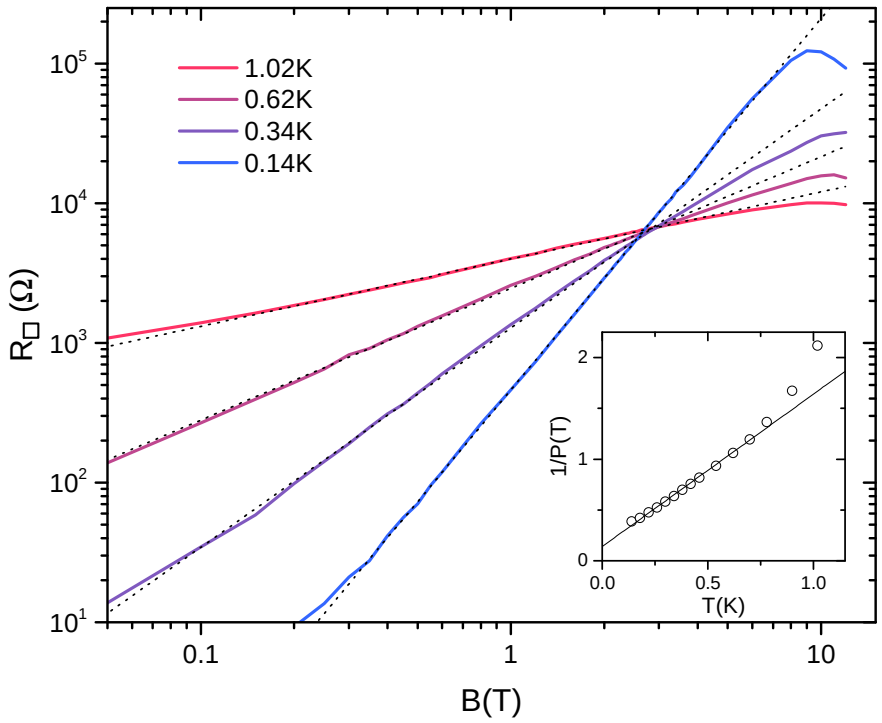

Figure 4.16: Log-log plot of resistance vs. magnetic field at several temperatures, showing power law magnetoresistance ($R \propto B^{P(T)}$) through the transition. The inset shows inverse power as a function of temperature with a fit to Equation 4.13.

determination of paired fields B_{sc} and B_{ins}. Combining Equation 4.11 with Equation 4.12 gives

$$\left(\frac{B_{sc}}{B_c}\right)^{P(T)} = \left(\frac{B_c}{B_{ins}}\right)^{P(T)}, \tag{4.14}$$

which simplifies to

$$B_{sc}B_{ins} = B_c^2, \tag{4.15}$$

a definition for the paired fields mentioned above. Substituting this back into Equation 4.14 gives the relation

$$\tilde{R}_{sc}\tilde{R}_{ins} = 1. \tag{4.16}$$

Assessment of whether the data for Sample A meet the criteria set out in Equations 4.15 and 4.16 is complicated by the temperature-dependence of crossing fields and

resistances. The set of points $B_{cross}(T)$ calculated from adjacent isotherms 120 mK to 1.52 K were treated statistically to determine $B_c = 2.8 \pm 0.3$ T. From this value, sets of fields were chosen with $B_{sc} = B_c/n$ and $B_{ins} = B_c * n$. Curves for $\tilde{R}_{sc}(T)$ and $\tilde{R}_{ins}(T)$ were determined by linear interpolation for various n. These curves were found to satisfy Equation 4.16 over the full temperature range through $n = 2$.

Another, similar basis for comparison comes in the context of the 2D Mott VRH conduction observed for this sample. The exponent $p = 1/3$ permits a generic form for the resistance $R(T, B) = R_0(B) \exp[(T_0(B)/T)^{1/3}]$, which can describe either side of the transition depending on the sign of T_0. Equation 4.11 applied to this case gives $R_0(B_{sc}) = R_0(B_{ins})^{-1}$ and $T_0(B_{sc}) = T_0(B_{ins})^{-1}$.

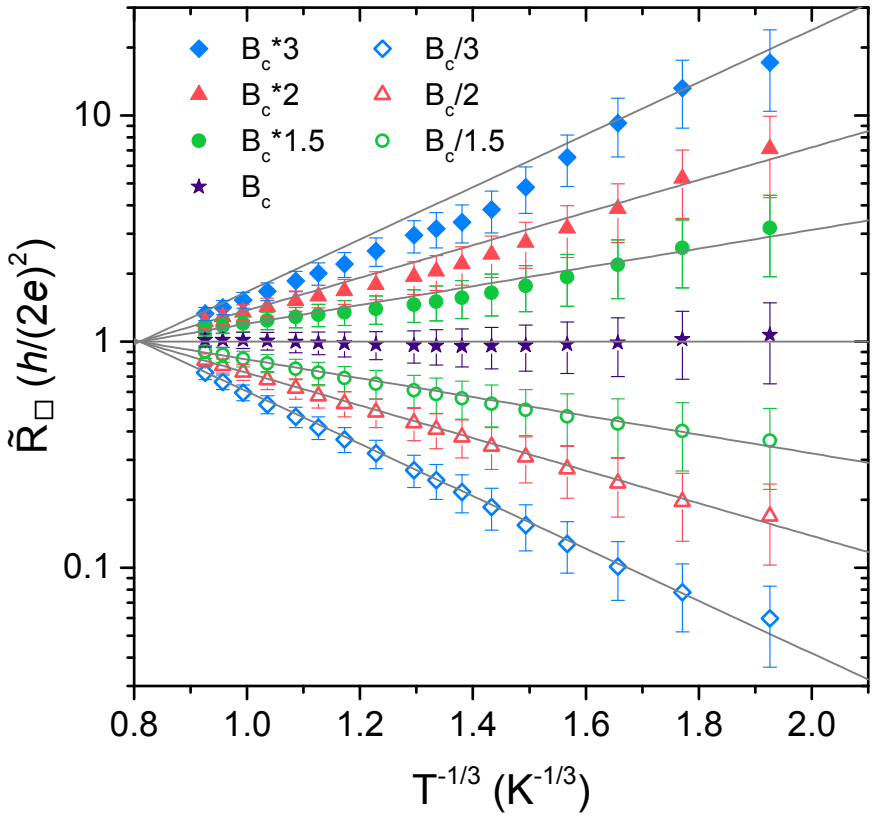

Figure 4.17: $\log R vs. T^{-1/3}$ for pairs $\tilde{R}_{sc}$ and $\tilde{R}_{ins}$. The lines on the bottom half of the plot are fits to $\tilde{R}_{sc}(T)$, and the the lines on the top half are the inverse of these fit functions, plotted for comparison with $\tilde{R}_{ins}(T)$.

Figure 4.17 shows R vs. T data for pairs of fields at $n = 1.5, 2$ and 3. These data are normalized by the quantum resistance and plotted against $T^{-1/3}$ to linearize $R_{sc}(T)$, which were then fit. These fits appear as grey lines on the plot, and the inverse of these fits have been plotted as well, for comparison with the high field data. Here we can see that values agree within uncertainty up through $B_{ins,2} = 2B_c = 5.6\,\mathrm{T}$. At $B_{ins,3} = 8.4\,\mathrm{T}$, a field approaching the MR peak, the data no longer agree with the dual fit within uncertainty over the full temperature range. The dual mapping in this sample is surprisingly robust in the insulating regime, where the behavior is otherwise very complex.

4.3 $dR/dT < 0$: the insulating region and MR peak

Figure 4.18 shows $R_\square$ vs T data at fields above the critical field at Tesla intervals.[5] In this region, all curves show $dR/dT < 0$ at the lowest temperatures, a behavior that points to but does not guarantee an insulating ground state. Better evidence for an insulator can be found by fitting these data to a temperature-dependence that extrapolates to $R \to \infty$ in the $T \to 0$ limit.

The expected form for the insulating state is the hopping form that by now should be very familiar:

$$R(T) = R_0 \exp\left(\frac{T_A}{T}\right)^x. \tag{4.17}$$

In the previous section, it was argued that the $R(T)$ data form symmetric pairs around the critical field B_c of an SIT. This would imply that in the insulating state, the same Mott hopping form observed for vortices below the transition, with $x = 1/3$ in Equation 4.17. However, the temperature-dependence of B_c afforded a margin of error around 10% for this description.

Closer scrutiny reveals that 2D Mott VRH of charges does not best describe the data in this regime. In Figure 4.5 which shows the full span of data as $\log R$ vs $T^{-1/3}$, large deviations from linearity are clearly visible at high fields $B \gtrsim 8\,\mathrm{T}$, near the MR peak.

[5] Data presented with the label "7 T" deviate from the curves formed by the rest of the data. It is likely there was an error with the power supply during the magnet ramp, causing it to enter persistent mode before reaching full field. Interpolation indicates $B_{7T} \approx 6.5\,\mathrm{T}$. This was not without precedent, but in other instances the errors were detected and the measurements repeated. The data are included here for completeness, but omitted from many other plots.

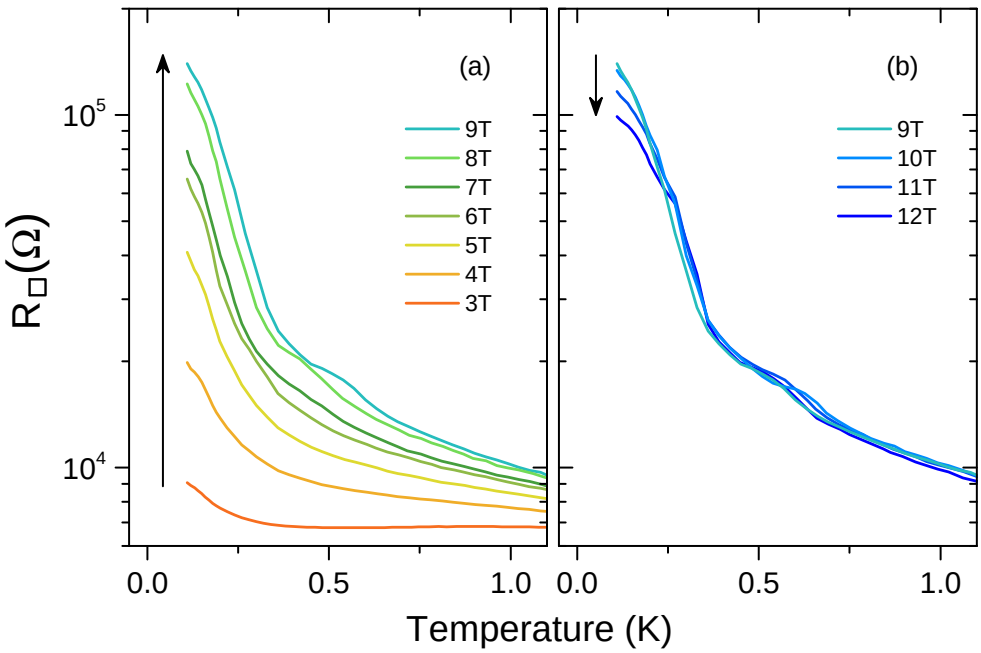

Figure 4.18: Resistance vs. Temperature at fields spanning the insulating portion of the data in Tesla increments, with (a) showing data on the low-field side of the MR peak, and (b) showing the high-feild side of the magneoresistance peak. The arrows indicate the direction of increasing magnetic field.

There is no region of linearity for intermediate fields within the $dR/dT < 0$ regime, either.

The lack of 2D Mott hopping temperature dependence is also evident in the Zabrodskii-Zinov'eva plot of the data shown in Figure 4.19. This method of plotting data, described in Section 4.1.1, shows agreement with the stretched exponential form in Equation 4.17 by revealing x as the slope of the data. Unlike the analysis in Section 4.1.1, the quantity w is defined here as

$$w = -\frac{\partial \ln R}{\partial \ln T},$$

following the original paper [102].

Included with the data plotted in Figure 4.19 are two line segments which indicate the slopes expected for hopping exponents $x = 1/3$ and 1. There is no significant region where the data show $x = 1/3$. However, there is a low temperature region, spanning

$3\,\mathrm{T} \lesssim B \leq 6\,\mathrm{T}$, that agrees reasonably well with $x = 1$, the hopping exponent for thermally activated conduction.

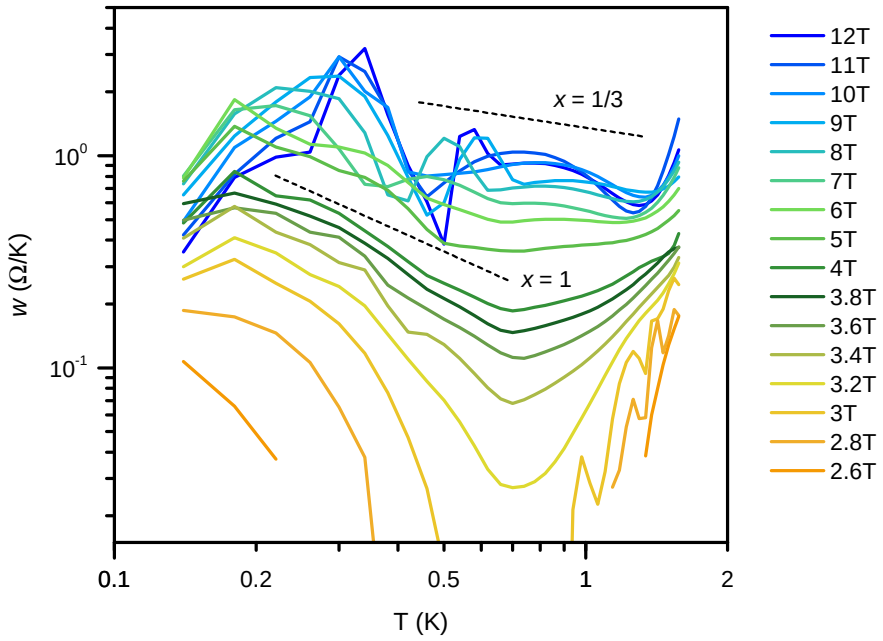

Figure 4.19: A Zabrodskii-Zinov'eva plot of high field data. Dotted line segments show the slope expected for activated conduction ($x = 1$) and 2D Mott hopping of charges ($x = 1/3$).

Figure 4.20(a) shows the logarithmic resistance data plotted against $1/T$ to highlight activated hopping behavior. Good quality fits were obtained for these data for the field range described above, and the fit lines are shown on the figure. The linear field dependence of the activation energies for these fits are shown in Figure 4.20(b). This temperature dependence explains the "droopy" resistance values observed at intermediate temperatures ($\approx 0.4\,\mathrm{K}$) in Figures 4.16 and 4.17. Data that obeys $\log R \propto T^{-1}$ will appear concave up when plotted as $\log R \propto T^{-1/3}$.

For fields above 6 T, the complicated R vs T data cannot be fit to any expected temperature dependence. This has much to do with mysterious features of the data that begin to emerge at fields $B \gtrsim 8\,\mathrm{T}$, meaning they coincide with the MR peak, and appear as ripples in Figures 4.19 and 4.20. In Figure 4.18, the appearance is that of bumps in $R(T)$ curves in the vicinity of 0.5-0.6 K, but is more likely a resistance dip

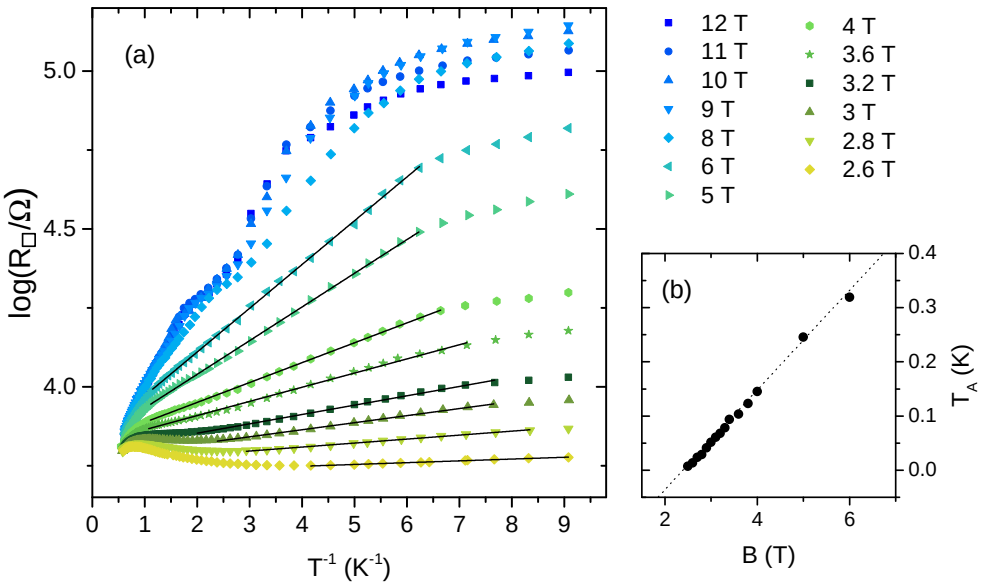

Figure 4.20: Activated conduction of charges in the insulating region of behavior. (a) shows $\log R$ vs $1/T$ data at various fields, with linear fits where applicable. (b) shows the linear dependence of activation energy T_A from Equation 4.17 on applied field B.

closer to 0.3-0.5 K. There is no obvious cause for such ripples in the data, and whatever they are, they are not robust. Other measurements of Sample A in high field show no sign of these features.

Increasing the magnetic field above the critical value causes the sheet resistance of Sample A to increase to a maximum value at around 9 T, beyond which magnetoresistance is negative. This striking magnetoresistance (MR) peak is most clearly visible from the $R(B)$ isotherms in Figure 4.2, rises to a peak value $R_{peak} \approx 25 \times R_c$ at 100 mK.

The MR peak is a characteristic feature for InO_x films driven into an insulating state by perpendicular fields [38,58,59,63,107,108], and even films without a superconducting transition at experimentally accessible temperatures due to localizing disorder [38, 61]. Similar peaks have occured in strongly disordered films polycrystalline TiN films [109] as well as amorphous Bi on mesoscopically undulating substrates [110, 111]. The uniting feature of these systems is a high degree of disorder, with samples characterized as having the strongest disorder leading to the most dramatic peaks [38, 59].

The insulating state just above the SIT is understood to be a Bose insulator in the

context of the dirty Boson theory. Here, localized Cooper pairs exist within a vortex superfluid. Kowal and Ovadyahu first proposed the idea that the localization length of these superconducting islands could be mesoscopic, and render the insulating films as effectively granular [57]. As mentioned in Section 4.2, the change of direction of the MR at and over the peak signifies a transition or crossover from the Bose insulator to a more standard electron-insulator. Some authors have found that the peak location roughly corresponds with the pair-breaking field $B_{c2}(0)$ [38, 59].

A few more detailed theoretical accounts of this effective granularity have been proposed. It has been shown theoretically [112,113] that disorder can lead to very strong spatial variation in superconducting pairing amplitude Δ. This leads to regions with strong pairing intermixed with areas where Δ is depressed close to zero at temperatures far T_c, resulting in what are effectively superconducting islands in a normal background. The islands of strong superconductivity Josephson couple with one another to form a percolative network across the sample. The application of a magnetic field has been shown to reduce the size of these islands, as well as Δ, reducing the coupling strength between the islands so that eventually phase coherence is lost [114].

Another strength of this theory is that it has more recently been extended to predict activated conduction [115]. The activated transport observed in Sample A is consistent with the majority of systems displaying an MR peak, despite the fact that highly disordered films are expected to show VRH in the insulating state [58, 108, 110, 111].

An alternative theory for the MR peak predicts conduction by VRH [116]. VRH has been observed in a few systems in the vicinity, but not actually at the lowest temperatures, of the MR peak [38, 57, 61, 63].

Like the low-field data, these curves depart from hopping temperature dependence at the lowest temperatures. Just as in the low temperature case, it is necessary to evaluate whether this behavior indicates a shift between behaviors belonging to a low-temperature and high temperature regime, or whether it is an artifact of measurement. Here, the onset temperature increases with both field and the resistance of the sample, the expected signature for failure to cool the sample. It is worth noting that flattening has been observed by Steiner et al. at the MR peak in highly disordered InO_x [59]. These data were doubtless subjected to the same scrutiny applied here, and deemed to be intrinsic to the sample, so there is some possibility that this is also the case for

Sample A.

A potential issue with this explanation is that the departure temperature appears to keep rising in temperature as the magnetic field increases, even as the resistances go down with field on the far side of the MR peak. If heating were due to the sample alone, we would expect the onset of a temperature gradient to track the sample resistance directly. However, it is probable that the contact resistances have positive MR over the full range of fields. Additionally, though the solid copper sample holder and cold finger of the refrigerator were designed to reduce eddy currents, those cannot be eliminated entirely and scale linearly with field. Any mechanical vibrations in the fridge system will cause heating that may become important at high fields. These realities point to heating at the lowest temperatures and highest fields.

4.4 Sample structure and disorder

Disorder is clearly important in defining the electronic behavior of these films. In this section, information on the microstructure of Sample A will be presented.

The films used in this study were been grown using the methods developed and documented by Zvi Ovadyahu and his group, as was discussed in Section 3.1.1. For numerous studies they have used electron diffraction to confirm amorphous structure in InO_x films with wildly varying properties [50, 51, 55, 57]. We assume Samples A (and B) are structurally disordered on the atomic scale as well, without crystalline inclusion, though this was not confirmed experimentally.

In early studies of InO_x, resistance uniformity between co-deposited samples lead to description of the material as "homogeneously disordered" [55], a label also applied to quench-deposited metals. More recent work casts doubt on the applicability of this label. Kowal and Ovadyahu found that the uniform behavior observed in macroscopic samples ($\sim$ mm) broke down for very small samples. Co-deposited samples of the same width, with lengths from $\sim 10^{-1}\,\mu$m to $\sim 10^{2}\,\mu$m, showed length-dependence in activation energy as well as critical behavior [53]. This indicated the presence of mesoscale percolative paths in these films. In a later study from the same group, Givan et al. used high resolution STEM combined with chemical probes to observe meso-scale structures ($\approx 10 - 80\,$nm) showing variation of stochiometry within amorphous InO_x films [51].

These were present in both a low-n insulating film and a high-n superconductor, where the observed variation in chemical content would likely have a significant impact on local carrier density, mobility, and thus, superconducting pairing amplitude.

A very detailed analysis of the structure of InO_x produced by pulsed laser deposition is presented in Reference [117]. The authors employed a battery of detailed simulation methods to describe the microscopic structure of this material as related to deposition conditions as well as room temperature performance as a semiconductor. The authors do not explore superconductivity. Pulsed laser deposition is much higher-energy deposition process than the electron-beam evaporation process used to create the samples under study here. Still, it is likely that the amorphous films have comparable microstructure [118].

These studies of InO_x microstructure provide a window into a source of mesoscale disorder, that can arise in amorphous binary superconductors, which show the MR peak, that is not available to amorphous elemental metals, which do not.

There is significant evidence that inhomogeneity within Sample A occurs on a large lengthscale, or a range of lengthscales. As mentioned in Section 4.1, the broad transition to superconductivity in zero field provides evidence of variation in local pairing strength Δ, across the sample. The smearing of crossing point B_c may also result from the presence of rare, large regions within the sample [103, 105].

Another clear indicator of non-uniformity within this sample is anisotropy in its resistance and critical behavior. As mentioned in Section 3.1.2, the sample is a $360\,\mu\text{m} \times 360\,\mu\text{m}$ square designed for the Van der Pauw resistance method. A uniform sample with this symmetrical geometry would be expected to show $R_{\updownarrow} \approx R_{\leftrightarrow}$, where these refer to four-terminal resistance measurements with current running in the vertical and horizontal directions across the sample, respectively.

Figure 4.21 shows the considerable anisotropy in the two orthogonal measurement directions, as illustrated by resistance isotherms as a function of magnetic field. The data look extremely similar, with the expected features of a (smeared) crossing point and MR peak. However, it looks like they have been translated away from each other on the plot. Vertical resistance component $R_{\updownarrow}$ looks like it has been shifted up and away from $R_{\leftrightarrow}$ on these axes because it is consistently about 30% larger. This difference is more than can be accounted for by a 10-15% uncertainty related to the finite size of the

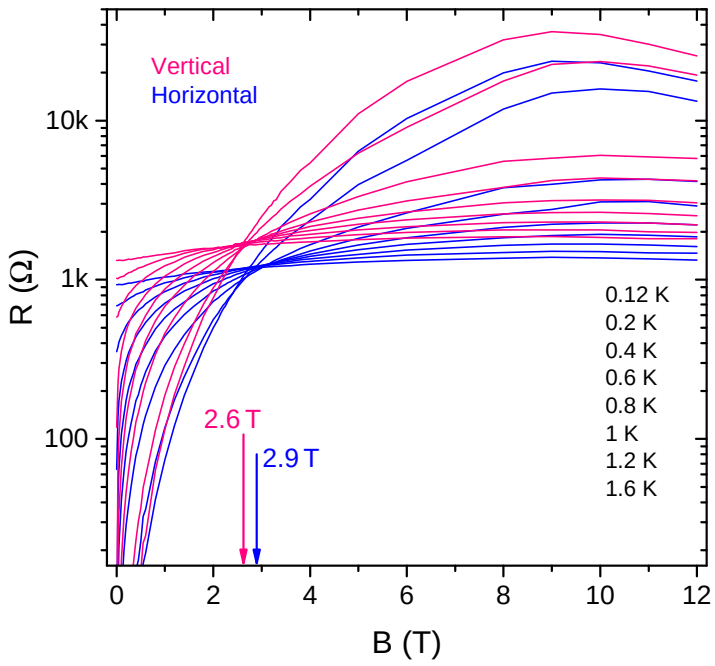

Figure 4.21: R vs B as measured along two orthogonal directions of the square sample. Isotherms are presented for $T = 120\,\text{mK}$, 0.2, 0.4, 0.6, 0.8, 1.0, 1.2, and 1.6 K. The arrows indicate the location of average crossing fields in the horizontal and vertical directions.

contacts [70]. While this could potentially be explained by a thickness gradient across the sample, measurements of step height using both AFM and profilometer data around the edges of Sample A indicate uniform thickness.

$R_{\leftrightarrow}$ appears shifted to the right of $R_{\updownarrow}$ because ordering occurs 0.3 T higher in this direction.

Sample A has an area several times larger than the largest samples in Kowal and Ovadyahu's study, but the result is similar. Anisotropy in the resistance and scaling across a square sample indicates that either there are structures present that are significant compared to the size of the sample.

Atomic force Microscopy performed on a Bruker Nanoscope V Multimode 8 SPM in tapping mode. AFM micrographs were made at a number of randomly chosen spots to probe the surface morphology of Sample A. Three of these micrographs–squares with 1 μm or 0.75 μm on a side–were used to determine statistics of the surface morphology.

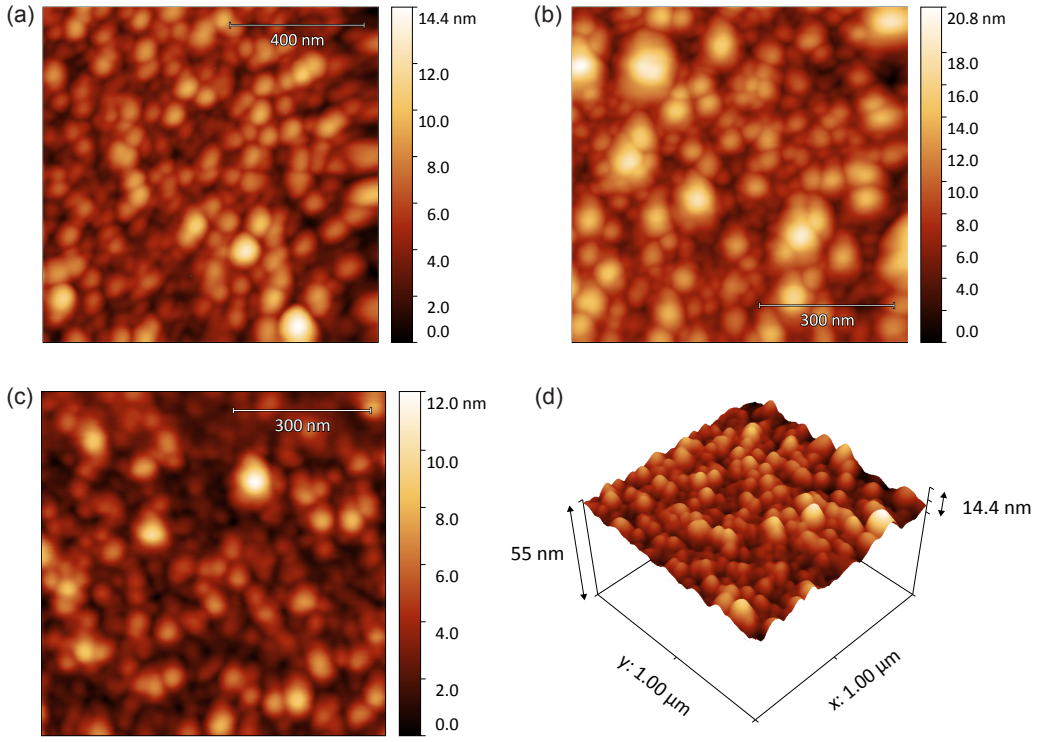

Figure 4.22: Atomic force microscope data for three locations on the surface of Sample A, with (a)-(c) showing the film height on a false-color scale, and (d) a 3d projection of the data from (a) rendered as a 3D projection. The z scale is $\approx 8\times$ the scale of x and y and has been drawn to show the scale of the surface morphology with regard to average film thickness.

These are shown in Figure 4.22(a)-(c). These show a morphology consistent with the "clumpiness" described by Shahar in Reference [55] as a consistent feature of e-gun deposited thin films, regardless of thickness. The limited AFM data on surface morphology available in the literature display similar structures [61, 63].

Two methods were used to analyze the structures in these images. The first was computation of the height-height auto-correlation function (HHCF) from the images. This provides a comparison of height $z(\overrightarrow{r})$ at $\overrightarrow{r} = (x, y)$, with the heights at the set

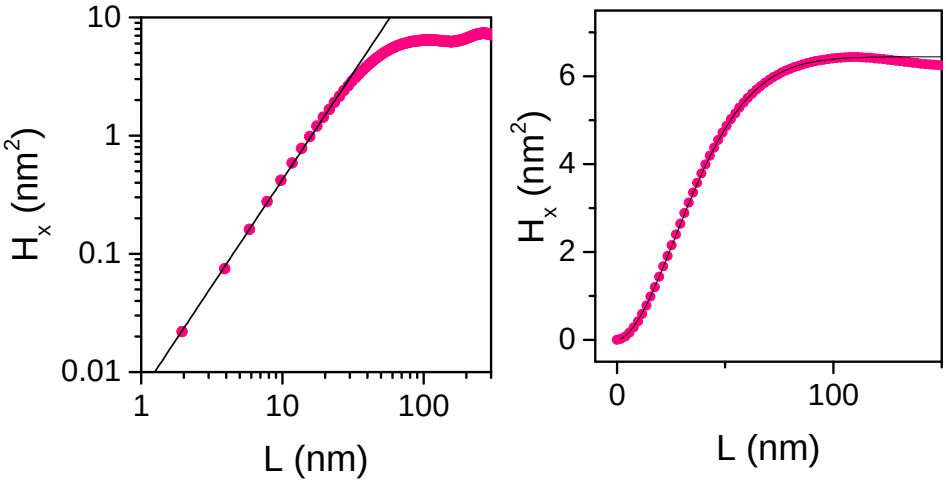

(a) Linear fit for the Hurst parameter.

(b) Gaussian fit.

Figure 4.23: Height-height correlation function as applied to the AFM data in Figure 4.22(a).

of points some distance L, by way of the relationship

$$H(L) = \left\langle \left[z(\overrightarrow{r}) - z(\overrightarrow{r} + \overrightarrow{L}) \right]^2 \right\rangle . \tag{4.18}$$

For AFM, surface statistics can only be reliably obtained using data from the fast-scanning (x-) axis [119]. For an image that contains X by Y pixels, a discrete, directional version of Equation 4.18 can be written

$$H_x(L) = \frac{1}{Y(X-\ell)} \sum_{j=1}^{Y} \sum_{i=1}^{X-\ell} \left(z(i\Delta x, j\Delta y) - z((i+\ell)\Delta x, j\Delta y) \right)^2 \tag{4.19}$$

where Δx and Δy describe the dimensions of a single pixel and $\ell = L/\Delta x$. The result of this calculation frequently takes the form of a Gaussian, specifically,

$$H_x(L) = 2\sigma^2 \left[1 - \exp\left(-\frac{L}{\xi_m} \right)^{2\alpha} \right] \tag{4.20}$$

where σ is the root-mean-squared of the surface roughness, ξ_m is the coherence length of the undulations, and α is known as the Hurst parameter, which characterizes roughness

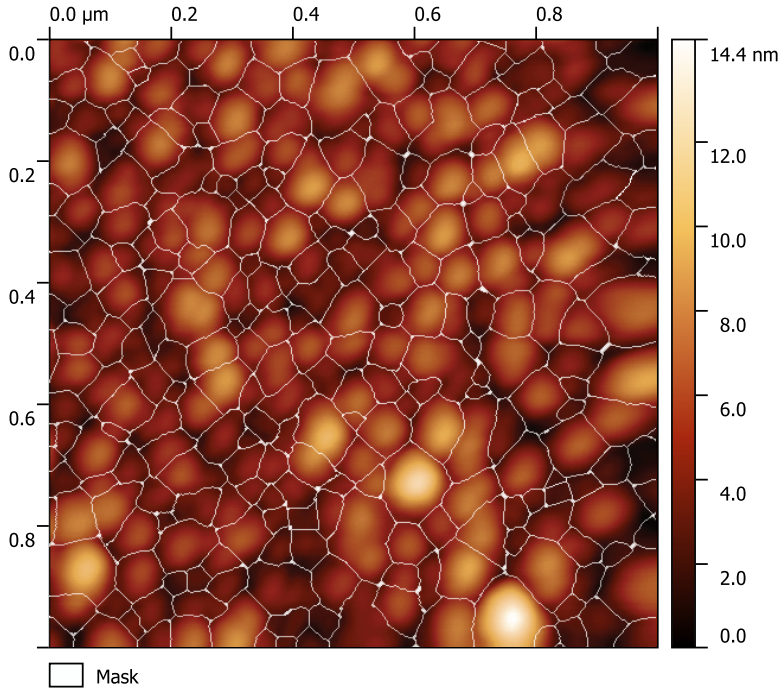

Figure 4.24: AFM data from Figure 4.22(a), superimposed with the boundaries used for grain analysis.

at very short lengthscales. In the regime where $L \ll \xi_m$, $H_x \propto L^{2\alpha}$, which proves very useful for fitting [120]. Figure 4.23 shows $H_x(L)$ calculated from the data in Figure 4.22(a) and fits that reveal α as well as σ and ξ_m. Data obtained from HHCF fits are presented in Figure 4.25.

The second analysis was performed by demarcating individual "grains" on each of the AFM micrographs, such as is shown in Figure 4.24. Demarcation was performed by hand. Statistics were assembled using on the maximum height within each grain and the areas of the grains. Grain diameters were calculated with the assumption of circular grains.

The results of both the HHCF fitting and grain analysis are presented together in Figure 4.25. Columns are labeled a-c, corresponding to the micrographs labeled in Figure 4.22, and "all". For HHCF quantities, this column averages the data in the other columns. For the grain analysis data, this column was computed from statistics on the complete set of grains from the three microgtraphs.

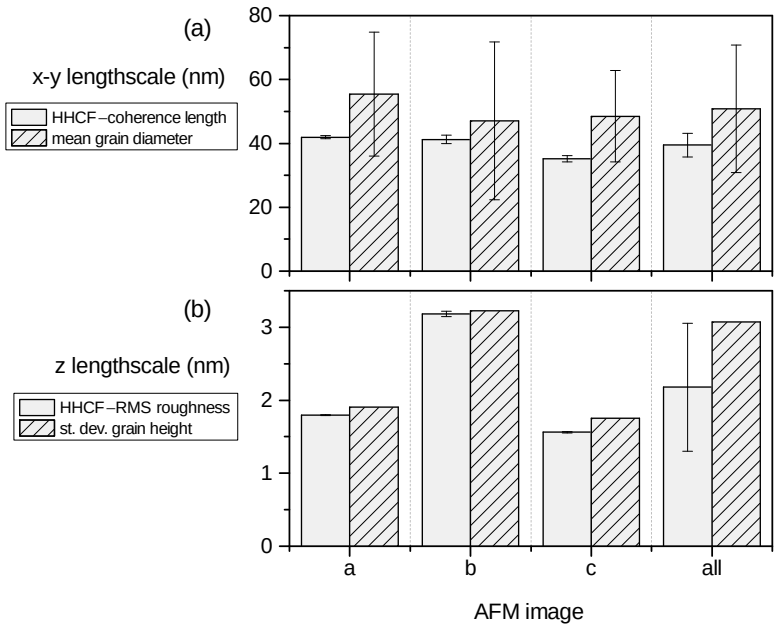

Figure 4.25: Statistics obtained from analysis of the AFM micrographs in Figure 4.22.

Figure 4.25(a) shows coherence length ξ_m determined from HHCF fits alongside the mean grain diameters. The uncertainty is the fitting error for the HHCF data (a-c), and standard deviation for the rest of the statistical data. These measurements of the in-plane dimension of surface features agree within uncertainty. HHCF measurements put the x-y lengthscale at an average 40 nm while the grain sizes measured on average 50 nm (with considerable spread around this value). In this case the discrepancy could result in part from approximating these irregular and angular-shapes as circles.

These two methods produced very similar measurements for the out-of-plane structures found in the indvidual images, as can be seen in Figure 4.25(b). Here, the standard deviation of the maximum heights within each grain was a more useful measure than the grain heights themselves. These measures of surface roughness differ between the micrographs, ranging from $\sim$ 2 to 3 nm. Surface roughness/variation in grain heights tracks with variation in grain diameter. (Indeed, for individual grain analysis, there was correlation between grain height and diameter.) The largest roughness value and spread were found in Figure 4.22(b), where some larger, taller structures are visible.

These analysis show that the average lengthscale of surface structures is between 40

and 50 nm, and that the variation of these features, both in height and breadth, differs in different regions of the sample. These variations in surface morphology from place to place provide a clue as to the large-scale inhomogeneity observed in this sample, but hardly the whole story. It is not clear what these structures, which to AFM tip resolution only reside in the top several nanometers of the film, can say about a 55 nm-thick film.

4.5 Sample dimensionality

The physics underlying behaviors observed in the data presented here depend on the sample dimensionality, which in turn depends on the superconducting coherence length ξ as well as the magnetic penetration depth for thin films, $\lambda_\perp$.

It is possible to extract ξ from magnetoresistance data by examining the temperature dependence of B_{c2}, the upper critical field at which the Cooper pairs in the superconducting condensate are broken apart to become normal. This occurs where the flux density everywhere is that which occurs within the vortex cores at lower fields, relating B_{c2} and ξ by

$$B_{c2} = \frac{\Phi_0}{2\pi\xi^2} \tag{4.21}$$

where Φ_0 is the flux quantum described in Section 2.1.1.

In the Ginzburg-Landau theory, ξ has temperature dependence

$$\xi(T) = \xi(0)\left(1 - \frac{T}{T_c}\right)^{-1/2}. \tag{4.22}$$

Combining this into Equation 4.21 gives

$$B_{c2}(T) = \frac{\Phi_0}{2\pi\xi^2(0)}\left(1 - \frac{T}{T_c}\right), \tag{4.23}$$

where T_c is the critical temperature in zero field. B_{c2} is expected to be linear in T, at least in the vicinity of T_c where G-L theory applies. The slope of this line,

$$\frac{dB_{c2}}{dT} = \frac{-\Phi_0}{2\pi\xi^2(0)T_c}, \tag{4.24}$$

can be used to find $\xi(0)$.

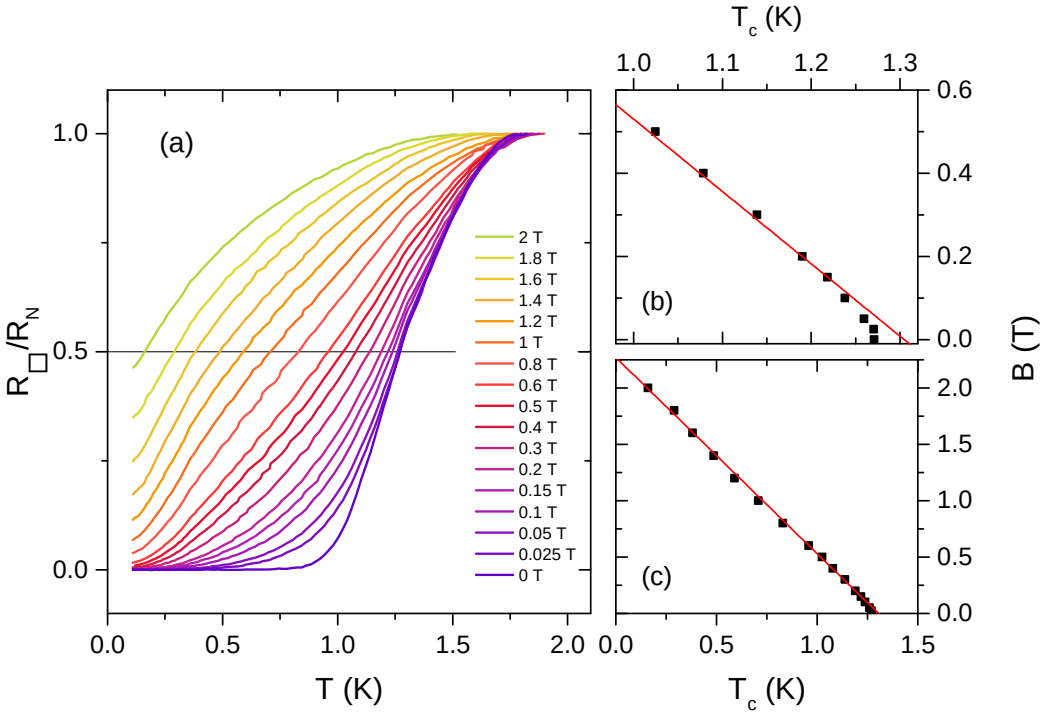

Figure 4.26: (a) Normalized resistance vs temperature data used to determine $T_c(B)$ shown in (b) for the low-field region and (c) for the full temperature range. Red lines show fits to these data.

For sample A, the set of points $T_c(B)$ will be used in place of $B_{c2}(T)$, because the latter lacks clear definition in the presence of the MR peak. T_c here is taken as the temperature where $R = 50\%R_N$, where R_N is the resistance maximum that occurs at temperatures just above the superconducting transition. Figure 4.26 (a) shows R vs T curves for this sample which have been normalized by the maximum value, and the line cut across to determine $T_c(B)$.

Figure 4.26 (b) shows these points in the immediate vicinity $T_c(0) = 1.27\,\mathrm{K}$, where a clear linear region is lacking. Instead, the data show linearity *below* 1.22 K, and bend down abruptly near the transition. In panel (a) of the figure, the R vs T data at the lowest fields lie on top of one another at all but the lowest resistances. Very similar results were reported by Steiner and Kapitulnik, who propose the possible explanation that the magnetic field response is cut off by some competing lengthscale at these very low fields [59]. They also suggest that the zero-field intercept of the fit to the

linear regime returns T_{c0}, the true mean-field transition temperature in the absence of fluctuations. By this measure, $T_{c0} = 1.30\,\mathrm{K}$ for Sample A.

Figure 4.26 (c) shows the other unexpected result of this analysis, which is that the same linear dependence seen between 1 K and 1.22 K describes the data down to the lowest temperatures. The upper critical field of a type II BCS superconductor, such as this one, is predicted to have negative curvature as a function of temperature [32, 121]. However, there have been previous reports of linearity in $B_{c2}(T)$ as $T \to 0$ in disordered films [32,38,122]. A likely explanation based is offered in Reference [121], which predicts an enhancement in B_{c2} to arise from strong mesoscopic disorder and the formation of superconducting islands. Among these islands there will be some with very strong local pairing, where the local pair-breaking field exceeds the mean-field value, and Josephson coupling between these islands can maintain phase order above the mean-field B_{c2}. The greatest enhancements will occur at the lowest temperatures, where phase fluctuations are suppressed.

These explanations of the form of the data in Figures 4.26 (b) and (c) do not provide much guidance for the practical matter of determining dB_{c2}/dT near T_c in order to determine ξ. The red fitline that describes the linear behavior below 1.22 K can be used with Equation 4.24 to obtain $\xi(0) = 12\,\mathrm{nm}$. Despite the good agreement of this fit with the data shown, it does not inspire confidence to note that these low-temperature data also point to a zero-temperature depairing field near 2.2 T, though other aspects of the data clearly indicate pairing, if not long-range phase order, occurs at and above this field. While it seems that the data very close to T_c, where the slope magnitude is larger, would offer a larger value for B_{c2} and a smaller value for ξ, it is likely that other physics plays a role in this regime. The apparent behavior of the data is an infinite slope in the limit of $T \to T_c$, which may relate to fluctuations that suppress T_c at zero field.

Equation 4.22 provides values for the coherence length at finite temperatures, based on the zero temperature measurement. Only in the immediate vicinity of T_c does $\xi(T) \gtrsim d$, the film thickness, which is considered the cutoff for the quasi-2D regime. The results reported in this chapter are all outside this 60 mK window, in a region where the film is effectively 3D by this criterion. It has been suggested that a second lengthscale, the dephasing length L_φ, may be important for determining the effective dimensionality of a system in the vicinity of a quantum critical point [14]. This has been used to argue

that the quasi-2D regime applies to InO_x films with thicknesses similar to this one [108]. So it is possible that this film is on the very margin of 2D superconductivity.

The penetration depth λ for Sample A was determined using Equation 2.4 and the assumption that pair density $n_s = n/2$. With normal state carrier concentration determined to be $n = 2.7 \times 10^{20}\,\mathrm{cm}^{-3}$ by Hall measurements, London penetration depth $\lambda_L = 460\,\mathrm{nm}$. In the vicinity of T_c, this value is modified according to the temperature dependence shown in Equation 2.7.

However, this value does not account for disorder, which is important. Given the atomic-length disorder of InO_x, it is likely the mean free path ℓ is similarly short. Equation 2.7, which relates the phenomenological G-L coherence length $\xi(0)$ to the BCS value ξ_0 can be manipulated to show $\xi(0)^2/\ell \approx \xi_0$. This means the dirty limit $\ell \ll \xi_0$ can be written $\ell^2 \ll \xi(0)^2$, which is clearly the case for Sample A. This means the corrections to λ given in Equation 2.5 will apply. Using the arguments above, $\lambda_{eff} \approx \lambda_L \xi(0)/\ell$, and we expect $\xi(0)/\ell$ to be large.

Unfortunately, ℓ was not measured, so the value of the correction term is not known. We can only conclude that the value $\lambda_L = 460\,\mathrm{nm}$ is low. Equation 2.20 gives the more relevant penetration depth $\lambda_\perp = 3.9\,\mu\mathrm{m}$ for a 55 nm film in a perpendicular field. This measurement is also probably low.

These values for the penetration depth clearly indicate that $d \ll \lambda \ll \lambda_\perp$, so the film will have the thin-film magnetic properties described in Section 2.1.2, including very long-range interactions between vortices.

Chapter 5

Discussion and conclusion

5.1 Vortex variable range hopping in context

The central finding of this work is strong evidence of vortex motion by variable-range hopping in two disordered superconducting films, which was presented in the last chapter. Through this finding we gain a fuller understanding of the range of behaviors exhibited by vortices in disordered superconducting films.

However, tunneling of vortices is hardly a new concept. Phase slips due to quantum fluctuations in low-dimensional systems have been under consideration since the early 80's. [86, 88] Not long after came evidence for vortex tunneling in bulk material [92] and films [93]. There has been detection and exploration of quantum phase slips in superconducting nanowires [123, 124]. The intermediate metallic regime observed in thin films, [23–26] which has eluded clear explanation for the last twenty years, has been approached as a problem of phase fluctuation and localization in the purely quantum $T \to 0$ limit [78, 79]. At this point, it clearly has been demonstrated that vortices can behave as quantum objects.

Most work on vortex VRH has been theoretical. This has no doubt been spurred, at least in part, by a desire to understand all manner of vortex motion in the disordered, 2D layers of high-T_c superconductors.

In 1991, Fisher, Tokuyasu and Young (FTY) made a prediction for variable range hopping of vortices in thin films. [95] They reasoned that the long-range interactions between the vortices in a thin film, described by Equation 2.22, would mean that the

movement of one vortex would involve a reshuffling of numerous nearby vortices. (This is the idea behind collective pinning theory, as well.) They argued that the collective hopping behavior, when optimized in the fashion described in Section 2.3, would lead to a hopping exponent $2/3 \leq p \leq 4/5$, in Equation 4.2. A similar result was obtained by Nelson and Vinokur for vortex VRH high-T_c films with columnar defects, though here it was in very weak fields and dilute vortices [125].

The temperature dependence predicted above for correlated vortex hopping has been observed in $YBa_2Cu_3O_{7-\delta}$ (YBCO) [97,98,126,127]. This same mechanism was explored as an explanation for a hopping exponent around 0.75 found for charge hopping in very thin films of quenched-condensed metals [48].

Auerbach, Arovas and Ghosh (AAG) approached the problem of single-vortex hopping by computing wavefunction overlap between two pinning sites [96]. They found a form for variable-range hopping with a hopping exponent $p = 1/3$, the same dependence Mott found for for 2D VRH hopping of non-interacting electrons. They predicted a field-independent value for characteristic temperature

$$T_0 = K\delta\bar{V}\left(\frac{\pi n_s}{n_{pin}}\right)^2, \tag{5.1}$$

where K is a numerical factor, $\delta\bar{V}$ is the spread in pinning site energies, and n_s/n_{pin} is the ratio of densities of Cooper pairs to pinning sites. This result applies in the limit of low fields, where the inter-vortex spacing $1/\sqrt{n_v}$ is much larger than the distance between pinning sites $1/\sqrt{n_{pin}}$. In addition, they calculated an exponential suppression to tunneling that depends on Fermi wavevector k_F and thus on carrier concentration n. The authors offer this as a possible explanation for why vortex VRH has not appeared in the literature: high carrier concentration superconductors like metals have virtually zero tunneling probability for vortices. They predict tunneling to occur at observable rates in low-n superconductors such as InO_x or YBCO.

Prior to the publication of the Sample A data in Reference [128], there were some very limited reports of vortex hopping with $p = 1/3$. Koren et al. designed an experiment to test the AAG theory, fabricating a long, thin (1 m long by 14 μm wide) $YBa_2Cu_3O_{7-\delta}$ meander line [99]. The geometry was designed to invite phase slips across or within the superconducting film, resulting in a measureable resistance. They were indeed able to

find a regime of 2D Mott-VRH of vortices at high fields and low temperatures, spanning a narrow range of resistances. They found T_0 to be weakly temperature dependent, but consistent with the scale predicted by AAG. Breznay et al. also use $p = 1/3$ to describe transport data across the SIT in a duality-symmetric InO_x sample, [129] very similar to the way Sample A data were treated in Section 4.2. In this case, however, the use of $p = 1/3$ is presented as an "ansatz", starting with the expectation of VRH on the insulating side of the transition and then extending it this across the SIT to the putative superconducting side, and the fits to the form are in no way rigorous.

Thus, the 2D Mott hopping form for vortices observed to span several orders of magnitude in the data for Sample A provides an unprecedented level of support for this mechanism's very existence. Sample B does not show such robust evidence for hopping with $p = 1/3$ over the full field range, as the Zabrodskii plot of these data show field dependence of p. However, the data provide evidence for vortex motion with a hopping process with $p \lesssim 1/2$, and thus different from classical nearest neighbor hopping or the correlated hopping predicted by FTY. The characteristics of Sample B data may come from an interplay between the true exponential hopping dependence and a temperature-dependent prefactor $R_0(T)$. This prefactor is predicted to have the form

$$R_0(T) = AT^m, \tag{5.2}$$

where A and m are constant. Throughout this analysis it has been assumed that m is negligibly small so that $R_0 \approx A$, because it is difficult to untangle power law and exponential behavior, especially in data that spans less than a decade in resistance.

The theory developed by AAG predicts the hopping exponent exhibited by vortices in these data, and thus it is the best explanation available for the data presented in this dissertation. Their theory is supported by the fact that all evidence of vortex hopping with exponent $p = 1/3$ presented up to now, and within this thesis so far, comes from low-n materials.

However, there are two key features of the data presented here that do not agree with the AAG prediction. The first is a field-dependent characteristic temperature T_0, which will be discussed in the next section. The second is the persistence of Mott law hopping with $p = 1/3$ up to fields where vortex population is dense and, by the interaction form

in Equation 2.22, should be highly interacting. The AAG theory should not apply in this regime, because it does not consider these interactions, which are expected to give rise to a higher value of p. No such crossover is observed.

This apparent lack of interaction is also seen in the duality-symmetry across the SIT. The continuous power law magnetoresistance shown in Figure 4.16 holds from far below B_c through the transition, (though the agreement is not equally good at all temperatures.) As discussed in Section 2.2.1, the duality between Cooper pairs and vortices is not perfect, in part because of the different interaction potentials between vortices and charges.

Recent work of Mulligan and Raghu on the field-tuned SIT provides a possible solution for this problem, as well as the persistance of the hopping form for non-interacting vortices up to high fields. The aim of this work was to provide a theory for perfect self-duality at the direct SIT, as well as an explanation for a broader intermediate metallic state. They offer as a possible solution the replacement of the bosonic degrees of freedom with composite particles–each corresponding to a Cooper pair bound with a vortex–which collectively behave like a non-Fermi liquid metal [83,130]. This treatment is based on theories of quantum effects in two-dimensional electron gasses, which are considered to be analagous quantum systems to quasi-2D superconductors [129]. The interactions in this composite system may be substantially suppressed, and explain the form of hopping found here [128].

5.2 A granular model for characteristic hopping energy T_0

All samples showing VRH presented here have a characteristic energy T_0 that is highly dependent on applied field, and thus out of agreement with the prediction of AAG. An alternative theory of T_0 was presented in Reference [128], which explains the dependence of $T_0(B) \propto 1/B$ at low fields, shown in Figure 5.1.

The picture of disorder-induced superconducting islands within the amorphous material due to mesoscale inhomogeneity explains both the MR peak and field-dependence of B_{c2} observed in this sample. This picture also offers a way to understand the field dependence of T_0. We can consider the film as a layer of superconducting islands in a normal/insulating background. Specifically, these islands are modeled as close-packed

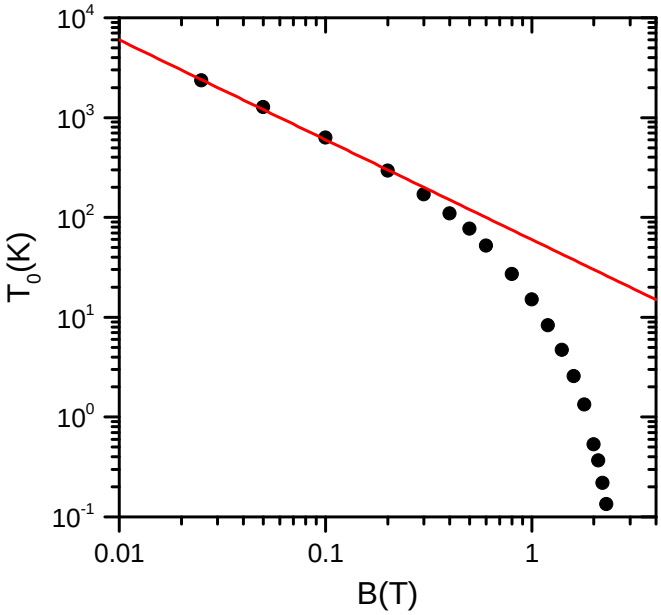

Figure 5.1: Characteristic temperature T_0 for 2D Mott hopping as a function of magnetic field for Sample A, with a line showing $T_0 = [60\,\mathrm{K}\cdot\mathrm{T}]/B$.

spheres, coupled through the weak links where they touch to form a Josephson junction array (JJA). Vortices are pinned in the normal regions between the spherical islands, and since the energy barrier for tunneling is much smaller across the weak links than through the grains themselves, hopping occurs across these links. This gives rise to a localization length a that is approximately equal to film thickness d.

Vortex pinning energies ε in the spaces between grains follow the form given in Equation 2.21 for thin films, or its JJA equivalent in Equation 2.31. Assuming $\lambda_\perp = \lambda_{JJ}$, this can be expressed generically as

$$\varepsilon = \varepsilon_{00} \ln\left(\frac{\lambda_\perp}{a}\right). \tag{5.3}$$

The energy ε_{00} can be expressed in terms of either the thin film or JJA picture, such that

$$\varepsilon_{00} = \left(\frac{\Phi_0}{4\pi}\right)^2 \lambda_\perp^{-1} = \pi E_J, \tag{5.4}$$

where $E_J = I_c\Phi_0/2\pi c$. In Reference [128], the authors interpret ε_{00} as the energy of the supercurrents through the central plaquette surrounding a vortex. The remaining energy in Equation 5.3, $\varepsilon_{00}[1 - \ln(\lambda_\perp/a)]$, is contributed by currents further distances from the vortex core.

The average energy for a pinning site is $\bar{\varepsilon}$. Due to disorder, site energies are distributed over a band $\bar{\varepsilon} \pm \delta\varepsilon$. We can consider this disorder to originate from variation in grain sizes, which in turn leads to a spread in the coupling energies between adjacent grains. These deviations have greatest effect where the currents are strongest and the paths through the islands are shortest, as current paths through numerous junctions will average out disorder. Thus, the specific properties of the central plaquette will define the energy spread, so that $\delta\varepsilon = \delta\varepsilon_{00} = \pi\delta E_J$. The spread in pinning energies depends on the spread in Josephson coupling energies E_J.

These quantities determine the hopping characteristics between these pinning sites. Based on Equation 2.41, the characteristic temperature for 2D Mott hopping is given by the relation [45]

$$T_0 = \frac{\beta}{k_B g(\mu) a^2}. \tag{5.5}$$

At low fields, only a fraction of the sites are occupied. We can model the density of states in this region as a low-energy exponential tail $g(\varepsilon) = g_0 \exp(-(\varepsilon - \bar{\varepsilon})/\delta\varepsilon$. The effective Fermi level μ will depend on the vortex number density

$$n_v = \frac{B}{\Phi_0} = \int_{-\infty}^{\mu} g(\varepsilon) d\varepsilon = g(\mu)\delta\varepsilon. \tag{5.6}$$

This can be combined with Equation 5.5 to give

$$T_0 = \frac{\beta\Phi_0\,\delta\varepsilon}{k_B a^2}\,\frac{1}{B}, \tag{5.7}$$

the $T_0 \propto 1/B$ dependence seen in Figure 5.1.

The system-specific quantities in coeffient C, where $T_0 = C/B$, are the energy distribution $\delta\varepsilon$ and localization length a. As discussed above, $\delta\varepsilon$ depends on δE_J. For very strong disorder, $\delta E_J/E_J \sim 1$, so $\delta\varepsilon$ can be replaced with $\varepsilon_{00} = (\Phi_0/4\pi)^2\lambda_\perp^{-1}$. The spherical grain model implies $a = d$. Thus, the coefficient can be written, this time in

terms of bulk penetration depth λ,

$$C = \frac{\beta}{16\pi^2}\frac{\Phi_0^3}{k_B}\frac{1}{d\lambda^2}. \tag{5.8}$$

If $d = 55\,\text{nm}$ and $\lambda = 13\,\mu\text{m}$, this gives $C = 60\,\text{K}\cdot\text{T}$, the value found to fit the data in Figure 5.1. This value of bulk penetration depth λ is larger than the measured value for λ_L discussed Section 4.5 by a factor of 30. However, it was also discussed that the effective penetration depth $\lambda_{eff} > \lambda_L$. It is possible that the correction for disorder would be enough to overcome this discrepancy.

It should be noted that the treatment of the film as a layer of spheres was inspired by the good match between the average lengthscale of the film's surface morphology and the overall film thickness. However, the height data do not indicate that the film has a true granular morphology. Despite the suggestive texture that appears in the AFM images, the RMS surface roughness across the micrographs measured only 2-3 nm. This is a much smaller fraction of overall film thickness than would be expected if the film were literally comprised of spherical grains. Furthermore, the grain heights were found to vary with a standard deviation of only 3 nm, which is much smaller than the variation in the in-plane footprints. Thus, there is little to indicate that the surface morphology is linked to the compositional disorder that gives rise to effective granularity, save the relative success of this model.

The exponential prefactor R_0 in Sample A decreases with increasing field, with $R \to R_Q$ as $B \to B_c$. Sample B does this as well. The physics behind this behavior is unknown, as the pre-exponential factor is not expected to be highly field-dependent [45].

5.3 Undiscovered hopping behavior and future work

It is surprising that after decades of study of thin film superconductors and the SIT, vortex VRH is only being reported and strongly substantiated now. As discussed in Section 5.1, such rarity might be the result of a set of restrictions on sample parameters, such as an upper bound on n, that permit vortex VRH to occur in fraction of superconducting systems. Even so, there has been significant data collected on disordered superconductors over the decades–large enough that it is likely to contain additional

evidence of VRH. Thus, it is more likely that the shortage of evidence stems from researchers' failure to check for the phenomenon. In Reference [74], Chernevak and Valles show data for quench-deposited bismuth films grown on a thin antimony underlayer. Some of these films show the expected thermally activated flux flow (TAFF) temperature dependence, and others do not. In general, films that show TAFF have higher transition temperatures than those that do not show this behavior. The authors attribute this poor fit to the activated form, due to an upward curvature of the data, as evidence of an intermediate metallic state.

Presented in Figure 5.2 are results of a re-analysis of these same data, which were digitized from Figure 1 (b) in Reference [74]. In Figure 5.2 (a) the resistance has been plotted on a log scale against $T^{-1/3}$, linearizing much of the data, with some curves over almost three orders of magnitude in resistance. Prefactor R_0 and characteristic temperature T_0 from the 2D Mott hopping form Equation 4.8 are plotted in Figure 5.2 (b) and (c), and take similar forms to the field-dependence of fitting parameters observed for Samples A and B in this dissertation. These fits and similarities suggest the presence of a VRH regime in these Bi/Sb films as an alternate interpretation of these data that do not necessarily disagree with the original conclusion of the presence of an intermediate metallic regime. The departure of these data from linearity at the lowest temperatures could signal the onset of a transition to a temperature-independent resistance regime.

This observation is interesting as it indicates a departure from the AAG prediction. Amorphous Bi is not considered to be a low-n superconductor. While Bi is a semi-metal with a very low carrier concentration ($\sim 10^{17}\,\mathrm{cm}^{-3}$) in its crystalline form[1], carrier concentrations of $n \sim 10^{22} - 10^{23}\,\mathrm{cm}^{-3}$ have been obtained via Hall measurements of the amorphous form of Bi [132, 133]. This form of the material is grown by depositing onto substrates held at liquid helium temperatures, usually on a thin Sb wetting layer. Between 10 and 20 K the material crystallizes, which coincides with a dramatic drop in the carrier concentration [132].

The data shown in Figure 5.2 provide the strongest example of vortex VRH behavior found thus far, in that it shows good agreement over multiple decades. Much of the success of this re-analysis depends on the details of the original plot in Reference [74],

[1]The magnetic signature of superconductivity was reportedly detected for the first time in crystalline Bi. This was observed near 0.53 mK [131].

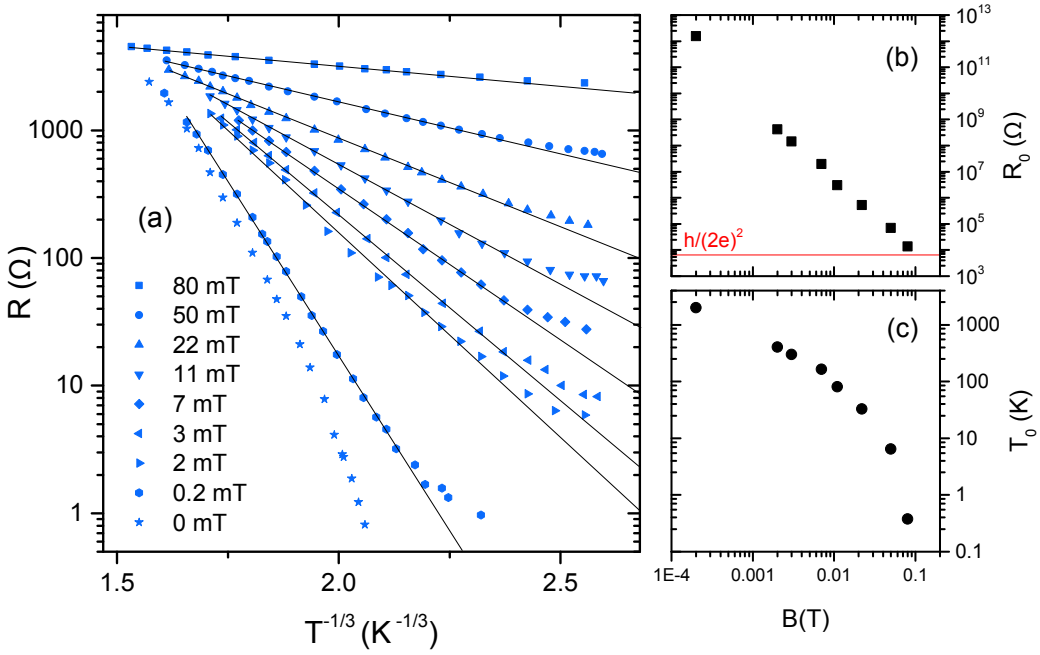

Figure 5.2: (a) $\log R$ versus $T^{-1/3}$ for Bi/Sb films from Reference [74] along with fit lines to the 2D Mott hopping form Equation 4.8. Parameters (b) R_0 and (c) T_0 as a function of B, extracted from the fits shown in (a).

which allowed capture of the data on a logarithmic scale in R. Many plots in the SIT literature share characteristics with those presented here, but are rendered on a linear scale in R, which limits the effectiveness of the re-analysis shown here. More work would have to be done to identify additional examples of this behavior in historical data sets and access the source data. More relevant data sets–new or historical–will need to be identified and explored if the specific parameters necessary for the observation of VRH are to be understood.

References

[1] M. N. Wilson. A century of superconducting technology. In *AIP Conference Proceedings*, volume 1435, pages 11–35. American Institute of Physics, June 2012.

[2] Heike Kamerlingh Onnes. Investigations into the properties of substances at low temperatures, which have led, amongst other things, to the preparation of liquid helium. *Nobel Lecture*, pages 306–336, 1913.

[3] J. Bardeen, L. N. Cooper, and J. R. Schrieffer. Theory of superconductivity. *Physical Review*, 108(5):1175–1204, December 1957.

[4] V. L. Ginzburg and L. D. Landau. On the Theory of superconductivity. *Zh. Eksp. Teor. Fiz.*, 20:1064–1082, 1950.

[5] Lev Gor'kov. Microscopic derivation of the Ginzburg-Landau equations in the theory of superconductivity. *Soviet Physics JETP*, 9(6):1364, December 1959.

[6] Michael Tinkham. *Introduction to Superconductivity.* McGraw-Hill, New York, 2nd ed. edition, 1996.

[7] F. London and H. London. The electromagnetic equations of the supraconductor. *Proceedings of the Royal Society A: Mathematical, Physical and Engineering Sciences*, 149(866):71–88, March 1935.

[8] Alexei Alexeyevich Abrikosov. On the magnetic properties of superconductors of the second group. *Soviet physics JETP*, 5(6):1174–1182, December 1957.

[9] Kristin Coyne. New world-record magnet fulfills superconducting promise - maglab. *National High Magnetic Field Laboratory News*, December 2017.

[10] Gianni Blatter, Mikhail V. Feigel'man, Vadim B. Geshkenbein, Anatoly I. Larkin, and Valerii M. Vinokur. Vortices in high-temperature superconductors. *Reviews of Modern Physics*, 66(4):1125–1388, October 1994.

[11] J. Pearl. Current distribution in superconducting films carrying quantized fluxoids. *Applied Physics Letters*, 5(4):65–66, August 1964.

[12] A. Chulliat, S. Macmillan, P. Alken, C. Beggan, M. Nair, B. Hamilton, A. Woods, V. Ridley, S. Maus, and A. Thomson. The US/UK world magnetic model for 2015-2020. Technical report, 2015.

[13] P. G. de Gennes. *Superconductivity of Metals and Alloys*. Addison-Wesley, Redwood City, California, 2nd edition, 1989.

[14] S. L. Sondhi, S. M. Girvin, J. P. Carini, and Dan Shahar. Continuous quantum phase transitions. *Reviews of Modern Physics*, 69(1):315–333, January 1997.

[15] Brian D. Josephson. Possible new effects in superconductive tunnelling. *Physics Letters*, 1(7):251–253, July 1962.

[16] Bertrand I. Halperin, Gil Refael, and Eugene Demler. Resistance in superconductors. *International Journal of Modern Physics B*, 24(20n21):4039–4080, August 2010.

[17] Ibrahim Elsayed, K. H. Sarwa B. Tan, Kevin A. Parendo, and Allen M. Goldman. Zero resistance at integer values of frustration in out-of-equilibrium classical josephson-junction arrays. *Physical Review B - Condensed Matter and Materials Physics*, 80(5):052502, August 2009.

[18] M. S. Rzchowski, S. P. Benz, M. Tinkham, and C. J. Lobb. Vortex pinning in Josephson-junction arrays. *Physical Review B*, 42(4):2041–2050, August 1990.

[19] H. S. J. van der Zant, F. C. Fritschy, T. P. Orlando, and J. E. Mooij. Dynamics of vortices in underdamped josephson-junction arrays. *Physical Review Letters*, 66(19):2531–2534, May 1991.

[20] E. Abrahams, P. W. Anderson, D. C. Licciardello, and T. V. Ramakrishnan. Scaling theory of localization: Absence of quantum diffusion in two dimensions. *Physical Review Letters*, 42(10):673–676, March 1979.

[21] Allen M. Goldman. Superconductor-insulator transitions. *International Journal of Modern Physics B*, 24(21):4081–4101, August 2010.

[22] Yu Saito, Tsutomu Nojima, and Yoshihiro Iwasa. Highly crystalline 2d superconductors. *Nature Reviews Materials*, 2(1):16094, December 2016.

[23] D. Ephron, Ali Yazdani, Aharon Kapitulnik, and M. R. Beasley. Observation of quantum dissipation in the vortex state of a highly disordered superconducting thin film. *Physical Review Letters*, 76(9):1529–1532, February 1996.

[24] Nadya Mason and Aharon Kapitulnik. Dissipation effects on the superconductor-insulator transition in 2D superconductors. *Physical Review Letters*, 82(26):5341–5344, June 1999.

[25] Nadya Mason and Aharon Kapitulnik. True superconductivity in a two-dimensional superconducting-insulating system. *Physical Review B - Condensed Matter and Materials Physics*, 64(6):605041–605044, July 2001.

[26] M. Morita and S. Okuma. Magnetoresistance and vortex states below the 2D superconductor-insulator transition near T=0. *Physica C: Superconductivity*, 392-396(PART 1):406–409, October 2003.

[27] Yongguang Qin, Carlos L. Vicente, and Jongsoo Yoon. Magnetically induced metallic phase in superconducting tantalum films. *Physical Review B - Condensed Matter and Materials Physics*, 73(10):100505, March 2006.

[28] A. W. Tsen, B. Hunt, Y. D. Kim, Z. J. Yuan, S. Jia, R. J. Cava, J. Hone, P. Kim, C. R. Dean, and A. N. Pasupathy. Nature of the quantum metal in a two-dimensional crystalline superconductor. *Nature Physics*, 12(3):208–212, December 2016.

[29] Yu Saito, Tsutomu Nojima, and Yoshihiro Iwasa. Quantum phase transitions in highly crystalline two-dimensional superconductors. *Nature Communications*, 9(1):778, December 2018.

[30] I. Tamir, A. Benyamini, E. J. Telford, F. Gorniaczyk, A. Doron, T. Levinson, D. Wang, F. Gay, B. Sacépé, J. Hone, K. Watanabe, T. Taniguchi, C. R. Dean, A. N. Pasupathy, and Dan Shahar. Extreme sensitivity of the superconducting state in thin films. *ArXiv e-prints*, page 1804.04648, April 2018.

[31] Aharon Kapitulnik, Steven A. Kivelson, and Boris Spivak. Anomalous metals – failed superconductors. *ArXiv e-prints*, December 2017.

[32] A. F. Hebard and M. A. Paalanen. Pair-breaking model for disorder in two-dimensional superconductors. *Physical Review B*, 30(7):4063–4066, October 1984.

[33] H. M. Jaeger, D. B. Haviland, A. M. Goldman, and B. G. Orr. Threshold for superconductivity in ultrathin amorphous gallium films. *Physical Review B*, 34(7):4920–4923, October 1986.

[34] David B. Haviland, Ying Liu, and Allen M. Goldman. Onset of superconductivity in the two-dimensional limit. *Physical Review Letters*, 62(18):2180–2183, May 1989.

[35] Matthew P. A. Fisher. Quantum phase transitions in disordered two-dimensional superconductors. *Physical Review Letters*, 65(7):923–926, August 1990.

[36] Myles A. Steiner, Nicholas P. Breznay, and Aharon Kapitulnik. Approach to a superconductor-to-Bose-insulator transition in disordered films. *Physical Review B - Condensed Matter and Materials Physics*, 77(21):212501, June 2008.

[37] Tatyana I. Baturina and Valerii M. Vinokur. Superinsulator-superconductor duality in two dimensions. *Annals of Physics*, 331:236–257, April 2013.

[38] Benjamin Sacépé, Johanna Seidemann, Maoz Ovadia, Idan Tamir, Dan Shahar, Claude Chapelier, C. Strunk, and B. A. Piot. High-field termination of a Cooper-pair insulator. *Physical Review B - Condensed Matter and Materials Physics*, 91(22):1–5, June 2015.

[39] A. F. Hebard and M. A. Paalanen. Magnetic-field-tuned superconductor-insulator transition in two-dimensional films. *Physical Review Letters*, 65(7):927–930, August 1990.

[40] S. M. Girvin. Duality in perspective. *Science*, 274:524–525, October 1996.

[41] Matthew P. A. Fisher, G. Grinstein, and S. M. Girvin. Presence of quantum diffusion in two dimensions: Universal resistance at the superconductor-insulator transition. *Physical Review Letters*, 64(5):587–590, January 1990.

[42] Alexey Yu. Mironov, Daniel M. Silevitch, Thomas Proslier, Svetlana V. Postolova, Maria V. Burdastyh, Anton K. Gutakovskii, Thomas F. Rosenbaum, Valerii M. Vinokur, and Tatyana I. Baturina. Charge Berezinskii-Kosterlitz-Thouless transition in superconducting NbTiN films. *Scientific Reports*, 8(1):4082, December 2018.

[43] Yen-Hsiang Lin, JJ Nelson, and Allen M. Goldman. Superconductivity of very thin films: The superconductor-insulator transition. *Physica C: Superconductivity and its Applications*, 514:130–141, February 2015.

[44] N. F. Mott. Conduction in glasses containing transition metal ions. *Journal of Non-Crystalline Solids*, 1(1):1–17, December 1968.

[45] B. I. Shklovskii and A. L. Efros. *Electronic properties of doped semiconductors.* Springer-Verlag, Heidelberg, 1984.

[46] Vinay Ambegaokar, Bertrand I. Halperin, and James S. Langer. Hopping conductivity in disordered systems. *Physical Review B*, 4(8):2612–2620, October 1971.

[47] Boris I. Shklovskii. Variable range hopping in thin film with large dielectric constant. *Low Temperature Physics/Fizika Nizkikh Temperatur*, 43(6):879–883, 2017.

[48] N. Marković, C. Christiansen, D. E. Grupp, A. M. Mack, G. Martinez-Arizala, and A. M. Goldman. Anomalous hopping exponents of ultrathin metal films. *Physical Review B*, 62(3):2195–2200, July 2000.

[49] Z. Ovadyahu, B. Ovryn, and H. W. Kraner. Microstructure and electro-optical properties of evaporated indium-oxide films. *Journal of the Electrochemical Society*, 130(4):917–921, April 1983.

[50] Zvi Ovadyahu. Some finite temperature aspects of the Anderson transition. *Journal of Physics C*, 19:5187–5213, September 1986.

[51] U. Givan and Z. Ovadyahu. Compositional disorder and transport peculiarities in the amorphous indium oxides. *Physical Review B*, 86(16):165101, October 2012.

[52] Zvi Ovadyahu. Slow dynamics of electron glasses: The role of disorder. *Physical Review B*, 95(13):134203, April 2017.

[53] David Kowal and Zvi Ovadyahu. Scale dependent superconductor-insulator transition. *Physica C: Superconductivity*, 468(4):322–325, February 2008.

[54] N. W. Ashcroft and N. D. Mermin. *Solid state physics*. Science: Physics. Saunders College, 1976.

[55] Dan Shahar and Zvi Ovadyahu. Superconductivity near the mobility edge. *Physical Review B*, 46(17):10917–10922, November 1992.

[56] Zvi Ovadyahu. Optical absorption and disorder in an amorphous metal. *Physical Review B*, 47(10):6161–6164, March 1993.

[57] David Kowal and Zvi Ovadyahu. Disorder induced granularity in an amorphous superconductor. *Solid State Communications*, 90(12):783–786, June 1994.

[58] G. Sambandamurthy, L. W. Engel, A. Johansson, and Dan Shahar. Superconductivity-related insulating behavior. *Physical Review Letters*, 92(10):107005, March 2004.

[59] Myles A. Steiner and Aharon Kapitulnik. Superconductivity in the insulating phase above the field-tuned superconductor-insulator transition in disordered indium oxide films. *Physica C: Superconductivity*, 422(1-2):16–26, May 2005.

[60] G. Sambandamurthy, A. Johansson, E. Peled, D. Shahar, P. G. Björnsson, and K. A. Moler. Power law resistivity behavior in 2D superconductors across the magnetic field-tuned superconductor-insulator transition. *Europhysics Letters (EPL)*, 75(4):611–617, August 2006.

[61] K. H. Sarwa B. Tan, Kevin A. Parendo, and Allen M. Goldman. Evidence of spatially inhomogeneous pairing on the insulating side of a disorder-tuned superconductor-insulator transition. *Physical Review B - Condensed Matter and Materials Physics*, 78(1):014506, July 2008.

[62] Benjamin Sacépé, Thomas Dubouchet, Claude Chapelier, Marc Sanquer, Maoz Ovadia, Dan Shahar, Mikhail V. Feigel'man, and Lev B. Ioffe. Localization of preformed Cooper pairs in disordered superconductors. *Nature Physics*, 7(3):239–244, March 2011.

[63] Yeonbae Lee, Aviad Frydman, Tianran Chen, Brian Skinner, and Allen M. Goldman. Electrostatic tuning of the properties of disordered indium-oxide films near the superconductor-insulator transition. *Physical Review B*, 88(2):024509, July 2013.

[64] Maoz Ovadia, David Kalok, Benjamin Sacépé, and Dan Shahar. Duality symmetry and its breakdown in the vicinity of the superconductor-insulator transition. *Nature Physics*, 9(7):415–418, July 2013.

[65] Daniel Sherman, Boris Gorshunov, Shachaf Poran, Nandini Trivedi, Eli Farber, Martin Dressel, and Aviad Frydman. Effect of Coulomb interactions on the disorder-driven superconductor-insulator transition. *Physical Review B*, 89(3):035149, January 2014.

[66] Nicholas P. Breznay and Aharon Kapitulnik. Particle-hole symmetry reveals failed superconductivity in the metallic phase of two-dimensional superconducting films. *Science Advances*, 3(9):e1700612, September 2017.

[67] D. Sherman, G. Kopnov, D. Shahar, and A. Frydman. Measurement of a superconducting energy gap in a homogeneously amorphous insulator. *Phys. Rev. Lett.*, 108:177006, Apr 2012.

[68] A. F. Hebard and S. Nakahara. Structural phase transitions of indium/indium oxide thin-film composites. *Applied Physics Letters*, 41(12):1130–1132, December 1982.

[69] Leo J. van der Pauw. A method of measuring the resistivity and Hall coefficient on lamellae of arbitrary shape. *Philips Technical Review*, 20(8):220–224, 1958.

[70] Leo J. van der Pauw. A method of measuring specific resistivity and Hall effect of discs of arbitrary shape. *Philips Research Reports*, 13(1):1–9, February 1958.

[71] Guy K. White and Philip J. Meeson. *Experimental Techniques in Low-Temperature Physics*. Oxford University Press, Oxford, 4th edition, 2002.

[72] Quantum Design. *Physical Property Measurement System, Hardware Manual*. Quantum Design, San Diego, 5th edition, 2007.

[73] Kevin A. Parendo, K. H. Sarwa B. Tan, and Allen M. Goldman. Hot-electron effects in the two-dimensional superconductor-insulator transition. *Physical Review B - Condensed Matter and Materials Physics*, 74(13):134517, October 2006.

[74] J. A. Chervenak and J. M. Valles Jr. Absence of a zero-temperature vortex solid phase in strongly disordered superconducting Bi films. *Phys. Rev. B*, 61(14):R9245–R9248, April 2000.

[75] Yen-Hsiang Lin, JJ Nelson, and Allen M. Goldman. Suppression of the Berezinskii-Kosterlitz-Thouless transition in 2D superconductors by macroscopic quantum tunneling. *Physical Review Letters*, 109(1):2–5, July 2012.

[76] Wei Liu, Lidong Pan, Jiajia Wen, Minsoo Kim, G. Sambandamurthy, and N. P. Armitage. Microwave spectroscopy evidence of superconducting pairing in the magnetic-field-induced metallic state of InO_x films at zero temperature. *Physical Review Letters*, 111(6):1–5, August 2013.

[77] Yu Saito, Yuichi Kasahara, Jianting Ye, Yoshihiro Iwasa, and Tsutomu Nojima. Metallic ground state in an ion-gated two-dimensional superconductor. *Science*, 350(6259):409–413, October 2015.

[78] D. Das and S. Doniach. Existence of a Bose metal at T=0. *Physical Review B*, 60(2):16, July 1999.

[79] D. Das and S. Doniach. Bose metal: Gauge-field fluctuations and scaling for field-tuned quantum phase transitions. *Physical Review B*, 64(13):134511, September 2001.

[80] Philip W. Phillips and Denis Dalidovich. Electron-like quasiparticles drive the superconductor-insulator transition in homogeneously disordered thin films. *Philosophical Magazine B - Physics Of Condensed Matter Statistical Mechanics Electronic Optical And Magnetic Properties*, 81(9):847–854, September 2001.

[81] Philip W. Phillips and Denis Dalidovich. The elusive Bose metal. *Science*, 302(5643):243–247, October 2003.

[82] Victor M. Galitski, Gil Refael, Matthew P. A. Fisher, and T. Senthil. Vortices and quasiparticles near the superconductor-insulator transition in thin films. *Physical Review Letters*, 95(7):077002, August 2005.

[83] M. Mulligan and S. Raghu. Composite fermions and the field-tuned superconductor-insulator transition. *Physical Review B*, 93(20):205116, May 2016.

[84] L. Benfatto, C. Castellani, and T. Giamarchi. Broadening of the Berezinskii-Kosterlitz-Thouless superconducting transition by inhomogeneity and finite-size effects. *Physical Review B*, 80(21):214506, December 2009.

[85] P. W. Anderson and Y. B. Kim. Hard superconductivity: Theory of the motion of Abrikosov flux lines. *Reviews of Modern Physics*, 36(1):39–43, January 1964.

[86] Leonid I. Glazman and N. Ya. Fogel'. Possibility of quantum tunneling of vortices in thin superconducting films. *Soviet Journal of Low Temperature Physics*, 10:51, January 1984.

[87] Mikhail V. Feigel'man, Vadim B. Geshkenbein, and Anatoly I. Larkin. Pinning and creep in layered superconductors. *Physica C: Superconductivity and its Applications*, 167(1-2):177–187, April 1990.

[88] A. O. Caldeira and A. J. Leggett. Influence of dissipation on quantum tunneling in macroscopic systems. *Physical Review Letters*, 46(4):211–214, January 1981.

[89] L. B. Ioffe and B. N. Narozhny. Resistance of Josephson-junction arrays at low temperatures. *Physical Review B*, 58(17):11449–11457, November 1998.

[90] Michael J. Stephen. Quantum tunneling of vortex lines. *Physical Review Letters*, 72(10):1534–1536, March 1994.

[91] Ping Ao and David J. Thouless. Tunneling of a quantized vortex: Roles of pinning and dissipation. *Physical Review Letters*, 72(1):132–135, January 1994.

[92] A. V. Mitin. Temperature dependences of flux creep and critical current in molybdenum sulfides. *Soviet Physics JETP*, 66:335, August 1987.

[93] Ying Liu, David B. Haviland, Leonid I. Glazman, and Allen M. Goldman. Resistive transitions in ultrathin superconducting films: Possible evidence for quantum tunneling of vortices. *Physical Review Letters*, 68(14):2224–2227, April 1992.

[94] A. C. Mota, K. Aupke, A. Amann, T. Teruzzi, A. Pollini, and P. Visani. Quantum Tunneling of Vortices in Cuprate and Heavy-Fermion Superconductors. *Journal of Low Temperature Physics*, 95(1-2):377–381, April 1994.

[95] M. P. A. Fisher, T. A. Tokuyasu, and A. P. Young. Vortex variable-range-hopping resistivity in superconducting films. *Physical Review Letters*, 66(22):2931–2934, June 1991.

[96] Assa Auerbach, Daniel P. Arovas, and Sankalpa Ghosh. Quantum tunneling of vortices in two-dimensional condensates. *Physical Review B*, 74(6):064511, September 2006.

[97] C. Dekker, P. J. M. Wöltgens, R. H. Koch, B. W. Hussey, and A. Gupta. Absence of a finite-temperature vortex-glass phase transition in two-dimensional $YBa_2Cu_3O_{7-\delta}$ films. *Physical Review Letters*, 69(18):2717–2720, November 1992.

[98] Z. Sefrioui, D. Arias, F. Morales, M. Varela, C. Leon, R. Escudero, and J. Santamaría. Evidence for vortex tunnel dissipation in deoxygenated $YBa_2Cu_3O_{6.4}$ thin films. *Physical Review B*, 63(5):54509, January 2001.

[99] G. Koren, Y. Mor, Assa Auerbach, and E. Polturak. Quantum vortex tunneling in $YBa_2Cu_3O_{7-\delta}$ thin films. *Physical Review B*, 76(13):134516, October 2007.

[100] D. M. Finlayson, P. J. Mason, and I. F. Mohammad. Comment on variable-range hopping in InP close to the metal-insulator transition. *Journal of Physics C: Solid State Physics*, 20(25):L607–L610, September 1987.

[101] J. R. Taylor. *An Introduction to Error Analysis*. University Science Books, Sausalito, 1997.

[102] A. G. Zabrodskii and K. N. Zinov'eva. Low-temperature conductivity and metal-insulator transition in compensate n-Ge. *Soviet Physics JETP*, 59(2):425–433, February 1984.

[103] Ying Xing, H.-M. Zhang, Hai-Long Fu, Haiwen Liu, Yi Sun, J.-P. Peng, F. Wang, Xi Lin, X.-C. Ma, Q.-K. Xue, Jian Wang, and X. C. Xie. Quantum Griffiths singularity of superconductor-metal transition in Ga thin films. *Science*, 350(6260):542–545, October 2015.

[104] Shengchun Shen, Ying Xing, Pengjie Wang, Haiwen Liu, Hai-Long Fu, Yangwei Zhang, Lin He, X. C. Xie, Xi Lin, Jiacai Nie, and Jian Wang. Observation of quantum Griffiths singularity and ferromagnetism at the superconducting $LaAlO_3$ / $SrTiO_3$ (110) interface. *Physical Review B*, 94(14):144517, October 2016.

[105] Thomas Vojta. Rare region effects at classical, quantum and nonequilibrium phase transitions. *Journal of Physics A: Mathematical and General*, 39(22):R143, June 2006.

[106] I. Tamir, A. Doron, T. Levinson, F. Gorniaczyk, G. C. Tewari, and D. Shahar. Nonequilibrium restoration of duality symmetry in the vicinity of the superconductor-to-insulator transition. *Physical Review B*, 96(10):104513, September 2017.

[107] M. A. Paalanen, A. F. Hebard, and R. R. Ruel. Low-temperature insulating phases of uniformly disordered two-dimensional superconductors. *Physical Review Letters*, 69(10):1604–1607, September 1992.

[108] V. F. Gantmakher, M. V. Golubkov, V. T. Dolgopolov, G. E. Tsydynzhapov, and A. A. Shashkin. Destruction of localized electron pairs above the magnetic-field-driven superconductor-insulator transition in amorphous In-O films. *Journal of Experimental and Theoretical Physics Letters*, 68(4):363–369, August 1998.

[109] Tatyana I. Baturina, C. Strunk, M. R. Baklanov, and A. Satta. Quantum metallicity on the high-field side of the superconductor-insulator transition. *Physical Review Letters*, 98(12):127003, March 2007.

[110] H. Q. Nguyen, S. M. Hollen, M. D. Stewart, J. Shainline, Aijun Yin, J. M. Xu, and J. M. Valles Jr. Observation of giant positive magnetoresistance in a Cooper pair insulator. *Physical Review Letters*, 103(15):157001, October 2009.

[111] Yen-Hsiang Lin, JJ Nelson, and Allen M. Goldman. The role of mesoscopic disorder in determining the character of the field-induced insulating regime of amorphous ultrathin films. *Physica C: Superconductivity and its Applications*, 497:102–109, February 2014.

[112] Amit Ghosal, Mohit Randeria, and Nandini Trivedi. Role of spatial amplitude fluctuations in highly disordered s-wave superconductors. *Physical Review Letters*, 81(18):3940–3943, November 1998.

[113] Amit Ghosal, Mohit Randeria, and Nandini Trivedi. Inhomogeneous pairing in highly disordered s-wave superconductors. *Physical Review B - Condensed Matter and Materials Physics*, 65(1):1–13, November 2002.

[114] Yonatan Dubi, Yigal Meir, and Yshai Avishai. Island formation in disordered superconducting thin films at finite magnetic fields. *Physical Review B - Condensed Matter and Materials Physics*, 78(2):024502, July 2008.

[115] Karim Bouadim, Yen Lee Loh, Mohit Randeria, and Nandini Trivedi. Single- and two-particle energy gaps across the disorder-driven superconductorinsulator transition. *Nature Physics*, 7(11):884–889, November 2011.

[116] Tianran Chen, Brian Skinner, and Boris I. Shklovskii. Coulomb gap triptychs, 2 effective charge, and hopping transport in periodic arrays of superconductor grains. *Physical Review B*, 86(4):045135, July 2012.

[117] D. Bruce Buchholz, Qing Ma, Diego Alducin, Arturo Ponce, Miguel Jose-Yacaman, Rabi Khanal, Julia E. Medvedeva, and Robert P. H. Chang. The structure and properties of amorphous indium oxide. *Chemistry of Materials*, 26(18):5401–5411, September 2014.

[118] Christopher Leighton. Private Communication, 2018.

[119] Petr Klapetek, David Nečas, and Christopher Anderson. Gwyddion user guide, 2016.

[120] Thomas Gredig, Evan A Silverstein, and Matthew P Byrne. Height-height correlation function to determine grain size in iron phthalocyanine thin films. *Journal of Physics: Conference Series*, 417:012069, March 2013.

[121] Victor M. Galitski and Anatoly I. Larkin. Disorder and quantum fluctuations in superconducting films in strong magnetic fields. *Physical Review Letters*, 87(8):087001, August 2001.

[122] Johanna Seidemann, Benjamin Sacépé, Maoz Ovadia, Dan Shahar, Karen Michaeli, and Mikhail V. Feigel'man. Quantum meets classical phase transition: Low-temperature anomaly in disordered superconductors near B_{c2}, September 2016.

[123] N. Giodano. Superconducting fluctuations in one dimension. *Physica B: Condensed Matter*, 203(3-4):460–466, December 1994.

[124] C. N. Lau, N. Marković, M. Bockrath, A. Bezryadin, and M. Tinkham. Quantum phase slips in superconducting nanowires. *Physical Review Letters*, 87(21):217003, November 2001.

[125] David R. Nelson and Valerii M. Vinokur. Boson localization and correlated pinning of superconducting vortex arrays. *Physical Review B*, 48(17):13060–13097, November 1993.

[126] P. J. M. Wöltgens, C. Dekker, R. H. Koch, B. W. Hussey, and A. Gupta. 2D-3D crossover effects on the vortex-glass phase transition in thin $YBa_2Cu_3O_{7-\delta}$ films. *Physica B: Physics of Condensed Matter*, 194-196:1911–1912, February 1994.

[127] Z. Sefrioui, D. Arias, M. Varela, M. A. López De La Torre, C. León, G. D. Loos, and J. Santamaría. Pure 2D vortex-glass phase transition with $T_g = 0$ K in deoxygenated $YBa_2Cu_3O_{6.4}$ thin films. *Europhysics Letters*, 48(6):679–685, December 1999.

[128] Ilana M. Percher, Irina Volotsenko, Aviad Frydman, Boris I. Shklovskii, and Allen M. Goldman. Vortex variable range hopping in a conventional superconducting film. *Physical Review B*, 96(22):224511, December 2017.

[129] Nicholas P. Breznay, Myles A. Steiner, Steven A. Kivelson, and Aharon Kapitulnik. Self-duality and a Hall-insulator phase near the superconductor-to-insulator transition in indium-oxide films. *Proceedings of the National Academy of Sciences*, 113(2):280–285, January 2016.

[130] Michael Mulligan. Particle-vortex symmetric liquid. *Physical Review B*, 95(4):045118, January 2017.

[131] Om Prakash, Anil Kumar, A Thamizhavel, and S Ramakrishnan. Evidence for bulk superconductivity in pure bismuth single crystals at ambient pressure. *Science*, 355(6320):52–55, January 2017.

[132] Werner Buckel. Hall-effekt von abschreckend kondensierten wismutschichten. *Zeitschrift für Physik*, 154(4):474–485, August 1959.

[133] K. Das Gupta, G. Sambandamurthy, Swati S. Soman, and N. Chandrasekhar. Possible robust insulator-superconductor transition on solid inert gas and other substrates. *Physical Review B - Condensed Matter and Materials Physics*, 63(10):5, February 2001.